

Investigation of Wireless Sensor Network for In-Situ Exploration of Water Ice on the Moon

**Submitted in partial fulfillment of the requirements
of the degree of**

Doctor of Philosophy

by

Jayesh P. Pabari



**Department of Electrical Engineering
INDIAN INSTITUTE OF TECHNOLOGY BOMBAY
2011**

Investigation of Wireless Sensor Network for In-Situ Exploration of Water Ice on the Moon

**Submitted in partial fulfillment of the requirements
of the degree of**

Doctor of Philosophy

by

**Jayesh P. Pabari
(Roll No. 05407702)**

Under the guidance of

**Prof. U. B. Desai (Guide)
and
Dr. Y. B. Acharya (Co-Guide)**



**Department of Electrical Engineering
INDIAN INSTITUTE OF TECHNOLOGY BOMBAY
2011**

Dedicated to
my wife
and
parents

Thesis Approval

This thesis entitled

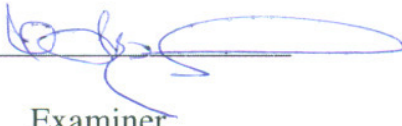
**Investigation of Wireless Sensor Network for
In-Situ Exploration of Water Ice
on the Moon**

by

Jayesh P. Pabari
(Roll No. 05407702)

is approved for the degree of

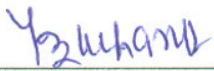
Doctor of Philosophy



Examiner



Examiner



Co-Guide



Guide



Chairman

Date: 3rd December 2011

Place: Mumbai

Declaration

I declare that this written submission represents my ideas in my own words and where others' ideas or words have been included, I have adequately cited and referenced the original sources. I also declare that I have adhered to all principles of academic honesty and integrity and have not misrepresented or fabricated or falsified any idea/data/fact/source in my submission. I understand that any violation of the above will be cause for disciplinary action by the Institute and can also evoke penal action from the sources which have thus not been properly cited or from whom proper permission has not been taken when needed.



(Signature)

Jayesh P. Pabari

(Roll No. 05407702)

Date: 3rd December 2011

Abstract

With the advancement in wireless technology, smart sensing devices and inquisitiveness; wireless sensors and their networks are sought for space sciences and technologies, either to explore beyond the awareness of human kind or to monitor performances of sophisticated systems. They have potentials for studying lunar and planetary surface sciences, by employing appropriate sensors. Detection of presence of water ice within the planetary regolith is crucial for future manned explorations as well as for understanding geological history of the surface. The search for the presence of lunar water has attracted considerable attention and motivated several recent lunar missions. Though, a few recent lunar missions have detected the water ice, all such results are based on remote observations from the orbiter. To detect the potential water bearing sites and to confirm the remote observations, in-situ measurements of water ice of different geographical locations are essential. The primary focus of the thesis is to address the research issues related to in-situ measurement of water ice on lunar surface using a wireless sensor network. Major challenges are the lack of knowledge of wireless communication on the moon, unavailability of compact water ice sensor, the sensor deployment issue and the operation of sensors in very harsh environment. Most of the challenges of lunar wireless sensor network are in physical layer of the open systems interconnection model.

In view of the fact that there is no atmosphere on the moon, communication scenario is expected to be different as compared to that on the earth. A lunar wireless model for finding

the path loss has been proposed, which is governed by various physical phenomena occurring during the wave propagation on the moon. The RF coverage predictions have been accomplished by the proposed lunar wireless model using the terrain data, measured by a terrain mapping camera on Chandrayaan-1. These form the first thesis contribution.

Wireless sensors are able to measure the required quantity and transmit the data to a rover, navigating the lunar surface. Such deployed sensors form a wireless point-to-point link between a sensor node and the rover. Due to irregular lunar surface terrain, there can be a large number of multipath components at the receiver in such a lunar multipath fading channel. A technique has been suggested for the prediction of power delay profile and the error rate analysis of lunar wireless link, based on the proposed lunar wireless model. Terrain based analysis of lunar multipath environment has been carried out and link performance parameters like the bit error rate, the packet error rate, the power delay profile and the maximum bit rate for data transmission have been predicted. These works form the second thesis contribution.

The presence of water ice mixed with the regolith can be inferred by measuring permittivity of the regolith. The data can be transmitted to a rover, navigating the lunar surface, and ultimately to the earth via an orbiter around the moon. Though, water detection or soil moisture sensors are available commercially, such soil moisture sensors are based on reflectometry and generally have a long probe, typically about 50 mm in length. Moreover, the probe needs to be inserted fully inside the soil surface for its efficient use. Such stringent requirements can pose limitation for the use in space applications, where payload size and mass are always critical issues. Also, the conventional sensors use operating frequency in MHz range, where there is an ambiguity in differentiating between dry regolith and ice; as permittivity of the regolith and the ice are almost comparable in this range. To address these issues; a distinct type of water ice sensor, called wireless impedance sensor node, has been proposed. It works on impedance measurement technique and the data communication is achieved at 2.4 GHz frequency in wireless mode. It has compact dimensions for the size critical space applications, without necessitating a long probe. The proposed sensor can be made to operate in transition region of the permittivity of ice, by feeding an appropriate master clock. This promises applicability of the proposed sensor for lunar and planetary surfaces, where water could be in the

ice form due to very low temperatures. The wireless impedance sensor node provides the permittivity at multiple frequencies in a given measurement range, in contrast to a single point measurement in case of a conventional sensor. This inherent property of the proposed sensor can be helpful in further characterizing the water ice. The lab model of the wireless impedance sensor node has been designed, evaluated and developed. To consider the lunar application, the water ice and the lunar soil simulant JSC-1A have been tested using the sensor and the performance of the sensor has been verified by testing the Milli-Q water, whose permittivity is known. These form the third thesis contribution.

Finally, even if appropriate types of sensors are available, the sensor deployment on the moon is also a very critical issue, due to the lack of enough control over it. Because of challenges involved in the deployment of sensors on a planet or outer body like the moon, there is a need of theoretical understanding before real implementation. A few techniques of sensor deployment on lunar surface have been suggested and compared. Minimum number of sensors needed to cover a given sensing region is derived, assuring wireless connectivity between the nodes. The condition on permissible tolerances in the desired dropping positions of the sensors is derived to address the practical difficulty in achieving exact locations. Moreover, the equations of sensor trajectory parameters have been derived for the moon, as gravity of the moon is different than that of the earth. These works form the final thesis contribution.

Contents

| | |
|---|----------|
| List of Tables | xv |
| List of Figures | xvii |
| 1 Introduction | 1 |
| 1.1 Exploration of Lunar Water..... | 2 |
| 1.2 Thesis Contributions..... | 3 |
| 1.3 Thesis Organization..... | 6 |
| 2 Overview: Bridging Wireless Technology and Space Science | 7 |
| 2.1 Present Wireless Scenario..... | 8 |
| 2.1.1 Existing Wireless Technology..... | 9 |
| 2.1.2 Wireless Sensor Network and Applications..... | 14 |
| 2.1.3 Existing Wireless Propagation Models..... | 16 |
| 2.2 Wireless Channel Fading..... | 18 |
| 2.2.1 Fading Parameters..... | 19 |
| 2.2.2 Multipath Fading..... | 22 |
| 2.2.3 Doppler Fading..... | 23 |
| 2.2.4 Rayleigh Fading Distribution..... | 25 |
| 2.2.5 Rician Fading Distribution..... | 25 |
| 2.3 Lunar Surface Science..... | 27 |

| | | |
|----------|--|-----------|
| 2.3.1 | Moon Environment..... | 27 |
| 2.3.2 | Lunar Surface Properties..... | 30 |
| 2.3.3 | Lunar Soil Simulant..... | 32 |
| 2.4 | Wireless Technology for Space Science and Applications..... | 33 |
| 2.5 | In-Situ Exploration of Water Ice..... | 35 |
| 2.5.1 | Existing Water Sensors..... | 37 |
| 2.5.2 | Additional Water Sensors..... | 40 |
| 2.6 | Sensor Deployment Scheme..... | 42 |
| 2.7 | Summary..... | 45 |
| 3 | Lunar Wireless Model and RF Coverage Prediction | 47 |
| 3.1 | Lunar Wireless Path Loss Model..... | 48 |
| 3.1.1 | Suitability of Existing Models..... | 49 |
| 3.1.2 | Physical Phenomena in Wave Propagation..... | 50 |
| 3.1.3 | Proposed Lunar Wireless Model..... | 54 |
| 3.2 | Modeling Parameters..... | 55 |
| 3.3 | Digital Elevation Model of Selected Lunar Site..... | 56 |
| 3.4 | Justification in Support of LWM..... | 59 |
| 3.5 | Results and Discussions..... | 60 |
| 3.6 | Conclusion..... | 64 |
| 4 | Lunar Multipath Environment and Wireless Link Analysis | 65 |
| 4.1 | Number of Multipath..... | 70 |
| 4.2 | Region under Consideration..... | 72 |
| 4.3 | Selection of Channel Object..... | 73 |
| 4.4 | Results and Discussions..... | 75 |
| 4.5 | Lunar Multipath Analysis Technique..... | 84 |
| 4.6 | Conclusion..... | 85 |
| 5 | Design, Development and Testing of Wireless Impedance Sensor Node | 87 |
| 5.1 | Need of Special Water Ice Sensor..... | 88 |

| | | |
|----------|--|------------|
| 5.2 | Algorithms..... | 89 |
| 5.2.1 | Impedance Algorithm..... | 90 |
| 5.2.2 | Parameter Extraction Algorithm..... | 92 |
| 5.3 | Principle of Operation..... | 93 |
| 5.4 | Design, Evaluation and Development of WISN..... | 95 |
| 5.4.1 | Merits of WISN over Existing Sensors..... | 100 |
| 5.5 | Experimental Set Up..... | 101 |
| 5.5.1 | WISN Calibration..... | 102 |
| 5.6 | Results and Discussions..... | 102 |
| 5.6.1 | Terrestrial Soil Testing (Phase I)..... | 104 |
| 5.6.2 | Milli-Q Water Testing (Phase II)..... | 105 |
| 5.6.3 | Ice Testing (Phase III)..... | 106 |
| 5.6.4 | Lunar Soil Simulant Testing (Phase IV)..... | 107 |
| 5.7 | Thermal and Space Qualification Consideration..... | 111 |
| 5.8 | Conclusion..... | 112 |
| 6 | Investigation of Sensor Deployment Schemes | 113 |
| 6.1 | Circular Deployment..... | 114 |
| 6.2 | Spherical Segment Deployment..... | 123 |
| 6.3 | Parabolic Launching..... | 127 |
| 6.4 | Deployment Simulation Consideration..... | 138 |
| 6.5 | Discussions..... | 138 |
| 6.6 | Summary and Conclusion..... | 141 |
| 7 | Conclusion and Future Work | 143 |
| | References..... | 147 |
| | Publications..... | 163 |
| | Acknowledgements..... | 165 |

List of Tables

| | | |
|-----|---|-----|
| 3.1 | Modeling parameters for RF coverage prediction..... | 55 |
| 3.2 | Selected lunar sites for RF coverage prediction..... | 56 |
| 3.3 | Lunar site coverage..... | 63 |
| 4.1 | Multipath number calculation..... | 77 |
| 4.2 | Multipath parameters, bit rates and packet loss..... | 83 |
| 5.1 | Comparison of permittivity measured by WISN with the reported values.... | 107 |
| 5.2 | Volumetric water contents, measured porosities and estimated upper limits of permittivity of mixtures..... | 110 |
| 6.1 | Deployment parameters of typical circular schemes..... | 123 |
| 6.2 | Comparison of deployment costs of three schemes..... | 141 |

List of Figures

| | | |
|---------|--|----|
| 2.1 | Typical multi-hop wireless sensor network..... | 14 |
| 2.2 | General structure of a wireless sensor node..... | 15 |
| 2.3 | Small scale fading due to multipath delay spread..... | 23 |
| 2.4 | Small scale fading due to Doppler spread..... | 24 |
| 2.5 | Various fadings as a function of symbol period..... | 24 |
| 2.6 | Probability density function of Rician distribution..... | 26 |
| 2.7 | Reflectometry based soil moisture sensor..... | 38 |
| 2.8 (a) | Phase diagram of water..... | 40 |
| 2.8 (b) | Conceptual design of IR sensor..... | 40 |
| 2.9 | Conceptual design of optical water ice sensor..... | 41 |
| 2.10 | Block diagram of microwave water sensor..... | 42 |
| 2.11 | Grid deployment with square cells having dropping points at the centre.. | 43 |
| 2.12 | Sensors dropped from an aircraft in a typical system..... | 44 |
| 2.13 | Concept of sensor deployment on lunar surface from satellite..... | 45 |
| 3.1 (a) | DEM of lunar site 1..... | 57 |
| 3.1 (b) | DEM of lunar site 2..... | 57 |
| 3.1 (c) | DEM of lunar site 3..... | 57 |
| 3.1 (d) | DEM of lunar site 4..... | 58 |

| | | |
|---------|--|----|
| 3.2 (a) | 3-D DEM of lunar site 1..... | 58 |
| 3.2 (b) | 3-D DEM of lunar site 2..... | 58 |
| 3.2 (c) | 3-D DEM of lunar site 3..... | 59 |
| 3.2 (d) | 3-D DEM of lunar site 4..... | 59 |
| 3.3 | Area coverage pattern of lunar site 1..... | 61 |
| 3.4 | Area coverage pattern of lunar site 2..... | 61 |
| 3.5 | Area coverage pattern of lunar site 3..... | 62 |
| 3.6 | Area coverage pattern of lunar site 4..... | 62 |
| 4.1 | Pictorial view of wireless sensors on lunar surface..... | 67 |
| 4.2 (a) | Exponentially decaying nature of lunar PDP..... | 71 |
| 4.2 (b) | Fourier transform of PDP..... | 71 |
| 4.3 | 3-D DEM of lunar site 3..... | 72 |
| 4.4 | Block diagram of lunar multipath channel..... | 73 |
| 4.5 (a) | PDP of a typical link in region 1 (crater) of site 3..... | 78 |
| 4.5 (b) | BER of a typical link in region 1 (crater) of site 3..... | 78 |
| 4.5 (c) | Rician k factors of all links in region 1 (crater) of site 3..... | 78 |
| 4.5 (d) | BER of all possible links in region 1 (crater) of site 3, over Rician channel..... | 79 |
| 4.5 (e) | BER of all possible links in region 1 (crater) of site 3, over Rayleigh channel..... | 79 |
| 4.5 (f) | PER of a typical link in region 1 (crater) of site 3..... | 79 |
| 4.6 (a) | PDP of a typical link in region 2 of site 3..... | 80 |
| 4.6 (b) | BER of a typical link in region 2 of site 3..... | 80 |
| 4.6 (c) | Rician k factors of all links in region 2 of site 3..... | 80 |
| 4.6 (d) | BER of all possible links in region 2 of site 3, over Rician channel..... | 81 |
| 4.6 (e) | BER of all possible links in region 2 of site 3, over Rayleigh channel..... | 81 |
| 4.6 (f) | PER of a typical link in region 2 of site 3..... | 81 |
| 4.7 (a) | DEM of 168 th latitude position, showing transmitter location at 300 th longitude position, in region $R1$ inside the crater..... | 84 |
| 4.7 (b) | Close up view of the region $R1$ as 3-D DEM..... | 84 |
| 4.8 (a) | DEM of 80 th latitude position, showing transmitter location at 168 th | |

| | | |
|----------|---|-----|
| | longitude position, in region <i>R2</i> outside the crater..... | 84 |
| 4.8 (b) | Close up view of the region <i>R2</i> as 3-D DEM..... | 84 |
| 5.1 (a) | Principle of impedance measurement..... | 89 |
| 5.1 (b) | Soil equivalent circuit..... | 89 |
| 5.2 (a) | Impedance sensor blocks..... | 94 |
| 5.2 (b) | A typical up chirp signal..... | 94 |
| 5.3 | Principle of operation of impedance sensor..... | 95 |
| 5.4 (a) | Developmental blocks of WISN..... | 97 |
| 5.4 (b) | PCB details..... | 97 |
| 5.4 (c) | Top snapshot of WISN..... | 97 |
| 5.4 (d) | Side snapshot of WISN..... | 97 |
| 5.4 (e) | Snapshot of measuring WISN and data aggregator WISN..... | 97 |
| 5.5 | Experimental Set Up for Testing..... | 101 |
| 5.6 | Plot of Z_R (measured, blue), Z_I (measured, magenta), Z_{Real} Theory (theoretical, red) and Z_{Imag} Theory (theoretical, cyan) versus frequency | 103 |
| 5.7 (a) | Response of resistors..... | 103 |
| 5.7 (b) | Capacitance associated with resistance..... | 103 |
| 5.8 (a) | Snapshot of sand type soil..... | 104 |
| 5.8 (b) | Capacitance versus frequency results of sand for various water contents... | 104 |
| 5.9 | Real (ϵ') and imaginary (ϵ'') parts of dielectric constant of Milli-Q water.. | 105 |
| 5.10 | Real (blue) and imaginary (red) relative permittivity of Milli-Q water..... | 106 |
| 5.11 | Real (blue) and imaginary (red) relative permittivity of ice at 273 K..... | 107 |
| 5.12 (a) | Snapshot of JSC-1A..... | 108 |
| 5.12 (b) | Capacitance versus frequency results of JSC-1A for various water contents..... | 108 |
| 5.13 | Real relative permittivity of JSC-1A, for various water contents..... | 109 |
| 5.14 | Real conductivity of JSC-1A, for various water contents..... | 110 |
| 6.1 | Circular ring package for sensor deployment..... | 115 |
| 6.2 | Sensor fall time vs. altitude..... | 118 |
| 6.3 | Initial velocity vs. altitude & distance to be covered..... | 118 |
| 6.4 | Impact velocity vs. altitude & initial thrust velocity..... | 119 |

| | | |
|---------|--|-----|
| 6.5 | Deployment pressure vs. altitude & distance to be covered..... | 119 |
| 6.6 | Deployment energy vs. altitude & distance to be covered..... | 120 |
| 6.7 (a) | Geometry for minimum number of sensors in circular topology..... | 121 |
| 6.7 (b) | Geometry for practical sensor positions..... | 121 |
| 6.8 | Minimum number of sensors in circular topology vs. radius of sensing zone (R) & line-of-sight communication range (d_s)..... | 121 |
| 6.9 (a) | Position of sensors in spherical deployment package..... | 124 |
| 6.9 (b) | Position of sensors in sensing region..... | 124 |
| 6.10 | Minimum number of sensors in spherical scheme vs. radius of sensing zone (R) & line-of-sight communication range (d_s)..... | 127 |
| 6.11 | Geometry of sensor launching scheme..... | 129 |
| 6.12 | Topology showing number and positions of sensors in a typical circular sensing zone of 1 km diameter..... | 129 |
| 6.13 | Pictorial view of scheme at crater..... | 130 |
| 6.14 | Depth of crater from the edge vs. impact velocity of sensor ($v_i = 10 \text{ m/s}$)..... | 132 |
| 6.15 | Impact angle of sensor vs. launching angle ($v_i = 10 \text{ m/s}$)..... | 132 |
| 6.16 | Time of flight of sensor vs. launching angle & impact velocity ($h = -1 \text{ km}, v_i = 10 \text{ m/s}$)..... | 132 |
| 6.17 | Distance of sensor vs. launching angle & impact velocity ($h = -1 \text{ km}, v_i = 10 \text{ m/s}$)..... | 133 |
| 6.18 | Depth of crater achieved by a sensor vs. launching & impact velocities..... | 133 |
| 6.19 | Impact angle of sensor vs. launching velocity..... | 134 |
| 6.20 | Time of flight of sensor vs. launching & impact velocities ($h = -1 \text{ km}, \theta = 30^\circ$)..... | 134 |
| 6.21 | Distance covered by a sensor vs. launching & impact velocities ($h = -1 \text{ km}, \theta = 30^\circ$)..... | 135 |
| 6.22 | Minimum number of sensors in parabolic type scheme vs. radius of sensing zone (R) & wireless connectivity range (d_s)..... | 137 |

Chapter 1

Introduction

Wireless Sensor Network (WSN) has the potential to be used for environmental monitoring, habitat study, military surveillance and reconnaissance, building safety and earthquake monitoring, medical field, machinery, ocean and wildlife monitoring, shipboard, transportation systems automation as well as space and planetary sciences. The WSNs are usually employed to monitor physical quantities such as temperature, pressure, light, vibrations, gas etc for controlling the environment in a spatially distributed manner. The sensors integrated into structures, machinery and the environment; coupled with the efficient delivery of sensed information; could provide tremendous benefits to society. A major benefit of these systems is that they perform in-network processing to reduce the large streams of raw data into useful aggregated information.

The search for the presence of lunar water has attracted considerable attention and motivated several recent lunar missions, largely because of water being useful in rendering long-term lunar habitation feasible. The detection of presence of water ice within the planetary regolith is crucial for the future manned exploration as well as for understanding geological history of the surface. With the advancement in wireless technology, smart sensing devices and inquisitiveness; wireless sensors and their networks are sought for space sciences

and technologies, either to explore beyond awareness of human kind or to monitor performances of sophisticated systems. The wireless technology promises its use for planetary exploration, spacecraft health, astronaut health monitoring and so forth. Thus, the scope of WSNs as well as wireless devices may extend beyond the earth to many space applications and motivated researches are needed to overcome the challenges involved in space.

Planetary surface science is the study of physical, chemical and thermal properties of the surface as well as subsurface materials of a planet. Though, the moon is not a planet of the solar system, it is of great interest to the space researchers; since it is the nearest to the earth.

1.1 Exploration of Lunar Water

It is known that the moon has very thin atmosphere with vacuum of the order of 10^{-12} Torr [1, 2] and lunar temperature varies approximately from -200 to +125 degree Celsius depending upon day and night conditions and locations [3]. It is extremely difficult for water to remain in stable form under such environment. However, few molecules of water might have been present on the moon, due to striking of water bearing comets and meteorites on its surface. Over thousands of years, these molecules might have been transferred to the polar regions, where they could be trapped inside cold traps or permanently shadowed regions due to very low temperatures. It is understood that water ice may be present in the permanently dark regions, inside craters, near the lunar south pole. Volatiles like water and CO_2 can provide information about history of the moon and cometary impacts. Water and CO_2 form essential elements for life. Also, the presence of volatiles provide source of rocket fuel.

There had been contradiction between the Clementine orbiter data and the earth based Arecibo Radar Observatory data, regarding the presence of water ice at lunar south pole [4]. Observations from very recent lunar mission [5] indicate the presence of water on the moon. Remote techniques are based on a signature of water molecule in the absorption spectra, obtained in infrared range [6] of ElectroMagnetic (EM) spectrum. When sunlight gets reflected from the lunar surface, a reflectance spectrum is obtained and a dip in the spectrum

indicates the presence of water ice. Water absorption may also be found in ultraviolet and microwave ranges of electromagnetic spectrum. It is also possible to know the presence of water using a RADAR [7] by studying the polarization ratio. However, all such results are based on remote observations from the orbiter. Apollo missions, which were ended in 1972, had carried out in-situ measurements in equatorial regions of the moon. There has not been in-situ measurement near the lunar south pole, and the mystery of potential areas containing water ice on the moon remains unsolved to the space science community. To detect the potential water bearing sites and to confirm the remote observations, in-situ measurements of water ice of different geographical locations are essential. For in-situ measurement, it is necessary to deploy a Wireless Sensor Network (WSN) consisting of water ice sensors operating in wireless mode. To study lunar regolith (soil) properties like the ambient light, surface temperature, electrical conductivity as well as permittivity and to infer the presence of water ice by in-situ measurement; a WSN is proposed to be deployed near the lunar south pole, by a future lunar mission. There can be many challenges involved in deploying the WSN on an outer body like the moon. Major challenges are the lack of knowledge of wireless communication on the moon, unavailability of compact water ice sensor, the sensor deployment issue and the operation of sensors in very harsh environment. Most of the challenges of lunar WSN are in physical layer of the Open Systems Interconnection (OSI) model [8]. Thesis contributions are targeted in solving such research issues, in a new application of WSN on the lunar surface. The contributions may also be useful for other planetary missions or similar applications.

1.2 Thesis Contributions

In view of the fact that there is no atmosphere on the moon, communication scenario on the moon is expected to be quite different as compared to that on the earth. Hence, the present wireless propagation models for terrestrial networks on the earth cannot be applied for the moon. This necessitates originating a lunar wireless model and needs information about the terrain of a landing site. A Lunar Wireless Model (LWM) for finding path loss has been proposed, which is governed by various physical phenomena occurring during the wave

propagation on the moon. Terrain Mapping Camera (TMC) on Chandrayaan-1, a recent Indian mission to the moon, has provided high-quality Digital Elevation Model (DEM) data and such terrain data are required in the LWM. A few lunar sites have been selected and the terrain based predictions of RF coverage have been accomplished, based on the proposed LWM. The RF coverage predictions use actual DEM data of the selected lunar sites. These form the first contribution of thesis.

Once the wireless sensors are deployed on the lunar surface at a selected landing site, they can measure the permittivity of regolith and transmit the data in wireless mode. The permittivity of regolith increases when water is added to it. The value of the permittivity is measured by a sensor and one can infer the presence of water, mixed with the regolith. The data can be transmitted to a rover, navigating the lunar surface, and ultimately to the earth via an orbiter around the moon. Such deployed sensors form a wireless point-to-point link between a sensor node and the rover. Due to irregular lunar surface terrain, there can be a large number of multipath components at the receiver. It is suggestive to predict the wireless link performance beforehand, in lunar multipath fading channel, by analyzing performance parameters like the Bit Error Rate (BER), Packet Error Rate (PER), Power Delay Profile (PDP) and maximum bit rate for data transmission. Measurement of the PDP of a lunar wireless link is not feasible. A technique has been suggested for the prediction of lunar PDP and the error rate analysis of the lunar wireless link, based on the proposed LWM. Typical wireless links on the selected lunar regions have been analyzed using the actual DEM to predict the link performances and the results have been compared. These works form the second thesis contribution.

Though, water detection or soil moisture sensors are available commercially [9], such soil moisture sensors are based on reflectometry principle. Such sensors generally have a long probe, typically about 50 mm in length, to propagate either a pulse or a sinusoidal signal of fixed frequency. Moreover, the probe needs to be inserted fully inside the soil surface for its efficient use. Such stringent requirements can pose limitation for the use in space applications, where payload size and mass are always critical issues. The third contribution of thesis is in the design, evaluation, development and testing of a distinct type of water ice sensor, called Wireless Impedance Sensor Node (WISN), based on impedance spectroscopy. The developed

lab model operates at 2.4 GHz in wireless mode. The WISN does not have necessarily long probe. It needs only an electrical contact with the soil sample under measurement, providing excellent flexibility in terms of electrode design. The WISN promises compact dimensions for the size critical applications. In addition, the WISN can provide the permittivity at multiple frequencies in a given measurement range, in contrast to a single point measurement in case of reflectometry based sensor. This inherent property of the WISN can be helpful in further characterizing the water ice. Thus, the WISN offers several precious rewards for future space and planetary applications. It can also be exploited for soil moisture measurement in terrestrial applications on the earth and other impedance based applications.

Finally, if appropriate types of sensors are available, the sensor deployment on the moon is also a very critical issue. This is because, there is no enough control over it and huge amount of funds are invested in a space mission. The deployment of sensors on a planet or outer body like the moon is really a challenging task and needs theoretical understanding before implementing through any space mission. A few techniques of sensor deployment on lunar surface have been suggested, and the minimum number of sensors needed to cover a given sensing region is derived in each case, assuring wireless connectivity between the nodes. Also, the condition on permissible tolerances in the desired dropping positions of the sensors is derived to address the practical difficulty in achieving exact locations. Moreover, the equations of sensor trajectory parameters have been derived for the moon, as gravity of the moon is different than that of the earth. These works form the final thesis contribution.

To summarize, the key contributions of the thesis are:

- The proposal of a lunar wireless model and the RF coverage predictions using the actual terrain data of the moon.
- The suggestion of a technique for the prediction of lunar PDP, lunar multipath analysis and error rate analysis of the lunar wireless link.
- The proposal of a wireless impedance sensor node for water ice detection on the lunar surface; design, evaluation, development and testing of the lab model of the WISN.

- The suggestion of a few sensor deployment schemes for lunar surface, the derivation of the tolerance condition for the sensor positions, various trajectory parameters and the minimum number of sensors.

In order to carry out in-situ exploration of water ice on the moon, a wireless sensor network is promising technology and contributions given in this thesis could be useful to mission planners.

1.3 Thesis Organization

The thesis is organized as follows. Chapter 2 describes review on the present wireless scenario, channel fadings, lunar surface science, wireless technology for space science, existing water sensors and sensor deployment schemes. It outlines the literature survey and bridges the two different areas, i.e., the wireless technology and the space science. Chapter 3 is on lunar wireless model and RF coverage prediction. It provides results of RF area coverage patterns, based on actual DEM. Chapter 4 presents the lunar multipath environment and wireless link analysis. The comparative results in Chapter 4 provide good insight into the selection of a link on the moon and furnish performance parameters of a given link on the moon. Chapter 5 gives the design and developmental details of a Wireless Impedance Sensor Node (WISN), along with water, ice and soil testing results. Chapter 6 suggests a few sensor deployment schemes for the lunar application, with results of sensor trajectory parameters and minimum number of sensors in each case. The thesis ends with Chapter 7, giving conclusion and direction for future work.

Chapter 2

Overview: Bridging Wireless Technology and Space Science

Radio wave transmission in wireless mode through a communication channel is very old and mature technology. Due to advancement in semiconductor and microelectronics technologies and also due to ever hungry user demand, the wireless world has travelled through various stages of development. Along with vertical growth of wireless technology, their applications are also increasing in diversified fields including military, space, precision agriculture, office automations, security and so forth. Research has also become essential in applied fields of wireless technology to meet the challenging requirements of various applications. The problems addressed in this thesis include interdisciplinary areas and it is necessary to review existing scenario of various fields to couple them together to arrive at possible solutions.

This chapter is organized as follows. Section 2.1 presents gradual progress in wireless technology and Section 2.2 describes various types of channel fading phenomena occurring during wireless communication. The problems addressed in the thesis focus on WSN on the moon to study the lunar surface science and so, it is essential to know the environment of the

moon. Section 2.3 gives details of the moon and related information. Section 2.4 connects the wireless technology to the space and planetary sciences, and also presents the associated constraints encountered in the implementation of the WSN for such applications. A key property of interest in lunar surface science is the permittivity of lunar soil (also referred to as regolith). The permittivity of regolith may be derived using a soil sensor or an electrical property sensor. Section 2.5 reviews existing water sensors and the conceptual designs of a few other potential sensors. The WSN is useful to study the physical property of interest and the sensors involved in the application need to be deployed in a geographical region. Section 2.6 reviews the deployment schemes for such sensors on the earth. The chapter ends with Section 2.7, which presents summary.

2.1 Present Wireless Scenario

There have been many wireless systems, which have come up in the past half century. Most of them target towards wireless communications of voice, data or multimedia; either for outdoor terrestrial networks or for indoor personal area networks and local area networks, inside a campus. Such technologies have been intended worldwide due to starving expansion of human activities around the globe. Some of the wireless technologies have been in use for deep space or satellite communications and also for remote sensing applications, going beyond the earth. With the advancement in wireless technology, smart sensing devices and inquisitiveness; wireless sensors and their networks are sought for space sciences and technologies; either to explore beyond the awareness of human kind or to monitor performances of sophisticated systems. Scope of WSN and wireless devices may extend beyond the earth to many space and planetary applications. Review of existing wireless technologies and models is, therefore, necessary to examine the applicability of WSN, to study lunar surface science. Since, the WSN broadly comes under the networking technology, it is imperative to refer the Open Systems Interconnection (OSI) model [8]. It is a way of subdividing a communication system into smaller parts, called layers. A layer provides services to its upper layer, while receiving services from the layer below. The OSI model actually

defines the operation of network devices by a network stack and there are seven layers suggested in the model. These are:

- Physical Layer: It handles a bit level signal and transmits as well as receives the data over a communication channel.
- Data Link Layer: It handles a frame level signal providing procedural means to transfer the data between network entities and to detect and possibly correct the errors. It defines physical address, controls shared access to channel and minimizes collisions.
- Network Layer: It handles packets of signal, performs network routing functions for path determination and does logical addressing.
- Transport Layer: It controls the reliability of a given link through flow control, segmentation/desegmentation and error control for end to end connection.
- Session Layer: It establishes, manages and terminates the connections between the local and remote applications.
- Presentation Layer: It converts machine dependent data to machine independent data performing data representation, encryption and decryption.
- Application Layer: It interacts with software applications that implement a communicating component. Its functions include identifying communication partners, determining resource availability and synchronizing communication.

2.1.1 Existing Wireless Technology

There have been many wireless technologies worldwide for various applications and include IEEE 802.11 up to 4G wireless technology.

A. IEEE 802.11

IEEE 802.11 standard [10-12] defines protocols for Wireless Local Area Network (WLAN) or Wi-Fi and these protocols are commonly used in wireless networking of

computers. Original standard was published in 1999 and there have been many amendments after that like IEEE 802.11a, b, d, e, g, h, i, j, k, n, r, w and y. IEEE 802.11 family suggests PHY (PHYSical) and MAC (Medium Access Control) layer protocols and includes over-the-air modulation techniques that use the same basic protocol. More popular are 802.11b, 802.11g and 802.11n protocols. Both, 802.11b and 802.11g use 2.4 GHz ISM band and may occasionally suffer interference from microwave ovens, cordless phones and Bluetooth devices. 802.11b uses Direct Sequence Spread Spectrum (DSSS) or Complementary Code Keying (CCK) and 802.11g uses Orthogonal Frequency Division Multiplexing (OFDM) or CCK or DSSS as signaling methods to control susceptibility to interference. 802.11b supports 20 MHz bandwidth with data rate of 11 Mbps and 802.11g supports 20 MHz bandwidth with 54 Mbps data rate. 802.11n is a new version of 802.11 and it uses Multiple Input Multiple Output (MIMO) with OFDM or CCK or DSSS in 2.4 GHz or 5 GHz band, having capability of 600 Mbps data rate and supporting 40 MHz bandwidth. IEEE 802.11 devices operate in Industrial, Scientific and Medical (ISM) bands and are limited to a range of several hundred metres. The 802.11 implements two MAC protocols as Point Coordination Function (PCF) and Distributed Coordination Function (DCF). In PCF, network operation is controlled by a central node and requires all devices to be in direct range; while DCF allows devices to form an ad-hoc network after implementation of suitable protocol at higher level. Such protocols may be implemented in WSN for the moon, as devices are expected to be in communication range with the rover. DCF implements Carrier Sense Multiple Access with Collision Avoidance (CSMA/CA), which is frequently exercised in wireless sensor networks. To avoid hidden node problem in wireless communication, 802.11 employs an RTS/CTS (Request to Send/Clear to Send) scheme. However, it has been shown by Xu and Saadawi [13] and Hsieh and Sivakumar [14] that CSMA/CA and RTS/CTS schemes significantly degrade the system performance when it is in 'ad-hoc mode' and internet data are transmitted across the network.

B. Bluetooth

Bluetooth [12, 15] is an open wireless technology standard for exchanging data over short distances of 10 m and 100 m from fixed and mobile devices like faxes, mobile phones, telephones, laptops, personal computers, printers, Global Positioning System (GPS) receivers,

digital cameras and video game consoles; creating Personal Area Network (PAN) with high levels of security. Bluetooth devices operate in various modes like Basic Rate (BR), Extended Data Rate (EDR) and High Speed (HS) rate in ISM band of 2.4 GHz. They use Frequency Hopping Code Division Multiple Access (FH-CDMA) and can achieve data rate of 1 Mbps to 24 Mbps using various modulation schemes like Gaussian Frequency Shift Keying (GFSK), $\pi/4$ -Differential Quadrature Phase Shift Keying (DQPSK) and 8 Differential Phase Shift Keying (DPSK).

Bluetooth is a connection oriented technology requiring devices to establish a communication channel before they converse. Bluetooth is a packet based protocol with a master-slave structure. One master may communicate with up to 7 slaves in a Piconet; all devices share the master's clock, master transmission begins in even slots and the slave transmits in odd slots. Bluetooth can form extended network by linking Piconets together but it takes substantial amount of time and demands links to remain continuously active. Forming links on demand may be possible but it is shown that additional overhead occurs in initializing the network [16, 17]. Such protocols are more suited for earth based systems.

C. IEEE 802.15.4 and Zigbee

IEEE 802.15.4-2006 [18] is a standard, which specifies the physical layer and medium access control for Low Rate Wireless Personal Area Network (LR-WPAN). It is the basis for the ZigBee, WirelessHART and MiWi specification; each of which further attempts to offer a complete networking solution by developing the upper layers, which are not covered by the standard. Alternatively, it can be used with 6LoWPAN and standard Internet protocols to build a Wireless Embedded Internet. The standard is designed for low power, low data rate devices; operating in 430 MHz or 868 MHz or 902 MHz or 2.4 GHz unlicensed frequency bands; with data rates up to 250 kbps. The standard specifies CSMA/CA medium access protocol with DSSS technique. Generally, orthogonal Quadrature Phase Shift Keying (QPSK) is used, having transmitter output power of 0 dBm (1 mW). The IEEE 802.15.4 transceiver ICs are simple and inexpensive, involving minimum peripheral components, e.g. CC2420 [19].

Zigbee is a specification for a suite of high level communication protocols using small, low-power digital radios based on the IEEE 802.15.4-2003 standard for Wireless Home Area Network (WHAN) such as wireless light switches with lamps, electrical meters with in-home displays and consumer electronics equipments via short-range radio. Zigbee protocols defined by Zigbee alliance [20] are intended to be simpler and less expensive than other WPAN such as Bluetooth. ZigBee [21] is targeted at Radio Frequency (RF) applications that require a low data rate and long battery life. Zigbee may be employed with simple mesh networking protocol for industrial control, embedded sensing, building automation etc. Zigbee devices are designed so that battery lasts for few years.

Zigbee standard defines three types of nodes, viz., Zigbee Coordinator (ZC), Zigbee Router (ZR) and Zigbee End Device (ZED). The ZED is a basic device for communication with higher level nodes, the ZR forwards packets from other nodes and the ZC is the most capable and the root of the network, many a times bridging two networks. Zigbee devices are battery powered and are normally used in short range, high density applications. Devices employing IEEE 802.15.4 protocols and possibly Zigbee protocols are quite promising for small range wireless sensor network on the moon, after space qualification.

D. WiMAX

WiMAX (Worldwide Interoperability for Microwave Access) [22-26] is a Broadband Wireless Access (BWA) technology based on the IEEE 802.16 standard that enables the delivery of high-speed personal broadband services to subscribers. WiMAX refers to interoperable implementations of the IEEE 802.16 wireless networks standard, ratified by the WiMAX Forum; in similarity with Wi-Fi, which refers to interoperable implementations of the IEEE 802.11 Wireless LAN standard, ratified by the Wi-Fi Alliance. It may use frequency in the range from a few hundred MHz to 66 GHz and it provides up to 40 Mbit/s with the IEEE 802.16m update expected to offer up to 1 Gbit/s fixed speeds.

WiMAX uses advanced radio technology with OFDM Scalable Orthogonal Frequency Division Multiple Access (SOFDMA) and smart antennas to deliver multi-play services, i.e.

voice, video and data over wireless and mobile networks. Operational in both licensed and license-exempt frequencies, the technology offers flexible and economically viable solutions for different deployment scenarios in urban, suburban and rural environments.

E. LTE

Long Term Evolution (LTE) [27-29] represents 4G wireless broadband technology developed by the Third Generation Partnership Project (3GPP), an industry trade group. The 3GPP is a standard body that works within the scope of the ITU to develop third (and future) generation wireless technologies that build upon the base provided by GSM. LTE represents next step (4G) in a progression from Global System for Mobile Communications (GSM) 2G standard to Universal Mobile Telecommunications System (UMTS) 3G technology. LTE is not a replacement for UMTS in the way that UMTS was a replacement for GSM, but rather an update to the UMTS technology that will enable it to provide significantly faster data rates for both uploading and downloading.

LTE will provide significantly increased peak data rates, with the potential for 100 Mbps downstream and 30 Mbps upstream, reduced latency, scalable bandwidth capacity and backwards compatibility with the existing GSM and UMTS technologies. The upper layers of LTE are based upon TCP/IP and will support mixed data, voice, video and messaging applications. Like WiMAX, LTE uses radio antenna technologies such as OFDM and MIMO, resulting in a higher Signal-to-Noise Ratio (SNR) to provide improved coverage and throughput, especially in dense urban areas.

F. 4G

4G [30-33] is the term for the fourth generation of wireless communications, defined by the ITU-T (International Telecommunication Union-Telecommunication Standardization Sector) as the IMT Advanced (International Mobile Telecommunications Advanced) standard. It is a successor to 3G and 2G families of standards. Future-proof fourth generation networks that comply with most or all of standard requirements are implemented using

emerging WiMAX technologies (IEEE 802.16e and IEEE 802.16m) and first release 3G Long Term Evolution. 4G refers to all-IP packet-switched networks, mobile ultra-broadband (gigabit speed) access and multi-carrier transmission.

2.1.2 Wireless Sensor Network and Applications

Wireless Sensor Network (WSN) in general, consists of a number of wireless sensors, networked together to sense a given region of interest for some physical quantity under consideration. A typical WSN is shown in Figure 2.1.

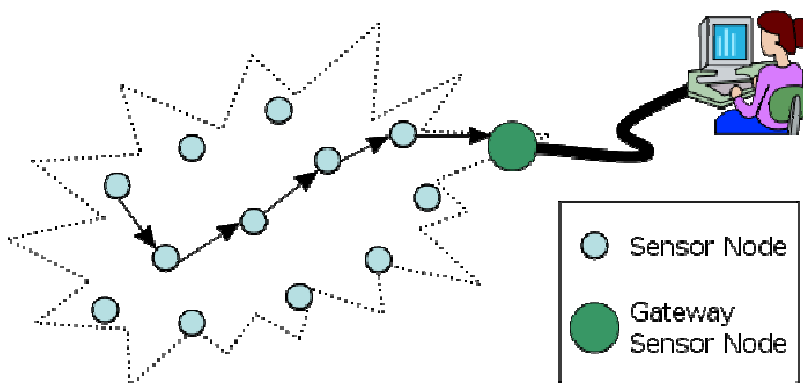


Figure 2.1: Typical multi-hop wireless sensor network.

The WSN may be ad hoc in nature, in which case, it consists of a large number of tiny self powered sensors capable of sensing physical phenomena and transmitting the information thus collected, to nearby nodes and subsequently routing towards the cluster head. The cluster head or the aggregator passes such information to outside world through internet. The sensor nodes are autonomous in nature and possess low level microcontroller, Analog-to-Digital Converter (ADC) and so forth as signal processing elements. Due to limited battery life time, the sensors can lose power over a period of time and thus network has a dynamic topology. The weight, size and power of sensor nodes have remained critical issues for long time depending on nature of an application. A typical sensor node described by Akyildiz et al. [34] has blocks as shown in Figure 2.2.

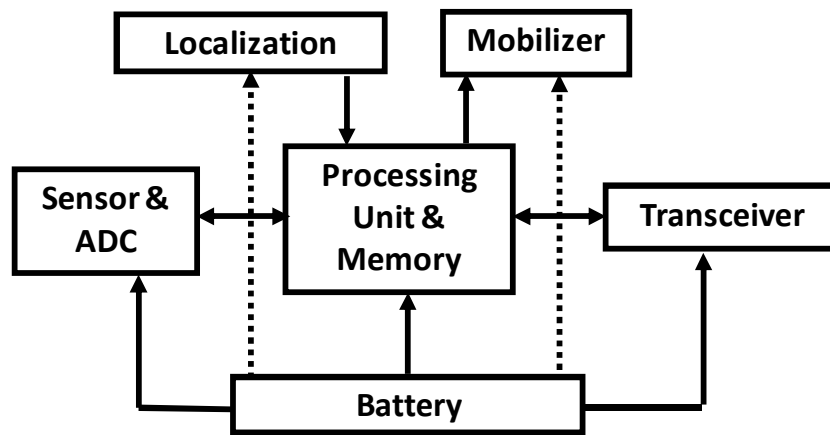


Figure 2.2: General structure of a wireless sensor node.

A set of sensors senses the physical properties of interest and provides the voltage signal, which is digitized by the ADC. Such digital signal is passed to a microcontroller for low level signal processing and the data are stored in the memory. A battery provides power to the sensor electronics. Generally, the WSN is deployed in remote and difficult to access area like a forest, and therefore, the nodes are left unattended. Hence, the sensor node normally remains in sleep mode to conserve the power and it wakes up for a very small duration to transmit the data to neighbors. Such transmission is accomplished by a transceiver on board and an antenna, which may be outside or PCB mounted. In some of the applications like tracking of a physical entity [35], location information is needed and a localizer unit is added to the node; while mobilizer is necessary in applications where sensor nodes need to move small distances after deployment. However, localizer and mobilizer are optional and may be omitted, if not required for a specific application.

Many applications of WSN have been reported in the literature like environmental data collection, security monitoring and sensor node tracking as given by Hill [36]. The environmental data collection applications [36] typically use tree-based routing topologies, where each routing tree is rooted at high-capability nodes that sink the data. The nodes with a large number of descendants transmit significantly more data than leaf nodes. These nodes can quickly become energy bottlenecks [37, 38]. In security monitoring applications [36], each node has to frequently check the status of its sensors but it only has to transmit a data report, when there is a security violation. In a security monitoring network, optimal configuration would be to have a linear topology. In node tracking scenario [36], a tagged

object is tracked by simply tagging it with a small sensor node, through a region of space, monitored by a sensor network. The node tracking applications will continually have topology changes as the nodes move through the network. It is essential that the network be able to efficiently detect the presence of new nodes that enter the network. In general, complete application scenarios contain aspects of all three categories and the network may be a hybrid one [36]. Applications of WSN in structural health monitoring and industrial automation have been given in [39]. Tavares et al. [40] describe application of WSN to automobiles. Thus, applications of WSN are in many diversified fields like commercial, military, health, environment etc on the earth. Applications of wireless technology for space and planetary sciences have been shown in Section 2.4 in this chapter.

2.1.3 Existing Wireless Propagation Models

It is expected that communication would be better on the moon as compared to that on the earth, due to the absence of atmosphere on the moon. Few existing propagation models were developed for communication on the earth and need to be reviewed for their applicability to the lunar wireless sensor network.

A. Irregular Terrain Model

Irregular Terrain Model (ITM) was suggested by Rice et al. [41] and is also known as Longley-Rice (LR) model. Hufford [42] shared that it can be used in area prediction mode and point-to-point mode. The ITM takes terrain and other parameters as inputs and produces the output as signal distribution in a given area. There are certain limitations of ITM, that it can be used for minimum antenna height of 0.5 metre and minimum communication distance of 1 km. The Point-To-Point (PTP) model given by Wong [43] is based on Longley-Rice model. The PTP model describes a method to obtain the diffraction loss and a general idea of calculating the diffraction loss may be obtained from this method for lunar application. The ITM model was suggested for terrestrial networks on the earth. As the lunar WSN involves

deployment of sensors on the ground with very small antenna heights, especially at 2.4 GHz operating frequency, the ITM cannot be used for such applications. Also, ITM considers atmospheric losses, which are not present on the moon. For any wireless system on the earth with communication distance of more than 1 km and incorporating antenna with a height of more than 0.5 metre at lower frequencies, this model may be useful.

B. Two-Ray Model

For a line-of-sight communication, a two-ray model was given by Neskovic et al. [44]. This theoretical model incorporates reflection by the reflection coefficient, which is calculated from the incidence angle, dielectric constant, surface conductivity and polarization of antenna. The signal strength at the receiver is shown in [45] using free space loss and reflection as

$$P_r = \frac{P_t G_t G_r \lambda^2}{16 \pi^2} \cdot \left| \frac{1}{d_1} \exp(-j k d_1) + \Gamma(\psi) \frac{1}{d_2} \exp(-j k d_2) \right|^2 \quad (2.1)$$

where d_1 and d_2 are the lengths of the first and the second path, respectively. The two ray model is mostly used for direct and ground reflected rays, having higher antenna heights for systems like television relay station on the earth. In case of lunar wireless sensor network, the sensor nodes are to be on the surface with very small antenna heights and therefore, two ray model may not give complete idea of the signal strength at the receiver.

C. Visual System Simulator Multipath Model

The signals, which are reflected from the reflectors, would reach the receiver with different strengths and phase angles; with respect to the direct signal. At the receiver, equivalent signal strength is given by superposition of many signals with varying amplitudes as well as phase angles. It is likely that the resultant signal strength may be reduced or increased as compared to the strength of the direct path. The multipath channel model in AWR VSS [46] is for the earth based systems, based on model like ITM. It is useful for

mobile systems on the earth environment and may be limited for its applicability to the moon, as is the case with ITM.

D. Willis Multipath Model

Willis [12] has given the extended version of two ray model as a multipath model for terrestrial application on the earth as

$$P_r = \frac{P_t G_t G_r \lambda^2}{16 \pi^2} \cdot \left| L_{d1} \Gamma_1(\psi_1) \frac{1}{d_1} \exp(-j k d_1) + \dots + L_{dn} \Gamma_n(\psi_n) \frac{1}{d_n} \exp(-j k d_n) \right|^2 \quad (2.2)$$

Willis model includes the diffraction losses for all multipath signals and does not include the direct path along with multipath signals, in a vector sum. It is useful for earth based systems mainly at lower frequency of operation. For lunar WSN at 2.4 GHz frequency, there can also be scattering losses at the reflectors, due to surface undulations. These losses are not taken into consideration in Willis model due to nature of its application. This model is basically for the earth based system, incorporating higher antenna heights and considering atmospheric losses. Hence, it cannot directly be applied to the WSN on lunar surface.

2.2 Wireless Channel Fading

Fading or small-scale fading in wireless communication indicates rapid fluctuations of amplitude, phase or delay of a radio signal over a short period of time or travel distance; in which large-scale path loss effects may be ignored. When a signal is transmitted, its multiple replicas may reach the receiver due to multiple reflections in the channel and resultant signal at the receiver can vary in amplitude and phase, depending on the signal strength and path delays of the waves and the transmitted bandwidth. In effect, multipath can cause the rapid variation in signal strength, changes in frequency due to Doppler shifts and delay spread.

Small-scale fading may be caused by (a) multipath propagation, (b) speed of reflectors, (c) speed of receiver and (d) transmitted signal bandwidth. The reflectors present in the channel can cause multiple replicas of the transmitted signal to reach the receiver, which are displaced with respect to one another in time and spatial orientation. The multipath creates Inter Symbol Interference (ISI) at the receiver due to multiple delayed versions of the transmitted signal. Whenever, a scatterer or a receiver is mobile, there can be random frequency modulation due to the Doppler shift. If the transmitted signal bandwidth is greater than that of the channel, the received signal will be distorted but signal strength will not fade much. If transmitted signal has narrow bandwidth as compared to the channel, the amplitude of the signal will change rapidly, but the signal will not be distorted in time.

Chukkala and Leon [47] have shown that two main communication issues with respect to channel evaluation are the link budget obtainable by propagation path loss or received power at a given location for a given transmitted power and the time dispersion of the transmitted bits due to multipath propagation. Multiple replicas of the transmitted bit arrive at different times after travelling through different paths and undergoing different path delays due to multipath effect. The time dispersion can be described by a Power Delay Profile (PDP). The time dispersive nature of multipath channel plays important role in deciding the maximum data rate that may be transmitted over a given channel without using a channel equalizer.

2.2.1 Fading Parameters [48]

The PDP is generally represented as a plot of relative received power as a function of excess delay of multipath with respect to the delay of direct or line-of-sight path. The PDP is found by averaging instantaneous PDP measurements over a local area. Mean excess delay, rms delay spread and excess delay spread (X dB) are defined as multipath channel parameters obtainable from a PDP. The mean excess delay is first moment of a PDP and given as

$$\bar{\tau} = \frac{\sum_k P(\tau_k) \tau_k}{\sum_k P(\tau_k)} \quad (2.3)$$

The rms delay spread is defined as square root of second central moment of a PDP given by

$$\sigma_\tau = \sqrt{\overline{\tau^2} - (\bar{\tau})^2} \quad (2.4)$$

where

$$\overline{\tau^2} = \frac{\sum_k P(\tau_k) \tau_k^2}{\sum_k P(\tau_k)} \quad (2.5)$$

The maximum excess delay (X dB) of a PDP is defined to be the time delay during which multipath power falls to X dB down the maximum or it is defined as $\tau_X - \tau_0$ where τ_0 is delay of the first or line-of-sight or direct signal and τ_X is the maximum delay at which multipath signal is within X dB of strongest arriving multipath signal (not necessarily at τ_0).

The PDP and spectral response (or magnitude frequency response) of a given multipath channel are a Fourier transform pair. The coherence bandwidth (B_c) is used to characterize the channel in frequency domain and it is a statistical measure of the range of frequencies over which the channel can be considered as ‘flat’ channel. The coherence bandwidth is a range of frequencies over which any two frequency components have better potential to be amplitude correlated. Though, the exact relationship between B_c and σ_τ is a function of applied signal and specific channel response, if the coherence bandwidth is defined for frequency correlation function as greater than 0.9, then

$$B_c \approx \frac{1}{50 \sigma_\tau} \quad (2.6)$$

and if the frequency correlation function is above 0.5 then

$$B_c \approx \frac{1}{5 \sigma_\tau} \quad (2.7)$$

The Doppler spread and coherence time provide information about the time varying nature of channel caused by motion of either the receiver or scatterers in the channel. The

Doppler spread (B_D) is defined as the range of frequencies over which the received Doppler spectrum (or received signal spectrum) is essentially non-zero. When single frequency component with frequency f_c is transmitted, the Doppler spectrum will have spectrum in the range from $f_c - f_d$ to $f_c + f_d$, where f_d is the Doppler shift, defined as

$$f_d = \frac{v \cos\theta}{\lambda} \quad (2.8)$$

with v as velocity of a mobile, λ as wavelength of transmitted signal and θ as angle between the line joining the source with the mobile and the direction of motion of the mobile.

The coherence time (T_C) is the time domain dual of the Doppler spread and is used to characterize the time varying nature of frequency dispersiveness of the channel in the time domain. The Doppler spread and coherence time are inversely proportional to each other

$$T_C \approx \frac{1}{f_m} \quad (2.9)$$

The coherence time is the time duration over which two received signals have a strong potential to be amplitude correlated and it is a statistical measure of the time duration over which the channel impulse response is essentially invariant, quantifying the similarity of the channel response at different times. If the reciprocal of the signal bandwidth is greater than the coherence time, the distortion occurs at the receiver. If the coherence time is defined for time correlation function above 0.5, then

$$T_C \approx \frac{9}{16 \pi f_m} \quad (2.10)$$

where f_m is the maximum Doppler shift given by $f_m = v/\lambda$. As per popular rule of thumb for modern digital communications, the coherence time is given by geometric mean of Equation (2.9) and Equation (2.10) as

$$T_C = \sqrt{\frac{9}{16 \pi f_m^2}} = \frac{0.423}{f_m} \quad (2.11)$$

The coherence time indicates that any two signals arriving with a time separation greater than the coherence time are affected differently by the channel.

2.2.2 Multipath Fading [48]

Multipath delay spread leads to time dispersion and frequency selective fading in a wireless communication system. If a mobile radio channel has a constant gain and linear phase response over a bandwidth greater than the transmitted signal bandwidth, then the received signal will undergo flat fading. In such a case, spectral characteristics of the transmitted signal are preserved at the receiver but the strength of the received signal changes with time due to fluctuations in the gain of the channel caused by multipath. The flat fading channels are also known as amplitude varying channels and are sometimes referred to as the narrowband channels, since the bandwidth of the transmitted signal is narrow as compared to the channel flat fading bandwidth. Thus, a signal undergoes flat fading if

$$B_S \ll B_C \quad \text{and} \quad T_S \gg \sigma_\tau \quad (2.12)$$

where T_S is symbol period and B_S is bandwidth, respectively of the transmitted modulation, and σ_τ and B_C are the rms delay spread and coherence bandwidth, respectively of the channel.

If the channel possesses a constant gain and linear phase response over a bandwidth that is smaller than the bandwidth of the transmitted signal, then the channel creates frequency selective fading on the received signal. In such a case, the channel has a multipath delay spread greater than the reciprocal bandwidth of the transmitted signal and the received signal comprises of multiple replicas of the transmitted signal attenuated or faded and delayed in time, causing distortion in the received signal. Frequency selective fading occurs due to time dispersion of transmitted symbols within the channel, leading to ISI. The frequency selective fading channels are also known as wideband channels since the signal bandwidth is wider than the bandwidth of the channel impulse response. As time varies, channel varies in gain

and phase across the spectrum, resulting in time varying distortion in the received signal. Thus, a signal undergoes frequency selective fading if

$$B_S > B_C \quad \text{and} \quad T_S < \sigma_\tau \quad (2.13)$$

The small scale fadings due to multipath delay spread are shown in Figure 2.3.

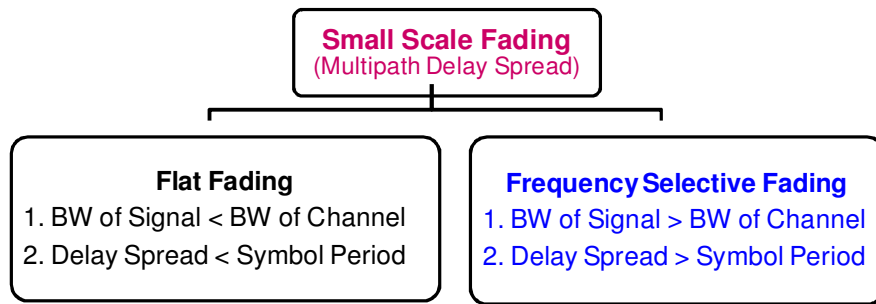


Figure 2.3: Small scale fading due to multipath delay spread.

2.2.3 Doppler Fading [48]

If the coherence time of the channel is smaller than the symbol period of the transmitted signal, then the channel is called fast fading channel. This results in frequency dispersion (also called time selective fading) due to the Doppler spreading, leading to signal distortion. Thus, a signal undergoes fast fading if

$$T_S > T_C \quad \text{and} \quad B_S < B_D \quad (2.14)$$

Fast fading only deals with the rate of change of the channel due to motion and it does not specify either flat or frequency selective channel. In practice, fast fading only occurs for very low data rates.

If channel impulse response changes at a rate much slower than the transmitted baseband signal, then it is called slow fading channel. In this case, the channel may be

assumed to be static over one or several reciprocal bandwidth intervals and implies that the Doppler spread of the channel is much less than the bandwidth of the transmitted signal. Thus, a signal undergoes slow fading if

$$T_S \ll T_C \quad \text{and} \quad B_S \gg B_D \quad (2.15)$$

The small scale fadings due to the Doppler spread are shown in Figure 2.4.

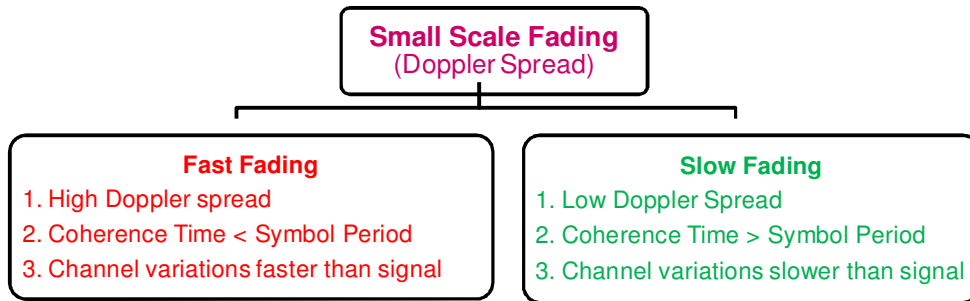


Figure 2.4: Small scale fading due to Doppler spread.

In case of a wireless sensor network on surface of the moon, the reflectors found are steady and the rover normally moves with very low velocity (of the order of a few cm per second). Hence, the Doppler spread is not anticipated (e.g. 0.08 Hz for rover velocity of 1 cm/s) and the multipath fading is a major challenging problem. All types of fadings are shown in Figure 2.5 as a function of symbol period.

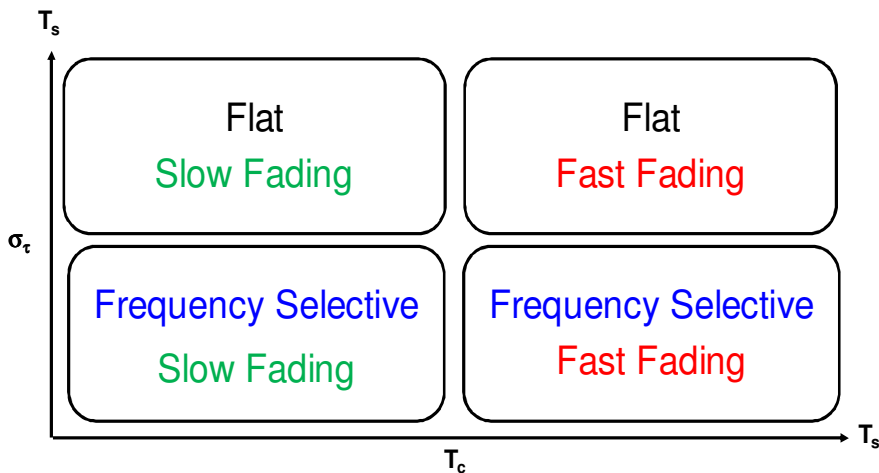


Figure 2.5: Various fadings as a function of symbol period.

It is given by Chuang [49] that for several modulation types such as Binary Phase Shift Keying (BPSK), QPSK, Offset QPSK (OQPSK) and Minimum Shift Keying (MSK); the average irreducible Bit Error Rate (BER) has been shown to become larger than 10^{-3} , when the rms delay spread exceeds 10 % of the symbol period and equalization is not used.

Therefore, as a general rule, the maximum data rate with acceptable BER performance is limited to $0.1/\sigma_\tau$ for a frequency nonselective channel, when using a receiver which does not employ an equalizer to combat the effects of multipath fading.

2.2.4 Rayleigh Fading Distribution [48]

In mobile radio channels, the statistical time varying nature of the received envelope of a fading signal or the envelope of an individual multipath component is commonly described by the Rayleigh distribution. The Rayleigh distribution has a probability density function (pdf) given by

$$p(r) = \begin{cases} \frac{r}{\sigma^2} \exp\left(-\frac{r^2}{2\sigma^2}\right) & (0 \leq r \leq \infty) \\ 0 & (r < 0) \end{cases} \quad (2.16)$$

where σ is the rms value of the received voltage signal before the envelope detection and σ^2 is the time-average power of the received signal before the envelope detection.

2.2.5 Rician Fading Distribution [48]

When there is a dominant signal component present in the channel, such as a line-of-sight propagation path, the small-scale fading envelope distribution is Rician. In such a case, random multipath components arriving at different angles are superimposed on a dominant signal and at the output of an envelope detector; a dc component is added to the random

multipath. The Rician distribution degenerates to a Rayleigh distribution when the dominant component fades away. The Rician distribution is given by

$$p(r) = \begin{cases} \frac{r}{\sigma^2} \exp\left(-\frac{(r^2 + A^2)}{2\sigma^2}\right) I_0\left(\frac{Ar}{\sigma^2}\right) & (A \geq 0, r \geq 0) \\ 0 & (r < 0) \end{cases} \quad (2.17)$$

The parameter A denotes the peak of dominant signal and $I_0(\cdot)$ is the modified Bessel function of the first kind and zero order. The Rician distribution is often described in terms of a parameter K , which is defined as the ratio of power in direct path and that in the multipath.

Figure 2.6 shows the Rician pdf with $A = \nu$, varying from 0 (Rayleigh) to 4.

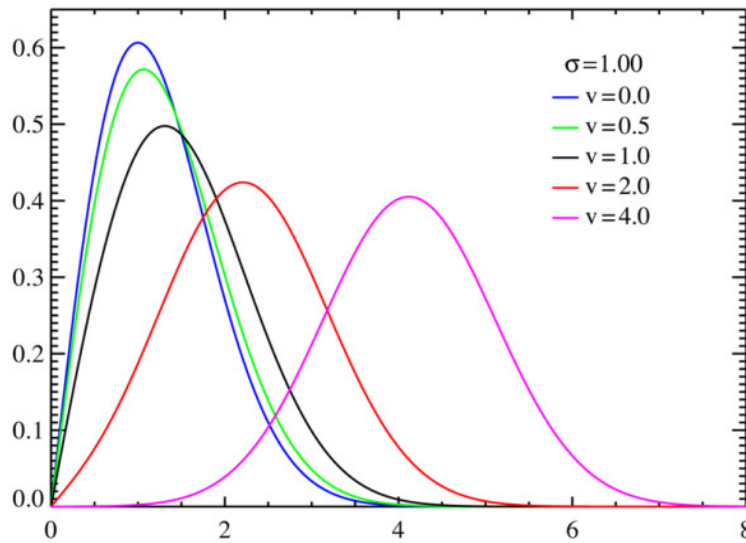


Figure 2.6: Probability density function of Rician distribution (Courtesy: http://en.wikipedia.org/wiki/File:Rice_distributiona_PDF.png).

For a wireless sensor network on the lunar surface, the deployed sensors are like Unattended Ground Sensors (UGSs), as there is no control after the deployment on the moon and hence the network becomes like a UGS network. Under this scenario, there is a possibility of direct signal component at the receiver, whose further justifications are given in Chapter 4, creating the Rician distribution due to superimposition of multipath above the direct path signal.

2.3 Lunar Surface Science

Lunar surface science is the study of physical, chemical and thermal properties of the surface as well as subsurface materials of the moon. There are mainly two types of regions, viz., (a) Mare type, where the regions are relatively flat and have few craters and (b) Highland type, where the surface is relatively rough and is heavily cratered. The top layer of the lunar surface has very fine soil, called regolith. As given in [50], regolith may be defined as the layer or mantle of loose incoherent rock material, of whatever origin, that nearly everywhere underlies the surface of the land and rests on bedrock. The regolith may be formed in place or transported from adjacent lands. The regolith is surficial layer covering the entire lunar surface ranging in thickness from metres to tens of metres and formed by impact process. The particles range from enormous boulders to micron-sized ones. The lunar surface is a complicated environment produced by impact and space weathering processes over billions of years and continually modified.

Few properties falling under lunar surface science are particle size, bulk density and porosity of the regolith; surface and subsurface temperatures, thermal conductivity; permittivity and electrical conductivity of the regolith etc. Measurement of most of these properties requires either sample return missions to perform experiments in the laboratory or in-situ measurements on lunar surface. For in-situ measurements, it is necessary to understand the moon environment.

2.3.1 Moon Environment

The moon has an atmosphere, so tenuous as to be nearly vacuum, with a total mass of less than 10 metric tons [51]. The surface pressure of this small mass is around 3×10^{-15} atm. Its sources include outgassing and sputtering, the release of atoms from the bombardment of lunar soil by solar wind ions [52, 53]. Water vapour has been detected by Chandrayaan-1 and found to vary with latitude, with a maximum at about 70 degrees. It is possibly generated

from the sublimation of water ice in the regolith [54]. These gases can either return into the regolith due to the moon's gravity, or be lost in space, either through solar radiation pressure, or if they are ionized, by being swept away by the solar wind's magnetic field [55].

The insolation due to the sun is known to the hardware designers or during conducting operation in the earth's orbit or in deep space. The sun radiates as a black body at an effective temperature of 5777 K [56] and the solar constant at 1 Astronomical Unit (AU) is about 1367 Watt per square metre. One AU is defined as a unit of length equal to about 149,597,870.7 km [57] or approximately the mean earth-sun distance. The maximum solar constant on the earth is 1413 Watt per square metre and the minimum solar constant is 1321 Watt per square metre, due to the earth's elliptical orbit; varying distance from the sun between 0.9833 AU and 1.017 AU [58]. The average distance from the earth to the moon is about 384, 403 km [59] and hence the nearest distance from the sun to the moon is about 149, 213, 467 km, which is about 1 AU. Therefore, the solar constant on the moon is also about 1367 Watt per square metre. Most of the radiant energy from the sun is in visible and near infrared ranges of the electromagnetic spectrum. The sun also radiates energy in Ultra Violet (UV), X-ray and gamma ray ranges.

As given in [56], the cosmic microwave background has a temperature of 2.7 K and it is a thermal radiation heat sink. The Milky Way immerses the moon in a constant flux of Galactic Cosmic Rays (GCRs). GCRs are high energy charged particles that enter the solar system from the galaxy. They are composed of protons, electrons and fully ionized nuclei of light elements. Most GCRs have energies too low to penetrate the earth's atmosphere, but all of them strike the moon. The moon has no magnetic field to deflect the GCRs and the lunar atmosphere is too thin to materially affect the incoming GCRs. Material shielding may be partially effective against GCRs in certain energy ranges, but may actually aggravate the problem for some of the higher energy rays as more shielding causes an increased amount of secondary radiation. The best shielding strategy appears to be structural shielding combined with highly hydrogenated materials such as water or plastic.

As mentioned by Mendell [56], the sun continually emits streams of plasma (a mixture of ions and magnetic fields) at high speed into the solar system. The flow is called the solar

wind and the moon, having no global magnetic field, poses a solid dielectric obstacle to it. The magnetic field passes through the moon but the particles impact the surface, burying themselves into surface grains. In addition to the planets, a large number of bodies ranging from comets and asteroids to submicroscopic dust particles orbit the sun. A solid body, as small as submicron, can impact the surface of the moon and affect the surface in some way. Most meteoroids, even large ones, burn up in the earth's atmosphere; but on the moon, all impactors make some kind of crater and spray ejecta. The lunar surface layer, the regolith, has been formed by impacts over geological time. Micrometeoroid impacts melt or vaporize the individual grains and deposit the residue on nearby grains. They may also weld the individual grains into fragile glassy structures, called agglutinates. Due to plasma of the solar wind and bombardment by UV radiation, charge state varies across the surface depending upon whether the surface is illuminated or not. On the day side, photon flux dominates; causing ejection of photoelectrons and the surface acquires a net positive charge. The surface potential grows more negative towards the terminator. At the terminator and on the night side, the charge becomes negative with a positive sheath. The charge on the day side is about 10 to 18 Volt positive and on the night side, it is about 10 Volt negative; directed outward. At the poles, the constant low sun angle and complex topography create a patchwork of light and shadow, making prediction of charging difficult.

Small dust particles may be mobilized by naturally occurring electric fields on the moon [56]. Dusty regolith particles accumulate charge through grain-grain contact and through contact with various surfaces. The low electrical conductivity of the regolith allows individual dust grains to retain electrostatic charge. The charged dust grains follow ballistic trajectories, subsequent to being accelerated upward through a narrow sheath region by the surface electric field. Dust fountain model for the maximum dust grain as a function of angle from subsolar point is given by Stubbs et al. [60].

As given in [56], the length of a lunation (time for successive zenith passage of the sun, i.e., noon) is 29.53 earth days and the obliquity of the moon (tilt of its spin axis from the ecliptic pole) is 1.5 degree. The disk of the earth in the sky as seen from the moon is about 4 times the solid angle of the disk of the moon as seen from the earth and the earth is more reflective than the moon. The light from earthshine is brighter than the light from the moon.

On new moon, one can see the old moon in the arms of the new moon. The unlit portion of the moon is illuminated by earthshine. Some seismic activities were observed by Apollo seismometers. The moon is extremely stable against moonquakes, in general. The gravity of the moon is very low as one sixth of that of the earth. The value of the acceleration of gravity is 1.62 metre per square second and escape velocity is 2.37 kilometre per second [1]. The sunlight gets reflected from the moon and reflectance increases from blue to red with further increase in the near infrared. The lunar surface has unusually low thermal inertia and large variation in temperature is almost completely damped within the first metre of the surface. The low thermal inertia means that the upper surface temperature quickly comes into radiative equilibrium with incident insolation and cools dramatically when it is removed. Rocks have much higher thermal inertia than the soil.

Thus, there are many effects on the moon like reflection of sunlight, thermal emission from solar heating, ejecta from impacts, neutrons generated in the surface layer by GCR, charging of the surface through interaction with the plasma environment, very minor seismic activities and dust levitation.

Direct earth communication on non-polar regions is continuous on the near side of the moon and relay satellite is needed for the far side [1]. For polar regions, direct communication with the earth is discontinuous but predictable and almost half the time is in the earth view. The temperature in non-polar region is about -150° to $+100^{\circ}$ C (123 to 373 K) [1], while the temperature in the polar region is about -50° C or 223 K (sunlit area) to -200° C or 73 K (dark area). Considering the method in [3] and maximum solar constant of 1413 Watt per square metre, the highest temperature on moon is expected to be about $+125^{\circ}$ C. The minimum temperature on the moon may be about -270° C [3].

2.3.2 Lunar Surface Properties

There are many properties of the lunar surface and main properties of interest are the ambient light, surface and subsurface temperatures and permittivity. The sensors for all these

properties are light sensor or photodiode, Resistor Temperature Detector (RTD) or thermocouple and electrical property sensor or impedance sensor, respectively.

A. Ambient Light

As discussed in Subsection 2.3.1, the solar constant on the moon is about 1367 Watt per square metre and it may vary from 1321 to 1413 Watt per square metre, approximately depending on the distance of the moon from the sun. Considering luminous efficacy of the sun as 98 lumen per Watt [61], the illuminance on the moon is found as 133.966 klux. This suggests that a light sensor [62] with a minimum capacity of 140 klux should be used for detection of light on the moon. An appropriate photodiode may be used as one of the sensors in lunar WSN, for detection of light on the moon.

B. Temperature

The temperature on the moon may vary from about -200°C to $+125^{\circ}\text{C}$ and hence appropriate temperature sensor in this range may be used for the measurement. Platinum Resistance Thermometer (PTR) PT100 [63] with range of -200°C to $+850^{\circ}\text{C}$ may be used for such applications. The other choice is either a T type copper-constantan thermocouple [64] with temperate range from -200°C to $+350^{\circ}\text{C}$ or a chromel-gold/iron type thermocouple [65] with temperature range from -271°C to $+327^{\circ}\text{C}$ for such applications. The T type copper-constantan thermocouple has an advantage that it is nonmagnetic and hence it is not affected by the Curie temperature.

C. Permittivity

The permittivity [66] is a function of frequency, in general. Permittivity of water has been reported by Batalioto et al. [67] and Grasso et al. [68], while permittivity of water ice is suggested by Seshadri et al. [69]. Typically relative permittivity of water at room temperature is 80 in low frequency range [67]. The relative permittivity of lunar soil is reported as about 4

to 8 in the literature [70, 71]. The permittivity of wet soil is reported by Dam et al. [72]. Experimental evidence indicates that permittivity of ice may be considered independent of both, temperature (below 273 K) and frequency, in the microwave range and may be assigned a constant value of 3.15 [73]. However, at lower frequency in the kHz range, permittivity of ice depends considerably on temperature. Also, there is a difference in the upper knee point frequencies in the real permittivity plots of water and ice, as shown by Stacheder [74]. The upper knee point in the real permittivity plot of ice could vary depending on temperature from less than 1 Hz [75] in colder region of the moon to 1 kHz [74] at 273 K. The transition region (from upper knee point frequency to lower knee point frequency) of real permittivity of ice is comparatively in lower frequency range from few Hz to few kHz and it shifts right or left depending on increase or decrease in the temperature. Typical transition regions of the permittivity of ice are from 90 (at 1 kHz) to 4 (at 100 kHz) at 273 K temperature [74] and from 92 (at 100 Hz) to 4 (at 3000 Hz) at about 260 K temperature [75]. Few water detection techniques or sensors are described in Section 2.5 in this chapter. One new entry in the domain is the Wireless Impedance Sensor Node (WISN), which is suggested for in-situ exploration of water ice on the moon due to its many advantages, as shown in Chapter 5.

2.3.3 Lunar Soil Simulant

A new lunar simulant JSC-1 [76] was developed under the auspices of the NASA Johnson Space Center. JSC-1 [76] is a glass-rich basaltic ash, which approximates the chemical composition, mineralogy, particle size distribution and engineering properties of lunar mare soil. JSC-1 [76] was produced specifically for large and medium scale engineering studies in support of future human activities on the moon. Such studies include material handling, construction, excavation and transportation. The simulant is also appropriate for research on dust control, spacesuit durability and agriculture. JSC-1 [76] was mined from a volcanic ash deposit located in the San Francisco volcano field near Flagstaff, Arizona. Lunar soil simulant JSC-1A [77] is similar to JSC-1 [76].

2.4 Wireless Technology for Space Science and Applications

With the advancement of wireless technology, smart sensing devices and inquisitiveness; applications of wireless sensors and their networks are sought for space sciences and technologies, either to explore beyond the awareness of human kind or to monitor the performances of sophisticated systems. Most planetary applications have been achieved using remote sensing techniques through orbiter. The possibility of using wireless devices for in-situ measurements in planetary application is a new application of WSN for planetary surface science. European Space Agency (ESA) identifies five wireless applications for space as given by Magness and Plancke [78]. These are (a) Microsensor Proximity Networks, robotic in-situ sensing for planetary exploration by fixed nodes; (b) Intra-Spacecraft Proximity Networks, robotic in-situ sensing for spacecraft health (e.g. temperature sensor for real time cabin temperature measurement) or astronaut health monitoring (e.g. gas sensor to measure oxygen); (c) Inter-Vehicular Proximity Networks, robotic in-situ sensing for planetary exploration using mobile nodes; (d) Extra-Vehicular Activity Proximity Networks, data delivery for EVA and (e) Advanced Science Proximity Networks, mobile planetary micro-sensors. All these are short-range RF wireless (proximity) network technologies for space applications. Daga et al. [79] have done the terrain based simulation of IEEE 802.11 a and b physical layers on martian surface and many other works related to wireless technology for the mars have been reported in literature [47, 80-82]. Leon et al. [83] have described in an annual report of NASA about the effective utilization of commercial wireless networking technology in planetary environments. The WSN can also be useful to ensure overall mission success in space applications. For instance, space crew health performance can be tracked down using telemedicine, without assistance of a doctor, by taking advantage of sensor local processing and telecommunications. On the other hand sensors can be deployed within the spacecraft to implement integrated health monitoring system. Also, in-situ health monitoring and temperature and pressure monitoring may be achieved by wireless devices [84]. In [85], spacecraft applications of motes are considered and a set of requirements is identified. Also, selected mote kits are tested under various scenarios complying with spacecraft testing procedures and details of results of functional,

ElectroMagnetic Interference (EMI)/ElectroMagnetic Compatibility (EMC), vibration, thermal and radiation tests are discussed. Thus, the scope of WSN and the wireless devices may extend beyond the earth to many space applications. Highly motivated researches are needed to overcome challenges involved in space applications before actual accomplishment.

Dubois et al. [86] have discussed the ad hoc wireless sensor networks for exploration of solar-system bodies and presented various advantages of WSN. They describe that various constraints are associated with such systems. Environmental constraints include hostile temperature, pressure, irradiation, shocks at separation stages and vibrations at launch. Operational constraints include physical channel, power consumption issues, energy source issue, EMC issue with other systems in the environment and localization of sensors in the environment. These operational constraints are:

- Physical channel: In many of the space exploration scenarios, the overall foot print of the network can be up to 100 x 100 square km. If nodes are capable of communicating over a distance of a few 100 m, this would largely limit the scenario where the WSN can be applicable. The frequency band, type of modulation, emission power and communication protocol strongly impact the performances of the WSN.
- Power consumption issues: All the options to achieve low power consumption in a WSN have to be considered as shown in [87-89]. These are dynamic power management/sleeping mode, carrier frequency/antenna size and gain, low power electronics, modulation/multiple access techniques and communication protocol/error control techniques. Many scenarios for data acquisition by the WSN in space exploration have a low sampling rate.
- Energy source issues: Depending on the mission and objectives, energy could be either harvested from the environment or/and stored in batteries. Energy harvesting is more complex than the use of batteries. The first WSN sent into space will be more reliable if batteries are used. Long duration mission will benefit most from harvesting technology. In the solar system, the most common source of energy that can be harvested is sunlight. Vibration energy or thermal gradients are much more difficult to harness.

- EMC issues with other systems in the environment: In space exploration, normally there are no EMC perturbations coming from other systems in the environment, besides the space craft. Furthermore, there are few limitations in the frequency band or emission power that can be used. There have been some discussions regarding frequency allocation for space communication between NASA, ESA, and JAXA, but this imposes very few limits on WSN.
- Localization of the sensors in the environment: In most missions, the localization of each node is essential in order to know where each measurement has been made. The node distribution method will strongly influence the localization technique as shown in [90]. In some missions, nodes move relative to each other and therefore their position would have to be updated frequently, i.e., continuous localization. Different localization techniques exist, but they have rarely been implemented on small size sensing nodes used in WSN and would have to be developed further. It is shown in [91-95] that RF electromagnetic wave propagation delay, RF signal strength, RF wave angle of arrival and Pulsed LIDAR can be used as localization techniques in WSN for space exploration. The localization process can be intrinsic to the network or external or a combination. For space exploration, the most promising localization techniques are based on pulsed LIDAR or RF waves.

2.5 In-Situ Exploration of Water Ice

Many techniques and sensors have been reported in the literature for detection of water in the universe. LCROSS [96] to the moon targeted (i) detection of water ice using near InfraRed (IR) spectroscopy of the scattered sunlight absorption features of water ice, (ii) detection of near IR spectra of H₂O vapor (sublimed ice) emission bands at 1.4 μm and 1.8 μm and fundamental bands near 3 μm from ground based 10 m class telescopes, (iii) measurement of an extended OH⁻ atmosphere via spectroscopy at the 308 nm OH⁻ band at UV wavelength along with nearby scattering continuum, (iv) spectroscopy covering the 619 nm H₂O⁺ band as well as adjacent scattering continuum and (v) narrow band imaging at mid IR

wavelengths to follow thermal evolution of plume and newly deposited regolith, which could be affected by water vapor in the ejecta.

The MSP LIDAR system [97] set up in a densely populated suburban area, was upgraded to a Raman LIDAR operating on the basis of inelastic photon scattering in the atmosphere. It could monitor aerosol, nitrogen and water vapor concentrations up to an altitude of 6 km in the troposphere. It is reported that in addition to aerosol backscatter observations; measurements of atmospheric extinction coefficients, extinction-to-backscatter ratios and the water vapor mixing ratio at the planetary boundary layer can also be determined. Spectroscopic water vapor detection using asynchronous THz sampling by means of a fiber-coupled Tera Hertz (THz) transmitter and receiver pair has been shown by Brown et al. [98]. Silver and Hovde [99] describe a laser-based hygrometer for ambient water vapor monitoring, which uses a fiber-optic coupled near IR diode laser in conjunction with high frequency wavelength modulation spectroscopy. Their instrument was extremely compact using little power and exhibited high detection sensitivity. The instrument was flown on a KC-135 aircraft for a period of six months and measured frost points at altitudes between 10000 and 40000 feet. The water detection sensitivity corresponds to a volume mixing ratio of 8 ppmV.

In situ measurements of H₂O from a stratospheric balloon by absorption spectroscopy near 1.393 μm by means of a distributed-feedback InGaAs laser diode has been shown by Durry and Megie [100]. To obtain high dynamic range for the measurements, required for continuous water vapor monitoring in the upper troposphere and the lower stratosphere, they used a circuit to combine differential and direct detection. They have reported absorption spectra of H₂O in the 5-30 km altitude range obtained at 1 second intervals. They retrieved water vapor mixing ratios from the absorption spectra by a fit to the full molecular line shape in conjunction with in-situ pressure and temperature measurements, with a precision error ranging from 5 % to 10 %.

Webster et al. [6] designed and built IR based laser hygrometer using Tunable Diode Laser (TDL) for measuring in-situ water vapor mixing ratio either in the atmosphere of the mars or thermally evolved from martian soil or ice samples. Their laser hygrometer used a

thermoelectrically cooled single-mode distributed feedback TDL at $1.87 \mu\text{m}$ to scan over a selected vibration-rotation line of both H_2O and CO_2 near 5327.3 cm^{-1} . A working prototype weighing only 230 g and consuming less than 3 Watt power had been built and used to generate spectra, whose analyses demonstrated precision sensitivities as fine as 1 part in 10^6 by volume in 1 second or 0.1 part in 10^6 in 10 second at martian pressures and temperatures. The total path length was 55.27 cm in 10 pass optical configuration and the length of the cell was restricted to 10.16 cm diameter probe.

In-situ exploration of water ice, mixed with any soil, requires the use of a water ice sensor in conjunction with other processing electronics. Existing water sensors are mostly based on either reflectometry principle or InfraRed (IR) spectroscopy. They use some portion of the EM spectrum for detection and are described in Subsection 2.5.1. However, there is also a possibility of using some other part of the EM spectrum for sensor design, in principle. The water sensor may be based on optical reflection or microwave absorption technique. The optical reflection and microwave absorption techniques are described in Subsection 2.5.2. The impedance sensor based on impedance spectroscopy, described in Chapter 5, is a promising sensor to detect the presence of water ice and it is very useful for future space and planetary applications.

2.5.1 Existing Water Sensors

There are mainly two categories of existing water sensors. One is based on reflectometry principle and the other is based on infrared spectroscopy. The infrared spectroscopy based sensor may have to be integrated with other subsystems for planetary applications.

A. Reflectometry Sensor

A reflectometry based soil moisture sensor may transmit a short rise time pulse or a sinusoid of single frequency along the conductor, called probe. If the conductor is uniform

and properly terminated, the entire transmitted pulse will be absorbed in the far-end termination and no signal will be reflected toward the sensor. Any discontinuity will cause some of the incident signal to be sent back toward the source. Increase in the impedance creates a reflection that reinforces the original pulse, whilst decrease in the impedance creates a reflection that opposes the original pulse. The pulse velocity is primarily affected by permittivity of the medium through which the pulse propagates. The resulting reflected pulse is measured and because the speed of signal propagation is relatively constant for a given transmission medium, it can be read as a function of cable length. Such a sensor is shown in Figure 2.7 in which a cable may be used for data transmission in terrestrial applications, while an antenna may be used for wireless mode in space applications. Such sensors [9, 101] generally have long probe (of the order of few cm) and the probe needs to be inserted inside the soil completely, for its efficient use. This indicates that, if such sensors are to be used for space applications, then they can have long dimension due to the long probe length. Also, there should be a mechanism to insert the probe inside the surface and hence, it needs extra energy for insertion in the lunar surface. Also, such sensors use operating frequency in the MHz range, at which there is an ambiguity in differentiating between the dry regolith and ice, since the permittivity of regolith and ice are almost comparable in this range.

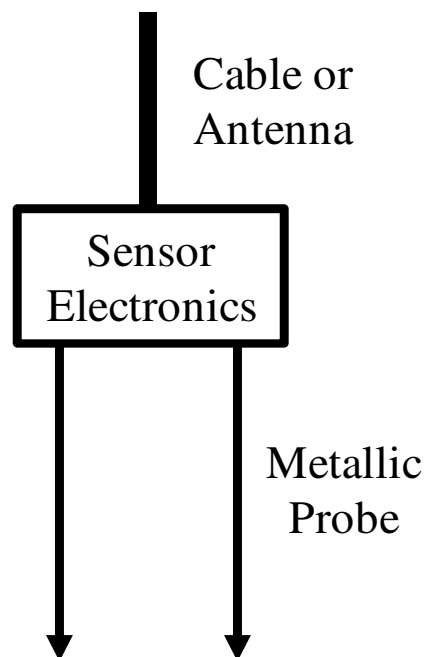


Figure 2.7: Reflectometry based soil moisture sensor.

B. Infrared Sensor

Infrared spectroscopy [102] can use signal ranging from 0.7 μm to 1000 μm and IR does not possess enough energy to induce electronic transitions. Therefore, absorption of IR is restricted to compounds with small energy differences in possible vibrational and rotational states. For a molecule to absorb the IR, vibrations or rotations within a molecule must cause a net change in dipole moment of the molecule. Alternating electrical field of radiation interacts with the fluctuating dipole. If the frequency of radiation matches the vibrational frequency of the molecule, then the radiation will be absorbed, causing a change in the amplitude of molecular vibration. Positions of atoms in molecules are not fixed and are subject to a number of different vibrations. Vibrations fall into two main categories of stretching and bending. Water has three vibrational frequencies at 3651.7 cm^{-1} , 1595.0 cm^{-1} and 3755.8 cm^{-1} . The measurement using IR spectroscopy is based on Beer-Lambert law.

Assuming water is present in the form of ice at very low (about 80 K) temperatures on the moon, it must be converted into vapor for detection by IR technique. Sublimation of an element or compound is a transition from solid to gas phase with no intermediate liquid stage, which occurs at temperature and pressure below triple point. Figure 2.8 (a) shows phase diagram and triple point of water. Sublimation is an endothermic change and snow as well as other water ices also sublime, albeit more slowly, at below-freezing temperatures. Hence, energy needs to be given to sublime the ice and make vapor. Figure 2.8 (b) shows conceptual design of IR sensor which uses a DC motor driven sampling drill. Energy for sublimation of water ice may be generated by sampling drill itself, avoiding any additional source of heat. Such sampling drill should be hard enough to be able to make a hole in the surface and should be hollow from inside, to collect the sample. It generates heat when in operation and this heat energy can be used for sublimation of ice to make the water vapor for detection. The generated vapor is collected in test chamber having two lasers (or LEDs), one in-band and the other out of band. To measure the absorption spectrum of water at 1.86 μm ; one laser at 1.86 μm and the other at 1.6 μm may be used in the test chamber, which can be responded by a photodiode [103]. Whenever water vapor is present inside the chamber, in-band signal is

absorbed while out of band signal is not absorbed; and if no vapor is present, both signals are detected by photodiode. Thus, the presence of water can be found by this technique.

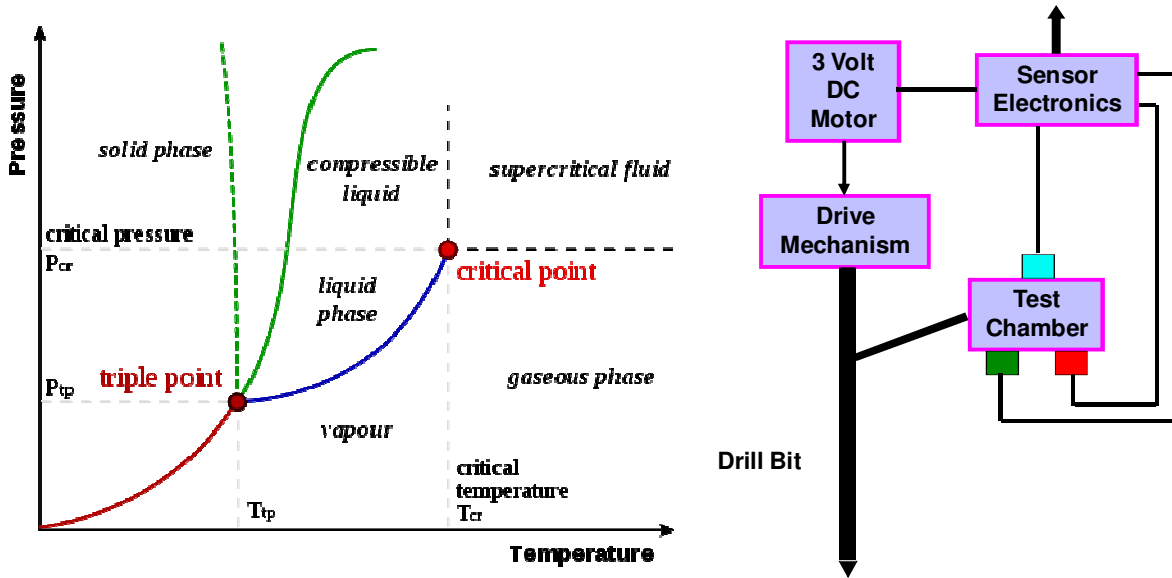


Figure 2.8: (a) Phase diagram of water (Courtesy: <http://en.wikipedia.org/wiki/File:Phase-diag2.svg>) and (b) Conceptual design of IR sensor.

2.5.2 Additional Water Sensors

There are two additional techniques, based on which a water sensor may be made. The first suggested technique is optical reflection, which is used in chilled mirror hygrometer [104]. The other is absorption of microwave by water at absorption frequency. Optical sensor and microwave sensor based on these techniques have to be developed for water detection.

A. Optical Sensor

The optical sensor is quite similar to the IR sensor in construction, having sampling mechanism. However, inside surfaces of the chamber are kept highly polished and optical source and detector are mounted instead of IR devices. After water vapor is created due to sublimation of water ice by the sampling drill, it is collected in the sample chamber. If either

the temperature of small chamber is decreased or the pressure inside is increased, frost will be deposited on top (and other) surface(s) of the chamber. This can be understood by phase diagram of water as shown in Figure 2.8 (a). The operation is near the triple point of water and water vapor is directly converted into water ice without going through liquid phase. Optical signal generated from the source gets reflected from top surface under this condition of deposited frost on the surface and will have lesser intensity than without frost, which can confirm presence of water ice.

Decrease in temperature may not actually be needed by special means, as dark regions on the moon have very low temperatures. Increase in pressure is achieved by generating more number of molecules using the drilling system, operating for longer period. In fact, this sensor may be combined with IR sensor for detection of water ice, if desired. The arrangement of optical sensor is shown in Figure 2.9.

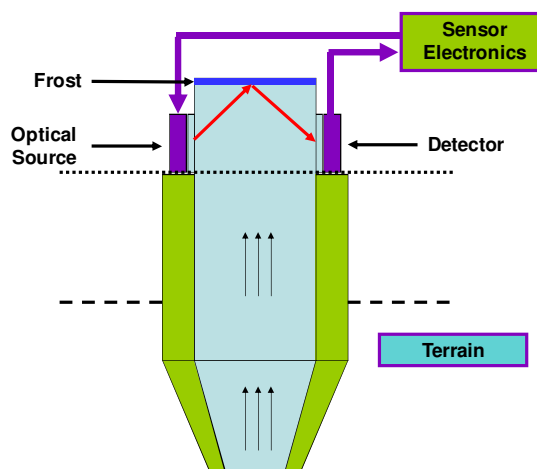


Figure 2.9: Conceptual design of optical water ice sensor.

B. Microwave Sensor

It is known that microwave signals are attenuated when they pass through the environment with moisture. Also, microwave propagation inside a waveguide is known to be dependent on dielectric, filled inside the guide. The soil is a dielectric material, which can modify the wave propagation in the waveguide. This indicates that if moisture is present in

the soil, the signal should be affected. The detection of water and measurement of soil property in RF and MW ranges have been reported in the literature [105-109].

To study MW detection of soil moisture, a C-band microwave waveguide was designed and developed [110]. The waveguide was tested using a microwave Vector Network Analyzer (VNA) in 5 to 6 GHz frequency range after filling with various types of soils. It was found that signal attenuation was dependent on moisture content and the type of soil.

The idea for miniaturized sensor is to use a microwave source on one side of the waveguide and a microwave detector on the other side. The block diagram of MW sensor is shown in Figure 2.10. Such sensor needs scooping mechanism to fill soil inside the waveguide.



Figure 2.10: Block diagram of microwave water sensor.

2.6 Sensor Deployment Scheme

There are many techniques of sensor deployment for the earth based system. In case of fully controlled deployment, the wireless sensors are manually deployed at the desired site. In fully controlled system, the sensor may have rechargeable battery and the battery of the node can also be replaced or removed. The network topology is well defined in such cases before actual operation of the network and this method is found expensive as compared to other schemes. In partly controlled system, the sensors are dropped by a moving vehicle in a specific way at the desired site. The sensors are battery powered and the network topology is not well defined in such cases, but broadly it is known before actual operation of the network. The topology is dynamic and the method is cheaper as compared to the manual deployment.

In case of random deployment, the sensors are dropped by some means (e.g. balloon) at a random point in the desired site and may occupy random positions after reaching the target area. The network topology is not defined in such cases before the actual operation of the network and it is dynamic. The method is cheaper as compared to manual deployment and partly controlled deployment, in general. Issues related to any sensor deployment system on the earth are:

- well defined dropping points
- minimum number of sensors
- maximum coverage of probing region by the sensors
- wireless connectivity among the sensors
- sensor trajectory parameters

Issues related to sensor deployment scheme for the moon include all of these, along with deployment vehicular movement.

Various deployment techniques have been reported in the literature like random deployment or a planned grid deployment given by Leoncini et al. [111, 112] and Chakrabarty et al. [113]. These techniques are for terrestrial applications on the earth, adopting grid strategy with square cells for environmental monitoring in areas, which are not easily accessible or reachable. Figure 2.11 shows grid strategy with square cells for sensor deployment.

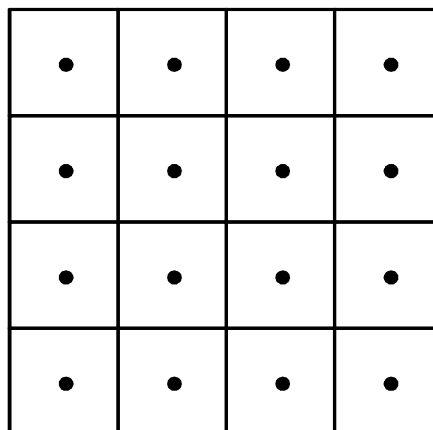


Figure 2.11: Grid deployment with square cells having dropping points at the centre.

Implementing grid strategy with cells of any shape and deploying sensors by a satellite above each cell in the grid, is impractical approach for the lunar application. In other terrestrial scheme, sensors are deployed through airplane moving above the regions and the uncertainty involved is addressed by Zou and Chakrabarty [114]. Figure 2.12 shows deployment of sensors from an aircraft in a typical deployment system.



Figure 2.12: Sensors dropped from an aircraft in a typical system (Photo Courtesy: http://www.army-technology.com/contractor_images/vaisala/4-meteorological-sensor.jpg).

For applications on the earth, the aircraft can fly horizontally and square regions can be covered. For the targeted lunar application, the deployment of sensors by means of many sensor packets, thrown from the orbiter, cannot be done economically in horizontal direction; due to limitation of size and weight in space missions. Howard et al. [115, 116] use self-deployment scheme and potential field based sensor deployment scheme, which are difficult to be implemented on the moon. Kumar et al. [117] show barrier coverage with sensors and also use random deployment. Zou and Chakrabarty [118] use random deployment initially and apply algorithm to maximize sensor field coverage. Chen et al. [119] give survey on sensor deployment algorithms. Wang et al. [120] discuss the movement assisted sensor deployment. Wang et al. [121] give a virtual rhomb grid-based movement-assisted sensor deployment algorithm, which integrates both deterministic and self-organizing deployment in a unified framework. Wan and Yi [122] discuss the sensor deployment as Poisson or uniform point

process in square or disk region. Bai et al. [123] suggest optimal deployment pattern. Balister and Kumar [124] compare a random versus deterministic deployment of sensors in presence of failure and placement error.

For lunar or planetary application, the random deployment like that given by Maleki [125] and Clouqueur et al. [126] is to be adhered to, by throwing sensors in some way in the sensing zone of interest. Figure 2.13 depicts the conceptual view of sensors dropped from the orbiter on lunar surface.

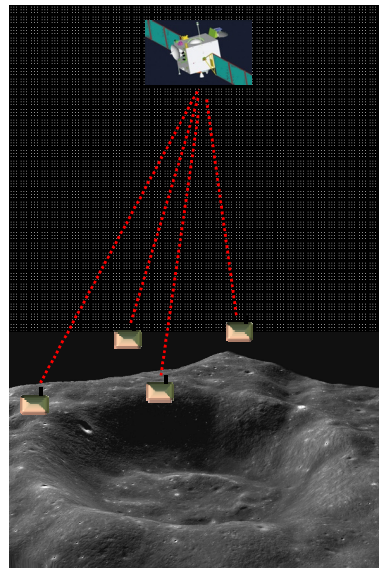


Figure 2.13: Concept of sensor deployment on lunar surface from satellite (Crater Photo Courtesy: http://www.isro.org/chandrayaan/htmls/Imagemoon_tmc.htm).

2.7 Summary

This chapter describes the present wireless scenario, existing wireless models and various types of fading arising in the wireless channel in the initial part. It also presents the lunar environment, regolith properties, lunar soil simulant and existing water sensors along with conceptual designs of optical and microwave sensors. The chapter reviews the sensor deployment schemes for the earth based wireless systems.

The chapter constitutes a bridge between the two diversified areas, viz., the wireless technology and the lunar surface science. The application of WSN for lunar and planetary surface sciences is a new concept and requires knowledge of many fields, together. All aspects needed for this purpose are visited and a synopsis of all is presented at a single place, in this chapter.

Chapter 3

Lunar Wireless Model and RF Coverage Prediction

A wireless sensor network essentially uses the simple low cost sensors that are distributed in a given region. WSN provides excellent spatial resolution and wide geographical coverage. Due to their small sizes, the nodes in a WSN have a limited amount of resources and therefore, power optimization is needed. A lunar WSN has been proposed to study the regolith properties and to infer the presence of water ice by in-situ measurement. The radio propagation environment in any WSN presents limitations to the performance of the system. The signal between the transmitter and the receiver is subjected to various physical phenomena. The propagation path loss and different types of fadings are main causes of signal variations. The communication scenario on the lunar surface is different as compared to that on the earth. Due to different environment on the moon, it provides some design constrictions for lunar system as compared to the terrestrial system on the earth, as given below.

System Design Constraints

- Atmosphere: There is no atmosphere on the moon, which restricts the use of any existing wireless model of the earth based system, in general.

- **Unattended Ground Sensor Structure and Poor Conductivity:** Due to unattended structure and very poor conductivity [71] of lunar surface, there is a possibility of inclusion of direct path at the receiver. Also, the chances of diffraction in all paths reduce.
- **Wavelength:** Due to the restricted size of payload in any space mission, it is preferable to use the higher operating frequency. This causes more number of reflectors and generates many multipath components, as the size of objects become possibly larger than wavelength.
- **Scattering:** Because of smaller wavelength and larger surface undulations, the probability of scattering losses increases.

All such constraints pose serious limitations in using the existing wireless propagation models and therefore a new model, which considers local environment for the system design, has been proposed for the moon in this chapter.

3.1 Lunar Wireless Path Loss Model

The sensors deployed on the lunar surface by adopting any scheme or as suggested in Chapter 6, settle on the surface and may be awakened due to self timer provided in the hardware. Triggering, if required, may be achieved by ground based tele-command system through an orbiter. These sensors can collect information about the physical phenomena of interest and transfer the data to the rover, as and when ready, through wireless communication. The signal transmitted in the channel has to pass through the lunar surface conditions and environment. However, the lunar environment is quite different than that of the earth, as mentioned in Subsection 2.3.1, in Chapter 2.

System design constraints indicate that the existing propagation models cannot directly be applied for communication on the moon. The model should include the effects of local environment of the moon. The selected frequency band is 2.4 GHz due to small size of antenna and easy availability of the transceivers, which may later be space qualified.

3.1.1 Suitability of Existing Models

Fundamentally all the existing propagation models have been developed for wireless systems on the earth and in general, none of them is directly suitable for the wireless sensor network on the moon due to the nature of the network and local constraints. Some of the models have been described in Chapter 2 and the suitability of each is discussed below.

A. Irregular Terrain Model

The ITM [41, 42] takes terrain and other parameters as inputs and produces the output as signal distribution in a given area. There are certain limitations of ITM, that it can be used for minimum antenna height of 0.5 metre and minimum communication distance of 1 km. As the wireless sensor network involves deployment of sensors on the ground with very small antenna heights, especially at 2.4 GHz operating frequency, the ITM cannot be used for such applications.

B. Two-Ray Model

The two ray model is mostly used for direct and ground reflected rays. In case of lunar wireless sensor network, the sensor nodes are to be on the surface with very small antenna heights. Therefore, two ray model may not give complete idea of the signal strength at the receiver. Instead, a large number of multipath components reflected from nearby terrain is expected at the receiver.

C. Visual System Simulator Multipath Model

The multipath channel model in AWR VSS [46] is for systems on the earth and it is based on model like ITM. This model is generally used for moving nodes, which is not the case for lunar wireless sensor network. Also, it is more useful for earth based systems, where path gains are available based on practical measurements.

D. Willis Multipath Model

Willis [12] has given the extended version of two ray model as multipath model and suggested to calculate a possible direct path separately. However, this model avoids scattering losses, possibly due to low frequency of operation. However, at 2.4 GHz operating frequency, scattering losses become more pronounced as compared to those occurring at 800 or 400 MHz frequency range. This model does not include direct path along with multipath in the vector sum. The direct path should be considered for lunar WSN due to reasons given in Chapter 4. Due to ease of rover operation, the lunar WSN has to be in the regions where possibility of diffraction is reduced to a great extent. Moreover, this model is basically suggested for the earth based system as mentioned earlier, which incorporates higher antenna heights and considers atmospheric losses. Hence, it cannot directly be applied for the WSN on lunar surface.

Similarly there are other models for wireless systems on the earth. For example, Durkin's model [127, 128] does not consider multipath effect in the simulation. Walfisch and Bertoni [129] gave a model to consider the impact of rooftop and building height by using diffraction to predict the average signal strength at street level. Chukkala et al. [80] and Daga et al. [79] gave the modeling and simulation of Radio Frequency (RF) environment of mars, which are based on ITM. Models like ITM for the earth may be used for the mars, as the mars has thin atmosphere but they cannot be used for the moon, since the moon has no atmosphere.

3.1.2 Physical Phenomena in Wave Propagation

Since, the earth based model cannot directly be used for lunar applications; various physical phenomena occurring during wave propagation have been examined considering the wave propagation environment on lunar surface. The signal transmitted by a transmitter is affected by such phenomena in the communication channel. The phenomena and factors associated with them are given below, and have been combined to arrive at a lunar wireless path loss model given in Subsection 3.1.3.

A. Free Space Loss

The proposal is to use compact wireless impedance sensors (along with other types of sensors), having quarter wave antenna of size 3.125 cm at 2.4 GHz operating frequency, for detection of electrical properties of lunar regolith. The idea is to use Line-Of-Sight (LOS) propagation technique for small distances of up to few hundred metres. Under ideal communication conditions, the power radiated from antenna is omni directional in the plane of interest, which is horizontal here and power is inverse square function of the distance for free space wave propagation, as given below by Friis formula [130].

$$P_r = \frac{P_t G_t G_r \lambda^2}{16 \pi^2 d^2} \quad (3.1)$$

where P_t and P_r are the transmitter and receiver powers, respectively; G_t and G_r are the gains of transmitter and receiver antennas, respectively; λ is the wavelength of operation and d is the distance from the transmitter. Free space loss is a basic loss for communication on the lunar surface, since there is a high vacuum [1, 2] on the moon. There is no atmosphere on the moon and therefore, there are no atmospheric losses, which are present on the earth.

B. Reflection

Wireless communications on the earth is affected by factors like steady and moving reflectors and scatterers, atmospheric absorption, etc. and lead to attenuated multipath components at the receiver. The signal is also affected by the Doppler effect. However, in case of lunar application, there are no moving objects or reflectors on the surface and also, the nodes are steady. The rover generally carries the cluster head and it moves very slowly with a speed of the order of a few mm per second. Hence, there can be multipath signals at the receiver due to surface topography and the Doppler effect is not really significant. For a rover speed of 10 mm/s typically, there is a maximum Doppler shift of 0.08 Hz at 2.4 GHz operating frequency. Multipath components travel on different propagation paths and arrive at different times at the receiver, causing the ISI at the receiver. Thus, the main possibility of the signal getting affected is due to the multipath fading caused by surface reflections due to

uneven terrain structure. This leads to multipath propagation in the wireless channel. The signal arriving at the receiver by the direct path will be modified due to multipath components. The expected number of multipath components is decided by signal BandWidth (BW) and maximum delay spread, as discussed in Chapter 4. The wavelength of transmitted signal is 12.5 cm at 2.4 GHz wireless operation and objects should be of larger size to cause the reflection. Rocks of size larger than 12.5 cm are easily found on the lunar surface along with fine grained regolith. That is why reflections from nearby terrain are expected in large number, creating increased possibility of multipath at the receiver. Parsons [131] derived the received signal strength using reflection coefficient (Γ) at the reflector as given below.

$$P_r = \frac{P_t G_t G_r \lambda^2}{16 \pi^2 d^2} \cdot |1 + \Gamma \exp(j \Delta)|^2 \quad (3.2)$$

where

$$\Gamma = \frac{a \sin \psi - \sqrt{(\epsilon_r - j x) - \cos^2 \psi}}{a \sin \psi + \sqrt{(\epsilon_r - j x) - \cos^2 \psi}} \quad (3.3)$$

is the reflection coefficient and

Δ = phase shift created due to reflected signal

ψ = angle of incidence with vertical from transmitter antenna to the reflector

ϵ_r = relative dielectric constant of the ground

a = 1 or $(\epsilon_r - j x)$ for horizontal or vertical polarization, respectively

where x is defined as $x = \frac{\sigma}{2 \pi f \epsilon_0}$

with σ = conductivity of the ground

f = frequency of operation

ϵ_0 = free space permittivity

Reflections are expected from uneven terrain. In fact, the major component of channel fading on the moon is due to the multipath created by reflections from craters and surface irregularities. Also, the transceiver used for ground sensors should not use horizontal

polarization; otherwise the signal would be attenuated [132] very near the transmitter. Instead, vertical polarization should be used, which can provide sufficient signal at farther distances.

C. Reflection Scattering

When the signal is reflected from lunar surface, it is likely that the ray is scattered due to dispersed signal. Gibson [133] has suggested the specular reflection and stated that roughness of a surface can be classified by Rayleigh criterion as given below.

$$h_c = \frac{\lambda}{8 \cos \theta_i} \quad (3.4)$$

where θ_i is angle of incidence at the reflector. Gibson [133] gave a parameter h , which represents minimum to maximum deviation about mean terrain height. If $h > h_c$, then the terrain is considered as a rough terrain and the loss for the same is considered by multiplying reflection coefficient by a scattering loss factor ρ_s calculated by Bothias' equation as below.

$$\rho_s = \exp \left[-8 \left(\frac{\pi \sigma_h \cos \theta_i}{\lambda} \right)^2 \right] \cdot I_0 \left[8 \left(\frac{\pi \sigma_h \cos \theta_i}{\lambda} \right)^2 \right] \quad (3.5)$$

where σ_h is the standard deviation of surface height about the mean surface height and I_0 is the modified Bessel function of the first kind and zero order. On the lunar surface, the regions are mostly rough and may have varying sized objects, which can lead to scattering losses. If $h < h_c$, the surface is considered to be smooth and the scattering loss is absent.

D. Diffraction

For line-of-sight communication, if an obstacle of the size comparable to wavelength of the transmitted signal is present in between the transmitter and the receiver, then the diffraction loss or gain can occur at the edge of an obstacle. The signal may be scattered and attenuated before reaching the receiver. On the lunar surface, it is likely to have such obstacles between the transmitter and the receiver. Knife-edge diffraction gain or loss may be

considered as shown by Lee [134], depending on a given terrain. Various methods are suggested [135-137] for multiple obstructions. Diffraction from the knife-edge obstacle can cause the signal to bend. Wong [43] stated that the bending of signal due to knife-edge obstacle causes higher signal strength as compared to that due to the rounded one. Since, the direct component contributes much higher signal power at the receiver, it is necessary to consider diffraction factor for the LOS component. For multipath components, the signal power would already be very less, as compared to that of the LOS signal and the diffraction factor may be neglected. For detailed study, one can consider the diffraction factors for all the paths, depending on the terrain. Most favorable practical scenario is to deploy the sensors in a lunar site with the least surface undulations to minimize the diffraction problem and to make the surface navigation easier by the rover.

3.1.3 Proposed Lunar Wireless Model

Considering the diffraction for direct path and including the reflections as well as scattering at various reflectors; the following equation [138] is given for obtaining area coverage in a wireless sensor network on the lunar surface.

$$\begin{aligned}
 P_r = & \frac{P_t G_t G_r \lambda^2}{16 \pi^2} \\
 & \cdot \left| L_{dd} \frac{1}{d_d} \exp(-j k d_d) + \rho_{s1} \Gamma_1(\psi_1) \frac{1}{d_1} \exp(-j k d_1) \right. \\
 & \left. + \rho_{s2} \Gamma_2(\psi_2) \frac{1}{d_2} \exp(-j k d_2) + \dots + \rho_{sn} \Gamma_n(\psi_n) \frac{1}{d_n} \exp(-j k d_n) \right|^2
 \end{aligned} \tag{3.6}$$

where L_{dd} is the diffraction factor of direct or LOS signal, d_d is the distance travelled by LOS signal, k is the phase constant, ρ_{sn} is the reflection scattering factor of n^{th} multipath component, Γ_n is the reflection coefficient of n^{th} multipath component, ψ_n is the angle of

incidence at n^{th} reflector and d_n is the distance travelled by n^{th} multipath component. The proposed model is called Lunar Wireless Model (LWM).

3.2 Modeling Parameters

All parameters used in the modeling are summarized in Table 3.1. The sensors can communicate with the rover or neighbor node to complete the network, once a wireless sensor network is deployed on the lunar surface. It is not feasible to test the system performance on the moon before the actual deployment. To visualize a practical scenario on the moon, a transmitter location is fixed at one point in a given landing site and 0 dBm power is transmitted at 2.4 GHz frequency, with a quarter wave monopole antenna. A similar antenna is kept at the receiver, and the receiver is moved to various locations to measure the received signal strength. As discussed in 3.1.2-B, vertical polarization is preferred in the simulation.

Table 3.1: Modeling parameters for RF coverage prediction

| Parameter for Model | Value |
|---|-----------------------|
| Moon Radius | 1737.4 km |
| Transmitter Power | 0 dBm |
| Transmitter Antenna | Quarter Wave Monopole |
| Receiver Antenna | Quarter Wave Monopole |
| Frequency of Operation | 2.4 GHz |
| Lunar Regolith Dielectric Constant [70] | 4 |
| Lunar Regolith Conductivity [71] | 10^{-8} S/m |
| Wave Polarization | Vertical |
| Transmitter Location | Middle Left |

Dielectric constant of lunar regolith is taken as 4, which is shown by Buehler et al. [70]. Similarly, the conductivity of lunar regolith is taken as 10^{-8} S/m, which is given by Chung et al. [71] for Apollo 14 lunar samples. Though, these values of the parameters have been taken for the example runs, they can be varied in the simulation, if required. The moon

radius is used to correct for a small error due to curvature of the moon, while calculating distances on the lunar surface.

3.3 Digital Elevation Model of Selected Lunar Site

Digital Elevation Model (DEM) of a landing site is also needed along with the other parameters in the LWM to include the terrain effect. Terrain Mapping Camera (TMC) on board Chandrayaan-1, a recent Indian mission to the moon, has provided high-quality DEM data during the mission time. Four sample sites at various locations have been selected; considering almost plane surface, region with some peaks and region with few craters; to study the lunar radio propagation model. Table 3.2 shows the details of sites used in deriving communication area coverage. The antenna height may be added to a DEM for computation.

Table 3.2: Selected lunar sites for RF coverage prediction

| Site No. | Crater Near the Site | Lunar Latitude | Lunar Longitude | Area of Region (square km) |
|----------|----------------------|---------------------------|---------------------------|----------------------------|
| 1 | Catalan | -52.103 to -52.40781 | 279.807 to 280.55313 | 9.2 (lat) × 22.4 (lon) |
| 2 | Baade | -45.414 to -45.71881 | 279.764 to 280.51013 | 9.2 (lat) × 22.4 (lon) |
| 3 | Zsigmondy | 60.548 to 60.101722 | 248.720 to 249.779051 | 13.4 (lat) × 31.8 (lon) |
| 4 | Moretus | -70.5916 to -71.708189 | 358.4305 to 360.645171 | 33.6 (lat) × 66.6 (lon) |

The DEM data of various sites were obtained during different satellite orbits and the resolutions were different. Sites 1 and 2 have resolution of 56.1 m in both directions; site 3 has resolution of 122.67 m in horizontal (longitude) direction and 53.34 m in vertical (latitude) direction, while site 4 has 185.07 m in both directions. Figure 3.1 (a) to Figure 3.1 (d) [138] show the DEM images of all these four sites, respectively; taken by the TMC on

board Chandrayaan-1. Using the available DEM of the lunar sites, three dimensional images have been generated, as depicted in Figure 3.2 (a) to Figure 3.2 (d).

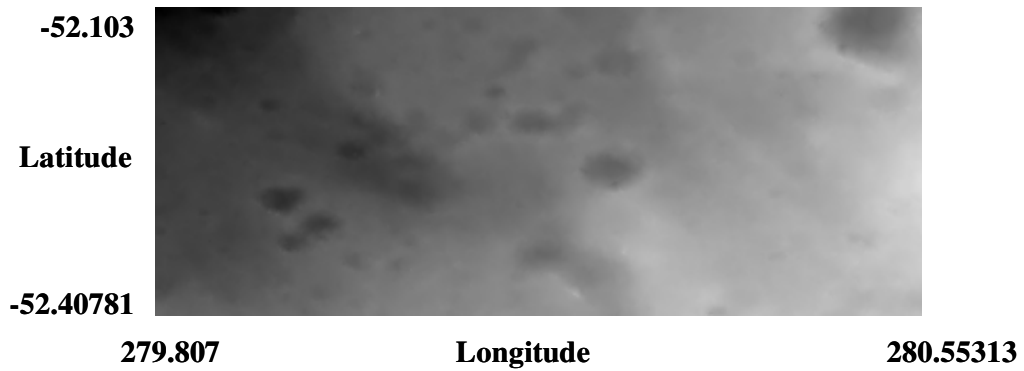


Figure 3.1 (a): DEM of lunar site 1.

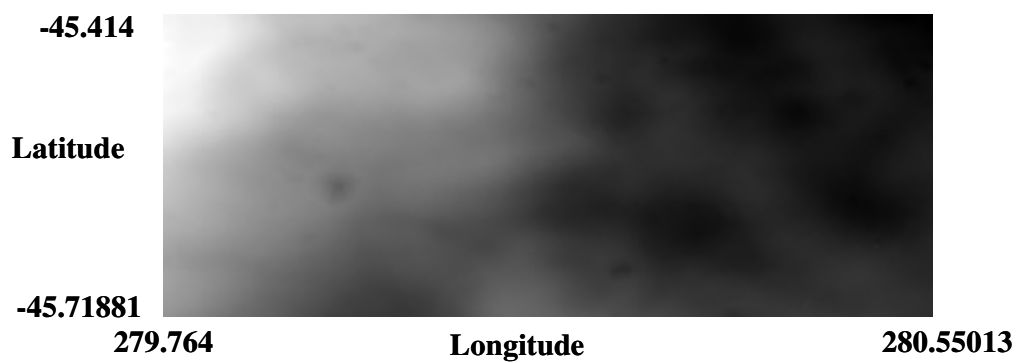


Figure 3.1 (b): DEM of lunar site 2.

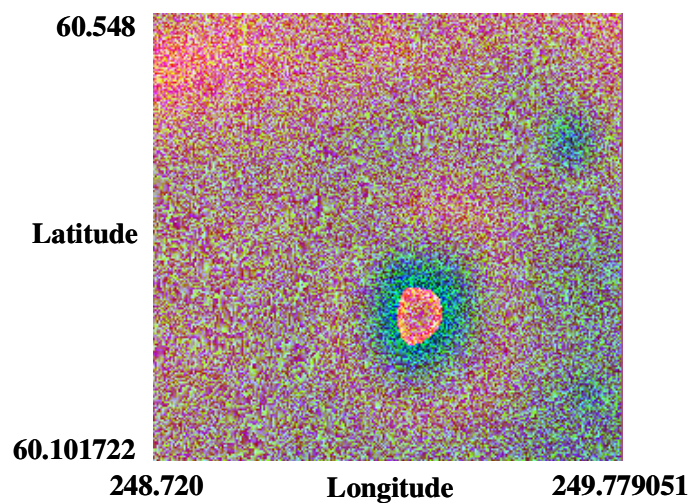


Figure 3.1 (c): DEM of lunar site 3.

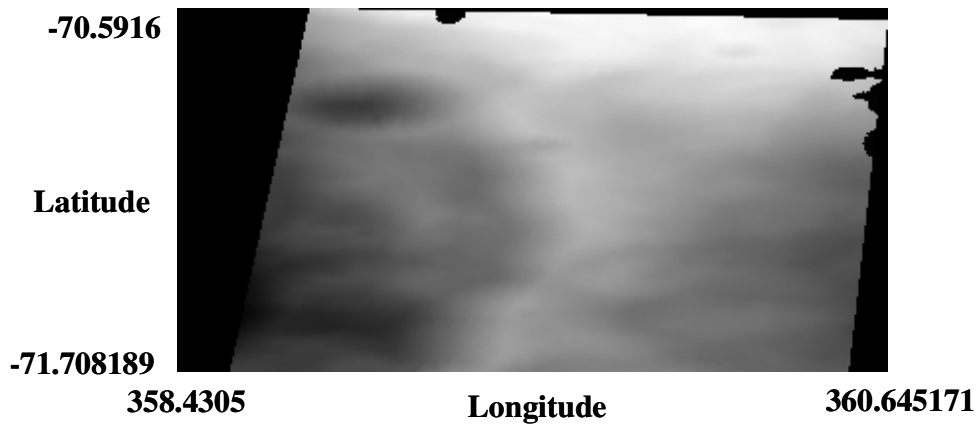


Figure 3.1 (d): DEM of lunar site 4.

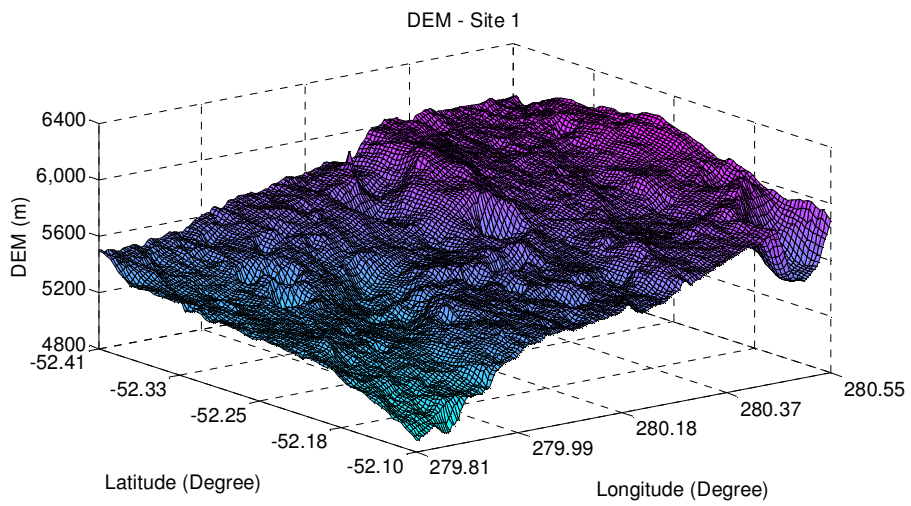


Figure 3.2 (a): 3-D DEM of lunar site 1.

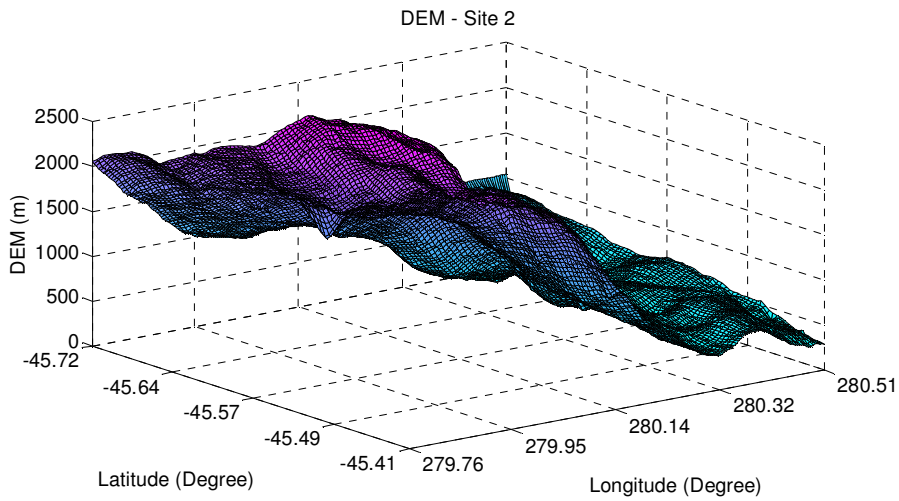


Figure 3.2 (b): 3-D DEM of lunar site 2.

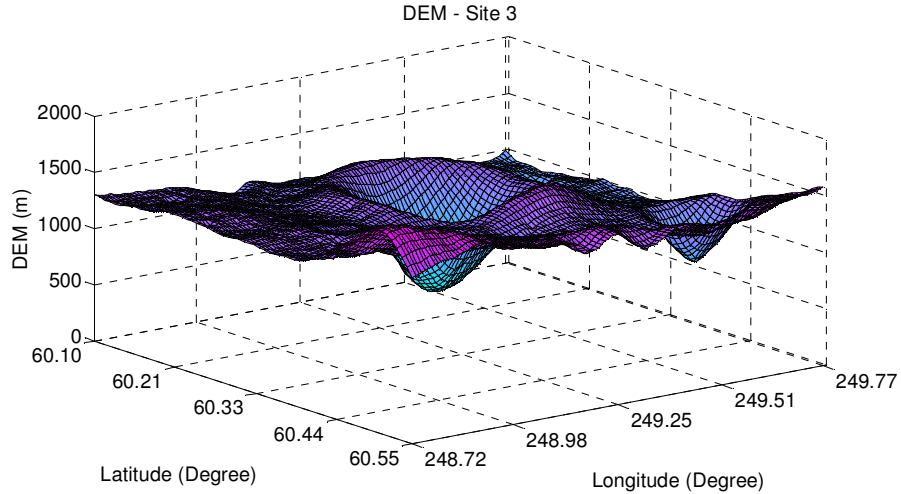


Figure 3.2 (c): 3-D DEM of lunar site 3.

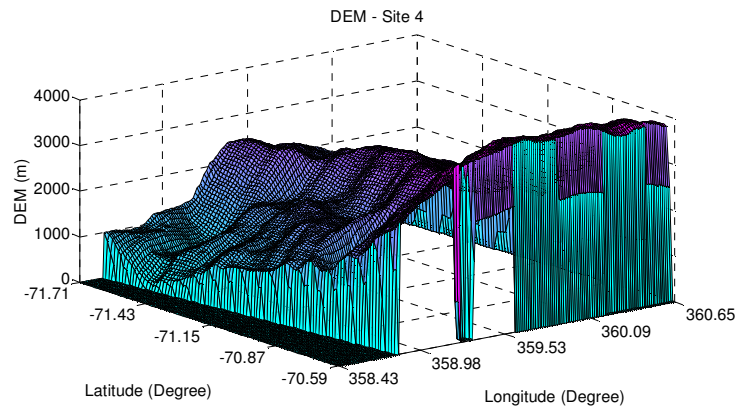


Figure 3.2 (d): 3-D DEM of lunar site 4.

3.4 Justification in Support of LWM

Ideally, any wireless model should be supported by practical measurements to validate it for practical applications. Since, it is not feasible to carry out measurements related to wireless model on the moon, it is imperative to check its applicability for practical situations by means of qualitative and logical arguments. Following are justifications in support of the proposed lunar wireless model:

- ❖ Due to absence of atmosphere, there are no atmospheric losses during the wave propagation.
- ❖ Due to very high vacuum of the order of 10^{-12} Torr [1, 2] on the moon, the free space loss is a basic loss.
- ❖ Due to Unattended Ground Sensor (UGS) type structure of lunar WSN and very poor conductivity of lunar regolith, typically 10^{-8} S/m for Apollo 14 samples as given in [71], there is a possibility of line-of-sight signal carrying major component of the total received strength at the receiver.
- ❖ If an obstacle is expected for the direct path based on DEM of a given landing site, the diffraction factor should be included.
- ❖ Reflections can occur from nearby terrain due to small (typically 12.5 cm) signal wavelength, causing the multipath at the receiver.
- ❖ At the reflectors or scatterers, there can be reflection losses as well as scattering losses due to wavy surface.
- ❖ The signal power of multipath would be less as compared to that of the line-of-sight path due to longer travel time of waves and the diffraction factor for the multipath may be neglected. The most favorable practical scenario is to deploy the sensors in a lunar site with the least surface undulations to minimize the diffraction problem and to make the surface navigation easier by the rover. In such cases, the possibility of occurrence of diffraction is rare and the effect would be too small to be considered. For detailed analysis, one can include diffraction factors for all paths.
- ❖ The number of multipath components is decided by the signal bandwidth and the maximum delay spread of the multipath.
- ❖ The total received signal is a vector or phasor sum of all the components.

3.5 Results and Discussions

Based on the proposed lunar wireless model, the RF area coverage patterns have been derived for four lunar sites. Modeling parameters as well as DEM data of the lunar sites measured by TMC on board Chandrayaan-1 have been taken as inputs in the RF modeling.

MATLAB [139] code has been written to ease the computing work and the results are derived for the selected lunar sites. These results [138] are depicted in Figure 3.3 to Figure 3.6 for lunar sites 1, 2, 3 and 4; respectively.

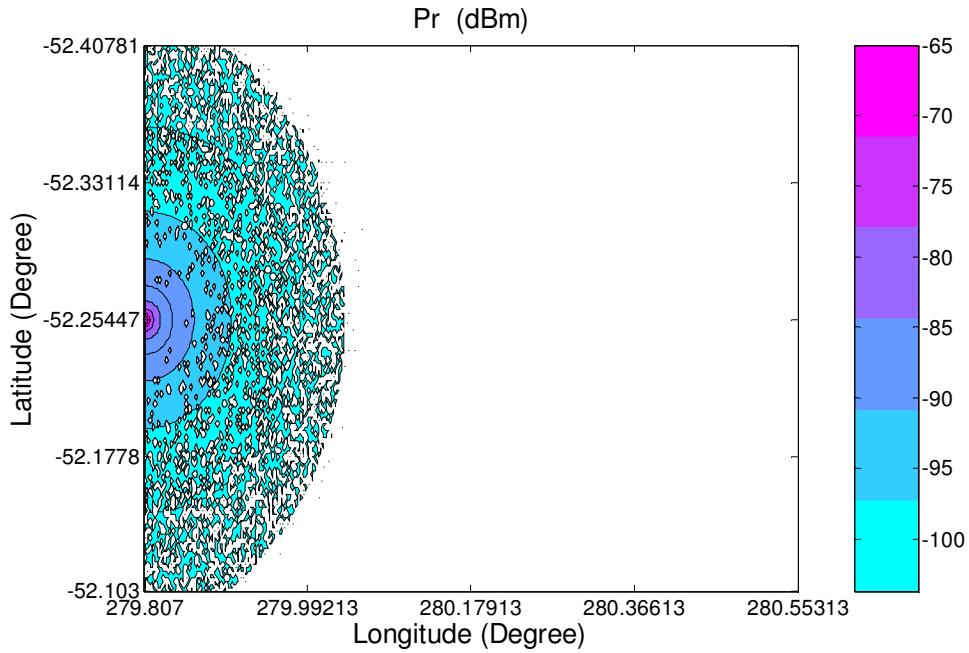


Figure 3.3: Area coverage pattern of lunar site 1.

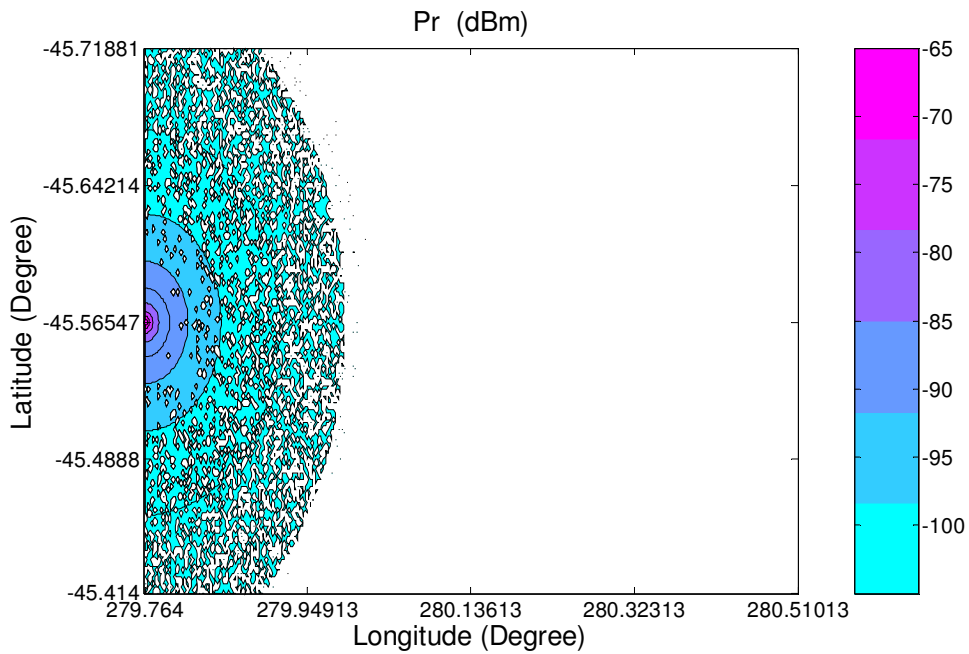


Figure 3.4: Area coverage pattern of lunar site 2.

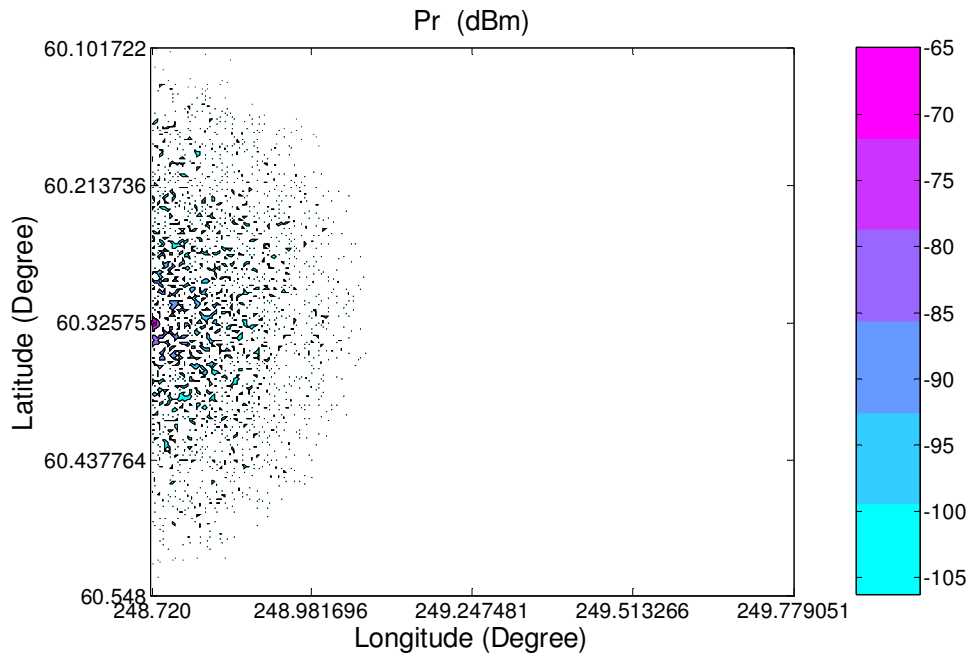


Figure 3.5: Area coverage pattern of lunar site 3.

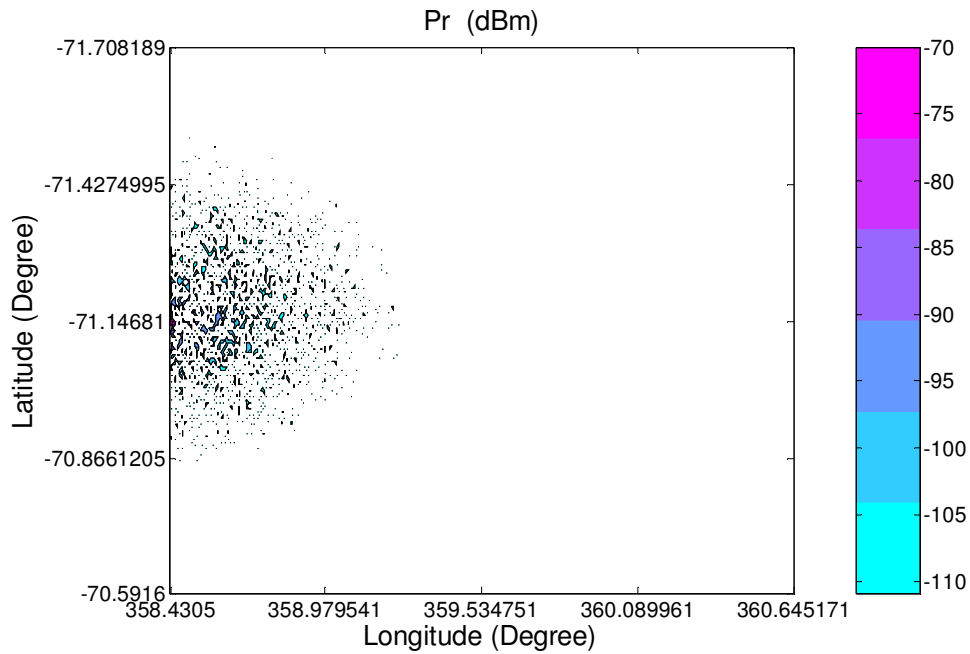


Figure 3.6: Area coverage pattern of lunar site 4.

The lunar wireless model considers all possible phenomena occurring during the wave propagation on the moon and it includes the losses associated with them, for a wireless sensor network on lunar surface. Major interest is in establishing a direct line-of-sight

communication between the transmitter and the receiver for lunar wireless sensor network. For a given area, there can be many multipath components depending on the size of the objects in the region and if all are allowed to contribute in the code, then the computational complexity is increased highly, due to the involvement of higher order matrix. Moreover, it needs highly sophisticated computing facility and it takes very long time for computation. The number of multipath components may, therefore, be restricted to smaller numbers, which is reasonably justified, as the distance travelled by the signal along the multipath is quite large in most of the regions as compared to that of the direct path. Hence, the contribution of those multipath components would be very less as compared to the contribution from the direct path. The number of multipath occurring during the propagation is discussed in Chapter 4.

The results in Figure 3.3 to Figure 3.6 show the received power in dBm, at various locations as per color bar. The white portions in the results are places, where the signal does not reach. Normally, the sensor node, operating in 2.4 GHz ISM band, has 0 dBm output power and its receiver has sensitivity of about -100 dBm [140]. The useful area is where the received power is more than -100 dBm. Radio coverage of the sites have been calculated as a ratio of occupied region, having more than -100 dBm received signal power to the total region under consideration. Table 3.3 shows the percentage radio coverages of all sites for 250 kbps link, effectively showing useful area for sensor network deployment. The bit rate of 250 kbps is included in the IEEE 802.15.4 standard at 2.4 GHz frequency. One can use different bit rate, if desired, in a given application.

Table 3.3: Lunar site coverage

| Site | Site Coverage (250 kbps link) |
|------|----------------------------------|
| 1 | 11.27 % |
| 2 | 10.02 % |
| 3 | 2.73 % |
| 4 | 1.01 % |

Sites 1 and 2 have been selected with comparatively plane surface having lesser undulations on the surface, while sites 3 and 4 have different profiles. The site 4 is at the edge

of Moretus crater near lunar south pole. From the derived radio coverage at the selected lunar site, one can know the areas having more than some specific value of received power. Results indicate the percentage coverage of a given site with known topography and also the possibility of checking, if a given sensor node would be useful, as far as the sensitivity of the receiver is concerned. The sensor nodes should preferably be deployed in the region, where the sufficient amount of power is available (pink in the coverage patterns). In case of lunar wireless sensor network, the rover is supposed to carry a cluster head and the radio coverage pattern can suggest the possible paths for the rover to move, assuring intact communication link with the nodes.

3.6 Conclusion

The existing RF models for the earth cannot directly be applied to a lunar WSN. This chapter has proposed a new wireless propagation model, called the Lunar Wireless Model, for a lunar WSN. The free space loss is a basic loss on the moon and some reflections along with scattering can occur from terrain irregularities, causing the multipath at the receiver. The RF modeling results show the percentage coverage patterns for a given bit rate of the link on lunar surface, based on DEM data. The RF modeling results suggest (a) possible use of available transceivers, as far as receiver sensitivity is concerned, (b) better sensor deployment sites on the moon, based on terrain data or; area coverage pattern for a given landing site on the moon and (c) rover paths to assure the wireless connectivity between the node and the cluster head on the rover.

Chapter 4

Lunar Multipath Environment and Wireless Link Analysis

A wireless sensor network consisting of appropriate sensors to measure the lunar regolith properties is proposed. The network is established, whenever the wireless sensors are deployed and the network is completed by a link with the base station, which can be a steady lander or a navigating rover on the lunar surface. As discussed in Chapter 3, wireless communication is affected by the local environment of the moon and the link performance suffers due to multipath signals at the receiver. The transmitted signal undergoes through several physical phenomena in the channel, which distort the original signal and introduce the ambiguity at the receiver. Consequently, signal detection at the receiver can result in the bit errors.

During transmission of the information signal, any error probability affects the system throughput. The bit errors also influence the system delay, which plays a vital role in real time traffic, if any. Due to error at one position, the whole packet has to be retransmitted, resulting in the wastage of power and bandwidth. Thus, the prediction of link performance beforehand is mandatory, especially in the space missions. The decision criteria are different for the lunar WSN, as compared to that on the earth.

System Design Constraints

- No Salinity: No salinity has been known on the moon [141] and so, there are no electrolytes in the lunar regolith for conduction.
- Poor Conductivity: Due to very poor conductivity [71] of the lunar surface, there is a possibility of the inclusion of a direct path at the receiver.
- Ice mixed with regolith: Even though water ice is present at some places on the lunar surface, its conductivity would be poor, since it would only be a pure ice. Thus, the signal can propagate within the obstacle between the transmitter and receiver, presenting a strong LOS at the receiver.

All such constraints place restriction for using the Rayleigh channel model, which is normally taken for wireless systems on the earth. A new channel model has to be adopted for the moon, which considers effects of the local environment in the design.

As shown by Chukkala and Leon [47], the two main communication issues with respect to channel evaluation are the link budget obtainable by propagation path loss or received power at a given location for a given transmitted power, and the time dispersion of the transmitted bits due to multipath propagation. Multiple replicas of the transmitted bit arrive at different times, after travelling through different paths and undergoing different path delays due to multipath effect. The time dispersion can be described by a Power Delay Profile. The time dispersive nature of the multipath channel plays an important role in deciding the maximum data rate that may be transmitted and the associated statistical parameters, i.e., the average and rms path delays may be obtained. The Power Delay Profile (PDP), Bit Error Rate (BER) and Packet Error Rate (PER) are good performance parameters for evaluation of any wireless communication link.

For a point to point wireless link analysis on lunar surface, one has to select the positions of the transmitter and the receiver on a given region and then find out the PDP, BER and PER of this link. The results can be quite useful, for predicting the behavior of the

wireless sensor nodes. For a wireless sensor network on lunar surface, once the sensors are deployed using some deployment scheme [142] after deciding an appropriate deployment site, the sensor nodes remain steady and only a rover moves on the lunar surface carrying a cluster head. There can basically be two types of communication scenarios (1) between a sensor node and the rover and (2) between any two deployed sensor nodes. The pictorial view of a typical arrangement of the wireless sensors on lunar surface is shown in Figure 4.1.

2.5D Visualisation (Coulomb C Crater)

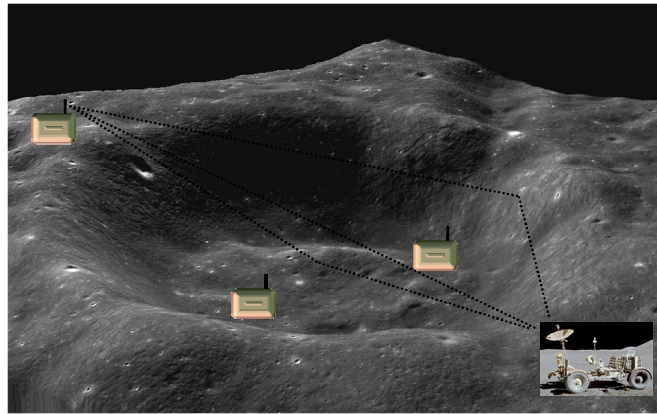


Figure 4.1: Pictorial view of wireless sensors on lunar surface (Crater photo courtesy: http://www.isro.org/chandrayaan/htmls/ImageMoon_tmc.htm).

To check the effect of small-scale fading on the data rates, the multipath signal components of the channel have to be derived based on terrain data. The path delay of the direct component is taken as a reference and all remaining signal components are considered with respect to the direct component for calculating the excess path delays. However, a PDP may also be studied using the absolute path delays of multipath signals reaching the receiver, which is at a certain position from the given transmitter. The time dispersion property of the multipath is generally described by the mean delay and rms delay; as shown by Rappaport et al. [143]. These properties are described in Chapter 2.

For the first communication scenario given above, there can be multipath between the transmitter and the receiver, along with a possible line-of-sight path. Also, the rover may be assumed to be moving with some velocity v , which can give rise to the Doppler shift in frequency spectrum at the receiver. Such movement in the rover can lead to fading of the

received signal at the receiver, though slow, due to predefined and expected very low speed of the rover, of the order of few mm per second. In other words, the received signal amplitude can vary with respect to time. Such random nature of the received amplitude can be treated as random variable and its probability density function (pdf) is given by Rician pdf [144]. This is because; the Rician pdf includes the possibility of direct path as well as multipath between the transmitter and receiver. Thus, for the first type of link on the moon, there will be multipath fading at the receiver, causing Inter Symbol Interference (ISI) and also there exists a possibility of very small fading due to the Doppler effect. The latter may be neglected for all practical applications on the moon, due to very low speed of the rover.

For the second case, the nodes are stationary and there can again be multipath between the transmitter and receiver, along with direct line-of-sight signal. These can cause interference at the receiver, as various multipath signals arrive at the receiver after some propagation delay. Since, the nodes are steady, there will not be any time fading, but there will be many signals coming with some specific delay at the receiver, causing the ISI. Such phenomena are repeated for various bits of information signal. If there are a large number of multipath signals at the receiver, then according to the Central Limit Theorem, the amplitude of the received signal will have the Gaussian pdf [145]. Thus, for the second case, there is no time fading at the receiver, but the signal distribution may be considered as Gaussian distribution for calculation of error rate. For practical application, the sensor nodes are expected to communicate only with slowly moving rover, due to limited recourses in space, essentially making single hop communication. More importantly, the performance parameters for the second case are expected to be better than those for the first case; as the Doppler shift would occur in the first case, while the Doppler shift would be absent for steady nodes in the second case. Moreover, the Rician pdf becomes the Gaussian pdf for larger value of Rician k factors. Hence, the first case provides the worst case scenario and only that needs to be examined in detail. Durgin [146] has provided theoretical steps for finding the BER of a fading channel. By making suitable choices and going through the steps suggested in [146], the equation of BER with differential binary phase shift keying modulation is given by

$$BER = \int_0^{\infty} \frac{1}{2} \exp\left(-\frac{\rho^2}{P_N}\right) \cdot \left(\frac{\rho}{\sigma^2}\right) \cdot \exp\left[-\frac{(\rho^2 + a^2)}{2\sigma^2}\right] \cdot I_0\left(\frac{\rho \cdot a}{\sigma^2}\right) d\rho \quad (4.1)$$

where ρ is a variable representing the received signal amplitude, σ^2 is the variance of received signal amplitude, P_N is the constant noise in the system, I_0 is the modified Bessel function of first kind and zero order [147] given by

$$I_0(z) = \sum_{k=0}^{\infty} \frac{(\frac{1}{4}z^2)^k}{(k!)^2} \quad (4.2)$$

and value of a depends on the strength of the direct path between the transmitter and receiver. When a is zero, the dominant signal is absent and the Rician distribution becomes a Rayleigh distribution. The Rician function is usually expressed in terms of the carrier-to-multipath ratio or k factor [12] given by

$$k = \frac{c}{m} = \frac{a^2}{2\sigma^2} \quad (4.3)$$

where c and m are the strengths of the carrier and multipath components, respectively. When k is zero (the direct component is absent or multipath components are dominant), the pdf becomes a Rayleigh distribution; and as k increases, the pdf shifts to the right, indicating an increase in the strength of the received signal. For larger values of k , the pdf becomes a Gaussian distribution.

The lunar wireless model is presented in Equation (3.6). The application of the lunar wireless model is extended further for analysis of lunar multipath environment and point-to-point wireless link. The power received at any node is given by [138]

$$P_r = \frac{P_t G_t G_r \lambda^2}{16 \pi^2} \cdot \left| L_{da} \frac{1}{d_d} \exp(-j k d_d) + \rho_{s1} \Gamma_1(\psi_1) \frac{1}{d_1} \exp(-j k d_1) + \rho_{s2} \Gamma_2(\psi_2) \frac{1}{d_2} \exp(-j k d_2) + \dots + \rho_{sn} \Gamma_n(\psi_n) \frac{1}{d_n} \exp(-j k d_n) \right|^2 \quad (4.4)$$

4.1 Number of Multipath

For any communication system under fading environment, the number of multipath components plays very important role, as the signal received at the receiver is a phasor sum of the signals received by direct path as well as by multipath. Theoretically, there can be a large number of multipath signals in a mountainous terrain, specifically at the operating frequency of 2.4 GHz due to its very small wavelength. It may be possible to measure the received power for a given transmitter power and derive the multipath parameters [148] in a terrestrial wireless network on the earth. However, for the lunar wireless network, such measurement is not possible. It has been attempted to predict the number of multipath theoretically, for a fading channel, based on the sampling theorem.

Extensive simulation study based on the DEM data shows the nature of the PDP as exponentially decaying. Due to presence of LOS signal, there is finite amount of power present at the beginning of exponential profile. The profile is truncated at the maximum delay spread, thus allowing multipath power up to a certain threshold. One such profile is shown in Figure 4.2 (a). This PDP is used to obtain the number of multipath in the lunar WSN. However, the number of multipath derived below does not depend on a particular shape of PDP and it is applicable to any shape of PDP, in principle. Similar PDPs are given for outdoor model on the earth [149, 150].

Suppose, a PDP for a given wireless system is as shown in Figure 4.2 (a), which is exponentially decaying. It provides the delay parameters like average delay $\bar{\tau}$, rms delay spread σ_{τ} and maximum delay spread τ_{max} . If such a PDP is considered as a signal in the time domain, its Fourier transform conveys its spectra in the frequency domain, as shown in Figure 4.2 (b); and its bandwidth can easily be found. Suppose the bandwidth of the signal is B Hz and its time period is T , then based on the Nyquist criteria [151], its sampling frequency f_s is given by

$$f_s \geq 2 B \quad (4.5)$$

The sampling instants are given as $T_s = 1/f_s$. Thus, for a duration of T sec, there will be $n = T/T_s$ number of samples, which are needed for reconstructing the signal in the time domain, preserving its bandwidth. Hence,

$$n \geq 2 B T \quad (4.6)$$

Thus, the minimum number of sampling points is $n = 2 B T$, rounded to the next higher integer. Analogous to a signal in the time domain, the Fourier transform of a PDP can provide information about the coherence bandwidth B_c [152]. For the signal to be transmitted in the multipath environment having flat fading, it is necessary that the signal bandwidth is less than the coherence bandwidth. There is also a possibility of line-of-sight signal component for the lunar wireless sensor network [138]. Adding it to the number and taking $\tau = \tau_{max}$, the minimum number of multipath components is given as

$$n_{m \min} = \text{ceil}[2 \tau_{max} B] + 1 \quad (4.7)$$

where *ceil* is a ceiling function of MATLAB [139], which rounds up the number to the next higher integer. Equation (4.7) can be used for any type of PDP profile to find out the number of multipath. Patzold et al. [149] have shown similar equation for the number of multipath, to be used in the tapped delay line structure of multipath channel. If there are more multipath signals present, they add to the profile, but $n_{m \min}$ can provide sufficient information about

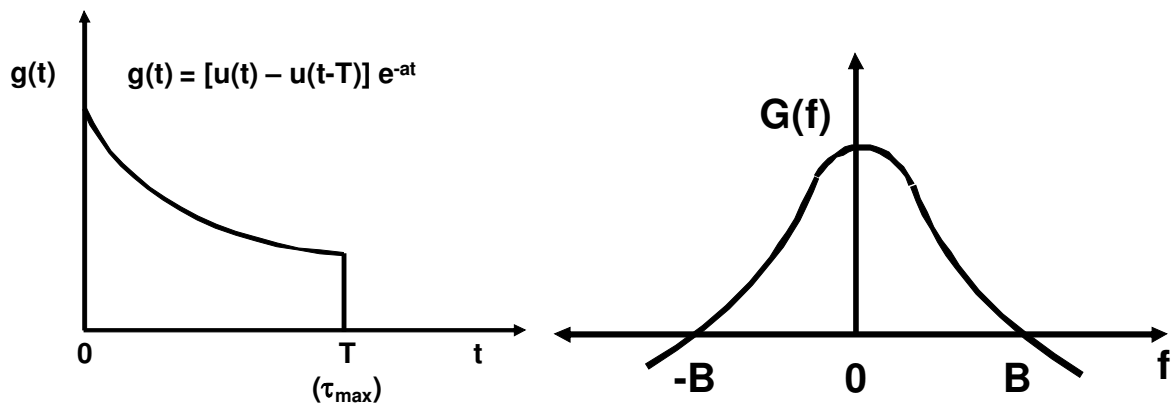


Figure 4.2: (a) Exponentially decaying nature of lunar PDP and (b) Fourier transform of PDP.

the nature of the profile by preserving its bandwidth. This minimum number of multipath is taken in the analysis.

4.2 Region under Consideration

A recent mission to the moon from India, Chandrayaan-1, had Terrain Mapping Camera (TMC) on board for deriving the DEM and has provided good-quality data during the mission time. One of the lunar sites is near Zsigmondy crater towards the lunar north pole. This site has been selected due to presence of almost plane surface and few craters (regions with undulations) within it. The selection of site helps to study the multipath effects due to crater, and predict the communication behavior of the wireless sensor network. A three dimensional DEM of the selected site is shown in Figure 4.3, which has a resolution of 61.34 m in longitude (horizontal) direction and 53.34 m in latitude (vertical) direction, after interpolation in longitude direction to make the grid finer. Due to heavy computational load involved in finding multipath parameters for a given site, small regions around the location of transmitter are taken. The first region is $R1$ and the second region is $R2$, as depicted in Figure 4.3. Various parameters like Rician k factors of all possible links in a given region with fixed transmitter and mobile receiver, multipath delays associated with all the links and multipath gains are computed. The DEM data shown in Figure 4.3 are used along with other inputs in the lunar wireless model, given by Equation (4.4), to derive various multipath parameters.

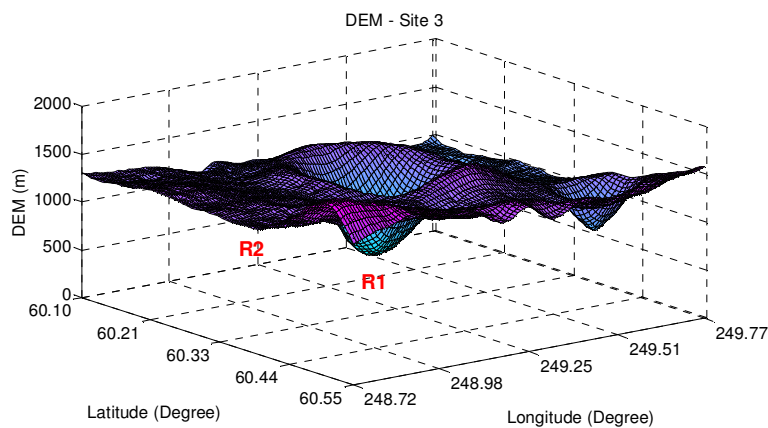


Figure 4.3: 3-D DEM of lunar site 3.

The multipath channel on the moon is represented by a block diagram shown in Figure 4.4, where SG is a signal generator producing bit patterns, Tx is a transmitter, AWGN is Additive White Gaussian Noise and Rx is a receiver. The AWGN presents background noise on the moon, created mainly due to sunlight and cosmic radiation. A particular bit pattern is transmitted by using a predefined modulation scheme and it is affected by multipath fading on the way along with addition of some background noise. The bit pattern arrives at the receiver after undergoing various path delays and path gains. The pattern creates the ISI at the receiver, which are then analyzed to know errors in the transmission. Since the wavelength of operation is small (12.5 cm), there can be many multipath components present on the moon. Also, large phase changes may be encountered in multipath propagation on the moon. Therefore, it is suggestive to use a differential modulation scheme to avoid the effect of phase changes during the propagation. So, the differential Binary Phase Shift Keying (BPSK) has been selected in the work.

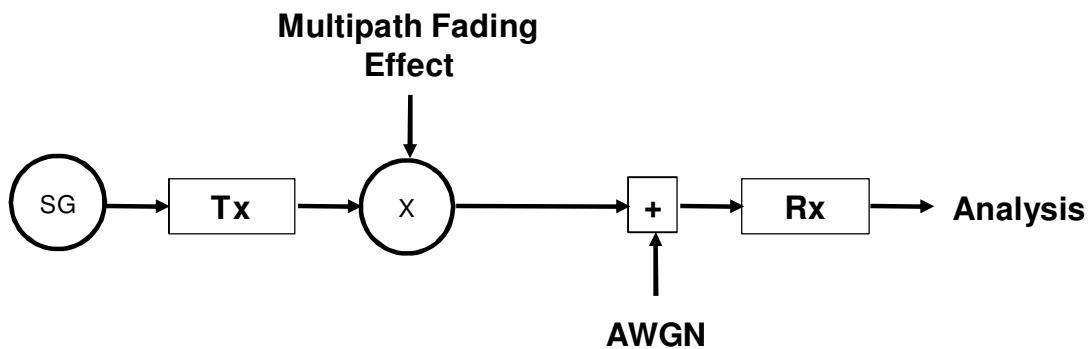


Figure 4.4: Block diagram of lunar multipath channel.

4.3 Selection of Channel Object

Since there has been very little work done on wireless systems for space and planetary applications, only a few references are available in this direction. Magness [153] from European Space Agency (ESA) has provided the assessment of short range RF wireless technology for space applications. Leon et al. [83] from NASA has discussed about the

wireless technology for planetary environment. Chukkala and Leon [47] showed the analysis of multipath on the mars, Borah et al. [81] have shown the BER and PER of a link on the martian surface, while Daga et al. [79] have shown the terrain based simulation to give error rates for martian surface. Tank and Linnartz [154] have given the statistics of Rician multipath in mobile communication. Lindsey [155] has shown the error probability for Rician multichannel reception and Willis [12] has mentioned about the Rician pdf for LOS and multipath for the earth based system.

There is no suggestion of channel object for the moon in the literature, as the moon is least explored for the wireless systems. It is very much clear from the lunar wireless model suggested in Chapter 3, that there is a possibility of multipath signals at the receiver for the system under consideration. There is also a possibility of LOS or direct component present at the receiver. Therefore, the Rician channel object is suggested for the wireless sensor network on the moon.

Qualitative Arguments in Support of Rician Channel Object

- ❖ No salinity has been known on the moon [141] and so, there are no electrolytes in the lunar regolith for conduction.
- ❖ The value of the depth of penetration gives an idea of direct component, which may reach the receiver, on the other side of an obstacle. If the direct component reaches the receiver, it can give rise to the Rician distribution.
- ❖ If there is an obstacle between the transmitter and the receiver; signal can reach the shadow region with negligible attenuation constant due to very dry lunar surface, possessing very poor conductivity [71]. This includes LOS at the receiver along with multipath components.
 - Typically, for lunar regolith $\rho = 10^8 \Omega\text{-m}$ from Apollo 14 data [71],

$$\omega = 2 \cdot \pi \cdot (2.4 \times 10^9) = 15.08 \times 10^9 \text{ rad/s,}$$

$$\mu = \mu_0 = 4 \cdot \pi \cdot 10^{-7} \text{ H/m and}$$
 - Depth of penetration [156] is $\delta = \sqrt{\frac{2\rho}{\omega\mu}} = 102.73 \text{ m}$

- ❖ Even though water ice is present at some places on the lunar surface, its conductivity would be poor (of the order of 10^{-5} S/m); since it would only be a pure ice. Thus, the signal can propagate within the obstacle between the transmitter and receiver, presenting a strong LOS at the receiver.
 - For highly pure water, $\rho = 1.82 \times 10^5 \Omega\text{-m}$ [157] and $\delta = 4.38$ m
 - For pure ice, ρ is of the order of 10^5 to $10^8 \Omega\text{-m}$ [158] and δ is in the range from 3.25 m to 102.73 m.
- ❖ The values of depth of penetration represent enough possibility of direct signal component, reaching the receiver and creating the Rician channel object.

Due to all these reasons, the selected channel object for the moon is the Rician. Also, when $k = 0$, it gives the Rayleigh object in the absence of direct path.

4.4 Results and Discussions

The DEM data of the moon were given by TMC on board Chandrayaan-1, a recent Indian mission to the moon. The lunar DEM data have been used to calculate the angle of incidence, the reflection coefficient, the distance etc by the method shown in Chapter 3 for achieving the link performance parameters like the PDP. MATLAB [139] codes have been written for various analyses. The lunar wireless model given in Chapter 3 has been used to derive the Rician k factors (a ratio of the line-of-sight power to the multipath power), the multipath delays and the multipath gains.

Suppose Γ is a reflection coefficient at the reflector on lunar surface, R_{dm} is a ratio of direct path to one of the multipath components, B is the signal bandwidth and τ_{max} is the maximum delay spread; then, based on lunar wireless model in Equation (3.6) or Equation (4.4), the equation of maximum delay spread (τ_{max}) is given by

$$\tau_{max} = \frac{d_{LOS} [\Gamma \cdot 10^{R_{dm}/20} - 1]}{c} \quad (4.8)$$

and the equation of number of multipath (n_m), which is suggested by Patzold et al. [149] and also shown in Section 4.1 based on the Nyquist criteria, is given by

$$n_m = \text{ceil}[2 \tau_{max} B] + 1 \quad (4.9)$$

where d_{LOS} is the line-of-sight distance, c is the velocity of light and ceil is a MATLAB [139] function, which rounds the number up to the nearest higher integer. Due to large margin involved inherently in Equation (4.9), the effects of scattering at the reflector and diffraction in LOS, if any, are smoothed. In addition, simplifying the scattering gives specular reflection at the reflector. For a fixed link and given signal bandwidth, the number of permissible multipath is optimized based on the values of Γ and R_{dm} , as seen from Equation (4.8) and Equation (4.9).

To know the performance parameters of a typical point-to-point wireless link, an example link has been chosen arbitrarily, in which the location of the transmitter with 0 dBm power is kept at the middle left position in a rectangular region and the location of the receiver is at about 500 m towards the right of the transmitter; in the selected portion of lunar site. Table 4.1 shows details of the number of multipath, where quantities used are defined as

- P_{LOS} = Line-of-sight power for 500 m link
- P_m = Multipath power less than P_{LOS} by few dB
- d_e = Excess distance to be travelled by the multipath for 500 m LOS distance
- n_m = Number of multipath for 500 kHz signal bandwidth or number of taps in tapped delay line structure

The calculation of delay in Table 4.1 is based on Equation (4.8) and it is actually the excess delay as compared to LOS signal. Negative delay indicates that the multipath reaches earlier than LOS signal. However, the multipath is supposed to travel excess distance as compared to LOS signal and has to be delayed as compared to LOS signal. Hence, cases with negative value should be considered as those, with only LOS signal for a given amount of dB value, down to LOS signal.

A small region of lunar surface is selected with a size of about 1226.8 m in longitude (horizontal) direction and 1066.8 m in latitude (vertical) direction, having a small crater inside. For the selected site, the average value of the reflection coefficients was found to be about 0.32 based on the DEM data. For multipath power 15 dB down the LOS power and reflection coefficient of 0.32, the number of multipath comes out to be three. Locations of the

Table 4.1: Multipath number calculation

| Sr. No. | P_{LOS} (dB) | Down (dB) | P_m (dB) | d_e^1 (m) | τ_{max}^1 (μ s) | n_m^1 | d_e^2 (m) | τ_{max}^2 (μ s) | n_m^2 |
|---------|----------------|-----------|------------|-------------|---------------------------|---------|-------------|---------------------------|---------|
| 1 | -83.71 | 10 | -93.71 | 1081.1 | 3.604 | 5 | 5.96 | 0.02 | 2 |
| 2 | -83.71 | 12.5 | -96.21 | 1608.5 | 5.362 | 7 | 174.71 | 0.582 | 2 |
| 3 | -83.71 | 15 | -98.71 | 2311.7 | 7.706 | 9 | 399.75 | 1.332 | 3 |
| 4 | -83.71 | 17.5 | -101.21 | 3249.5 | 10.832 | 12 | 699.83 | 2.333 | 4 |
| 5 | -83.71 | 20 | -103.71 | 4500 | 15 | 16 | 1100 | 3.667 | 5 |

1: Results for unity reflection coefficient

2: Results for reflection coefficient of 0.32, which is for almost all lunar regions into consideration, calculated based on terrain.

reflectors are generated randomly and the results are shown in Figure 4.5 (a) to Figure 4.5 (f). PDP of a typical point-to-point link is shown in Figure 4.5 (a); while line curve in Figure 4.5 (b) shows BER of the link as a function of SNR, when 50000 bits were transmitted at 500 kbps bit rate. The asterisk (*) curve in Figure 4.5 (b) is for Rayleigh type channel, when there is no line-of-sight component present. Similarly, link performance parameters for all possible links in a given region are derived by moving the receiver and keeping the transmitter fixed. Figure 4.5 (c) shows Rician k factors of all possible links in region 1 (crater) and Figure 4.5 (d) shows BER of all possible links in region 1, over Rician channel, with 50000 bits transmitted at the bit rate of 500 kbps. Figure 4.5 (e) shows BER of all possible links in region 1, over Rayleigh channel, with 50000 bits transmitted at the bit rate of 500 kbps. Figure 4.5 (f) depicts PER of the link under consideration as a function of SNR, in which 100 trials of 10000 bits were transmitted at the rate of 500 kbps. Similar results of region 2 in site 3 are shown in Figure 4.6 (a) to Figure 4.6 (f). The region 2 is outside the crater in lunar site 3.

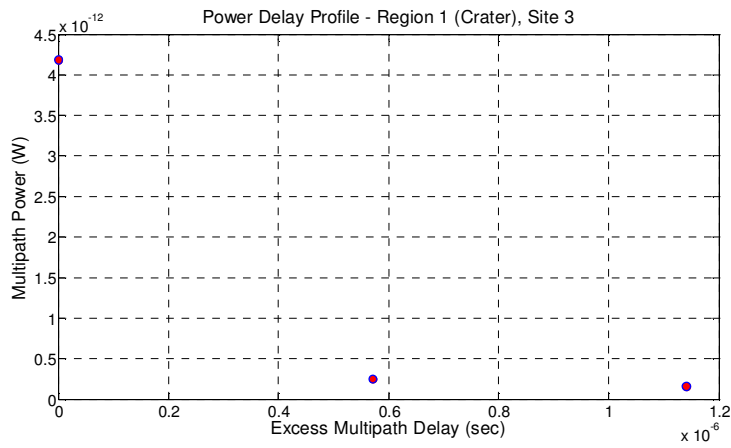


Figure 4.5: (a) PDP of a typical link in region 1 (crater) of site 3.

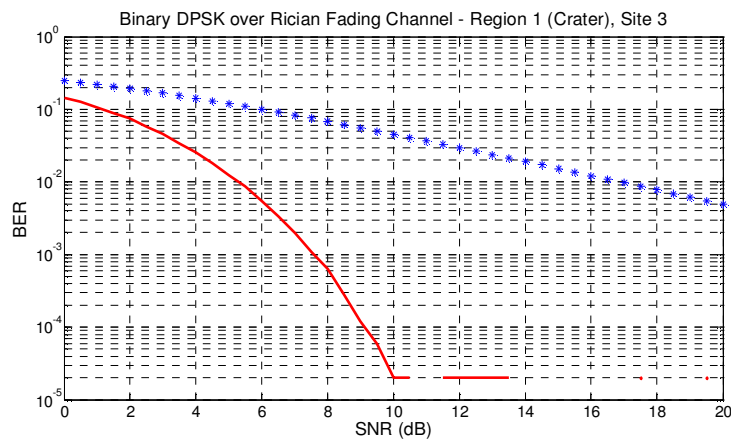


Figure 4.5: (b) BER of a typical link in region 1 (crater) of site 3.

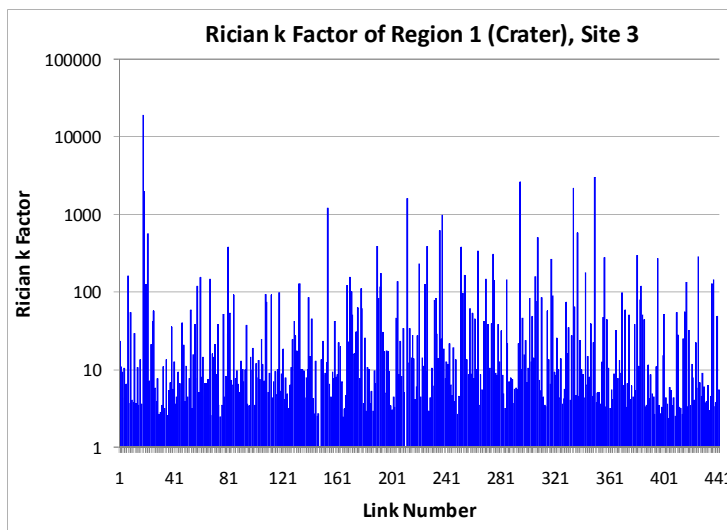


Figure 4.5: (c) Rician k factors of all links in region 1 (crater) of site 3.

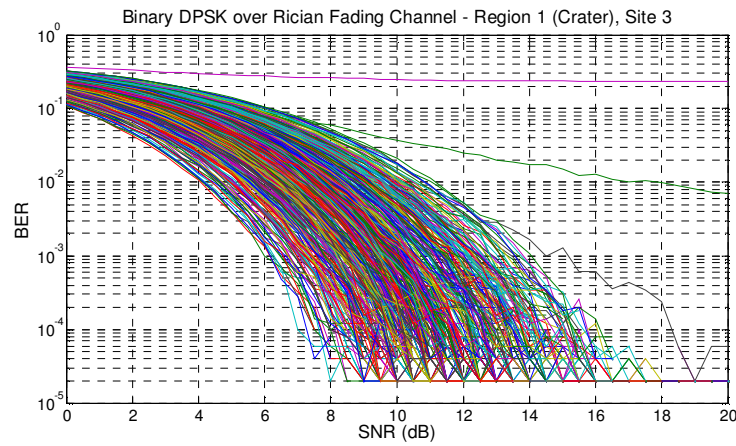


Figure 4.5: (d) BER of all possible links in region 1 (crater) of site 3, over Rician channel.

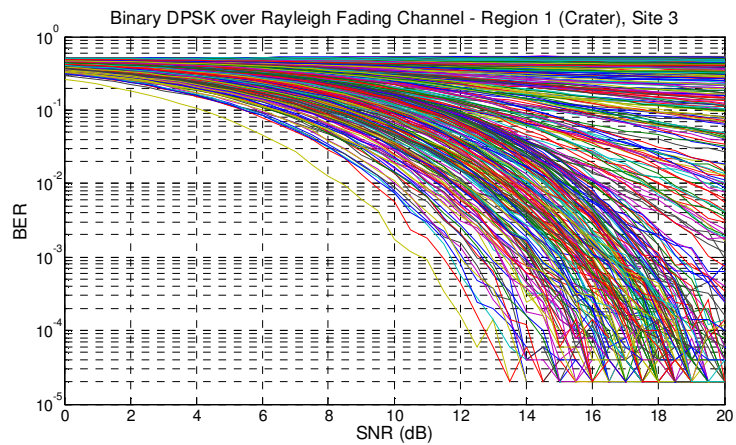


Figure 4.5: (e) BER of all possible links in region 1 (crater) of site 3, over Rayleigh channel.

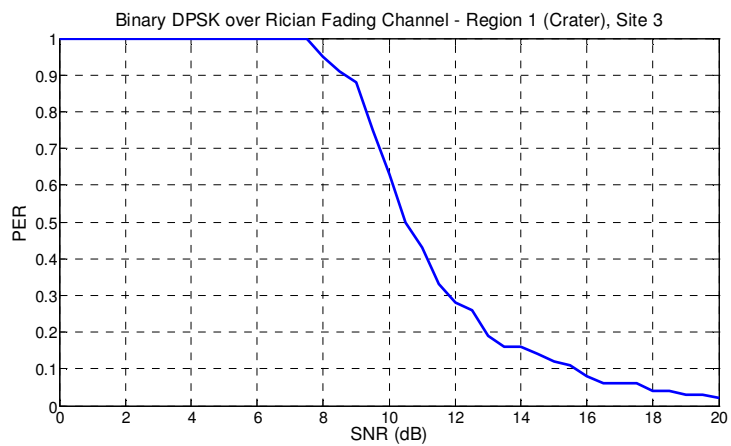


Figure 4.5: (f) PER of a typical link in region 1 (crater) of site 3.

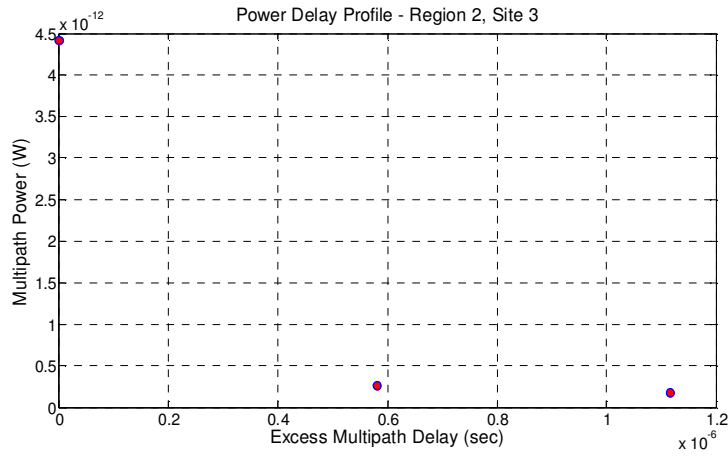


Figure 4.6: (a) PDP of a typical link in region 2 of site 3.

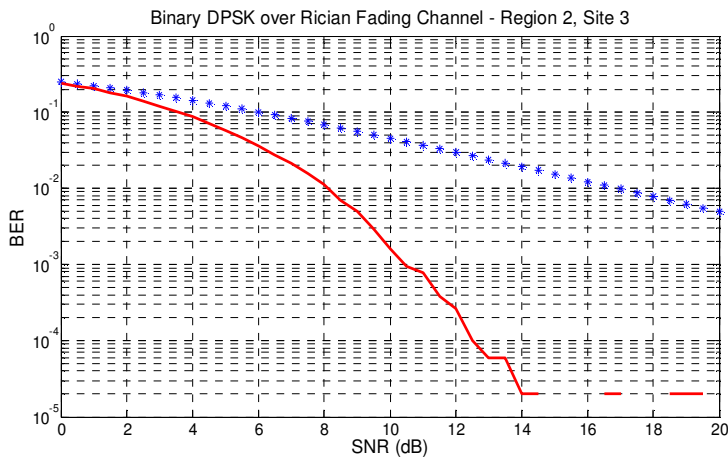


Figure 4.6: (b) BER of a typical link in region 2 of site 3.

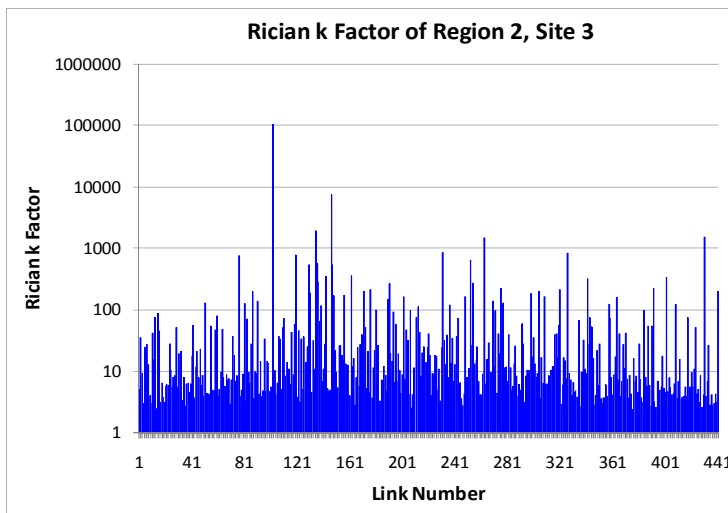


Figure 4.6: (c) Rician k factors of all links in region 2 of site 3.

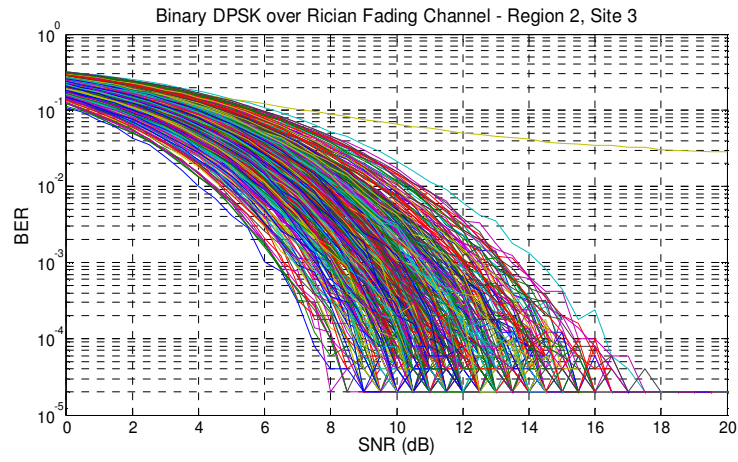


Figure 4.6: (d) BER of all possible links in region 2 of site 3, over Rician channel.

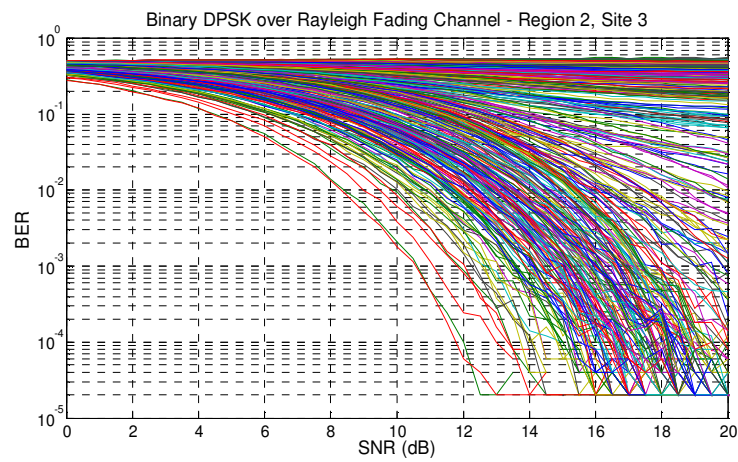


Figure 4.6: (e) BER of all possible links in region 2 of site 3, over Rayleigh channel.

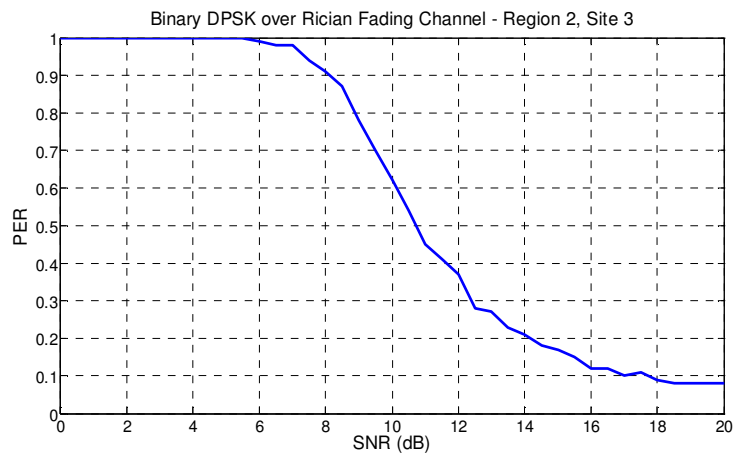


Figure 4.6: (f) PER of a typical link in region 2 of site 3.

The comparison of performance over the Rician and Rayleigh channels in region 1 can be made using Figure 4.5 (d) and Figure 4.5 (e). Similarly, the comparison of performance over the Rician and Rayleigh channels in region 2 can be made using Figure 4.6 (d) and Figure 4.6 (e). It is seen from Figure 4.5 (d), Figure 4.5 (e), Figure 4.6 (d) and Figure 4.6 (e) that the BER of the Rician channel is better than that of the Rayleigh channel, in general, due to significant power carried by the line-of-sight component as compared to multipath components. It is given by Chuang [49], that, for several modulation types such as BPSK, QPSK, OQPSK and MSK; the average irreducible BERs have been shown to become larger than 10^{-3} , when rms delay spread exceeds 10 % of the symbol period and equalization is not used. Therefore, as a general rule, the maximum data rate with acceptable BER performance is limited to $0.1/\sigma_\tau$ for frequency nonselective channel, when using a receiver which does not employ an equalizer to combat the effects of multipath fading.

PDP results show exponential decaying function for lunar surface, like outdoor models on the earth as given by Patzold et al. [149] and by Erceg et al. [150]. From this profile, mean and rms delay spreads are found, which are shown in Table 4.2. The coherence bandwidth shown in Table 4.2 is actually based on an approximate relationship, as given in Chapter 2. Considering these approximate values, it is seen that the channel becomes frequency selective for both the example cases, as the signal bandwidth is higher than the coherence bandwidth. However, the exact relationship between coherence bandwidth and rms delay spread is a function of applied signal and specific channel response, as described in Chapter 2. In Table 4.2, S_{max} is the maximum bit rate without equalizer and S_s is the simulation bit rate.

For a given landing site on the moon, one has to use DEM of the site and apply the method shown, to check if the channel becomes frequency flat or frequency selective, for a given signal bandwidth. In case of frequency nonselective channel, one can find out the maximum data rate, without the use of an equalizer. If the channel is found to be frequency selective, then one may have to reduce the signal bandwidth. The BER results show that the errors reach as high as 10^{-3} for many links having SNR less than 12 dB, which is also verified from the rms delay spread value as compared to the symbol period. Hence, the minimum suggested SNR at the receiver is about 15 dB, keeping a margin of 3 dB. Higher BERs are expected due to the ISI, caused by path delays.

Table 4.2: Multipath parameters, bit rates and packet loss

| Region No. | $\bar{\tau}$ (μs) | σ_{τ} (μs) | App. $B_{c50\%}$ (kHz) | S_{max} (kbps) | S_s (kbps) | Packet Loss (at 12 dB SNR) (%) |
|------------|--------------------------------|-----------------------------------|------------------------|------------------|--------------|--------------------------------|
| 1 | 0.571 | 0.466 | 429.18 | 214.59 | 500 | 28.75 |
| 2 | 0.566 | 0.456 | 438.60 | 219.30 | 500 | 37.50 |

Though, region 1 has crater within the surface, actual BER depends on Rician k factor. For a typical link under consideration, the value of Rician k factor in first region is 386.48; while that in the second region is 17.72; which indicates that higher line-of-sight power is present in region 1 as compared to that in region 2. DEM in Figure 4.3 shows that region $R1$ is inside the crater and region $R2$ is outside the crater. This DEM has 252 positions in latitude direction, while 520 positions in longitude direction. The regions under considerations ($R1$ and $R2$) are 21 positions in latitude and 21 positions in longitude directions. The transmitter location in region $R1$ is at 168th latitude and 300th longitude, while that in region $R2$ is at 80th latitude and 168th longitude; as shown in Figures 4.7 (a) and 4.8 (a), respectively. The close up view of 3-D DEM of region $R1$ near the transmitter is shown in Figure 4.7 (b) and that of region $R2$ is shown in Figure 4.8 (b). The receiver location is at about 500 m, towards the right of the transmitter location, in both the cases. It is evident from Figure 4.7 (b) and Figure 4.8 (b) that there exists better possibility of line-of-sight signal (due to concave surface) in region 1 as compared to that in region 2 (due to wavy surface). Higher the Rician k factor, higher is the power in line-of-sight as compared to diffuse power, and there is an improvement in BER (better BER for the same SNR), as expected. This is also verified from Figure 4.5 (b) and Figure 4.6 (b). Also, the packet loss at 12 dB SNR is about 8.75 % more in region 2, as compared to that in region 1. Thus, the results indicate that the link in region 1 gives better performance and hence, it is better for sensor deployment.

For detailed analysis, one may include the possibility of diffraction and scattering too, in the method shown. For more precise applications of the given wireless link, one may apply the method for a large number of times and take the average value of the parameter. The analysis of lunar multipath environment can be carried out using the LWM. Link performance

parameters of any link are achievable by the suggested method, based on DEM of the landing site. The prediction of the maximum data rate without the use of an equalizer is useful to the hardware designer. Exclusion of an equalizer simplifies the receiver design and consequently, reduces the mass and the size of a payload, which are at premium in any space application.

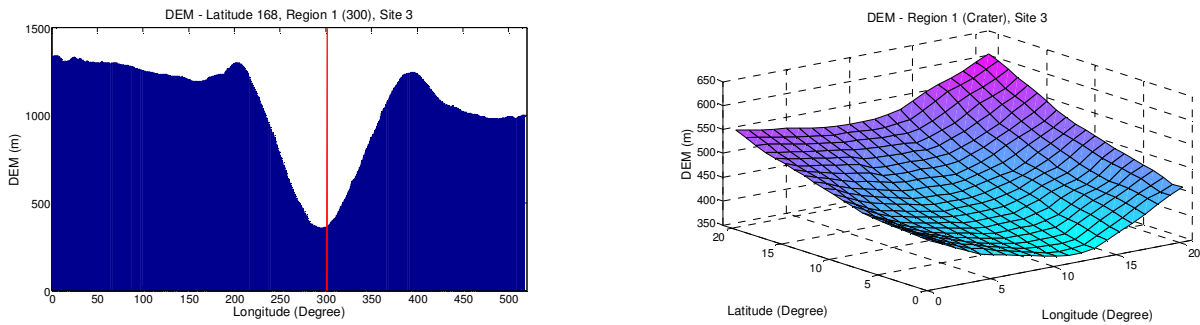


Figure 4.7: (a) DEM of 168th latitude position, showing transmitter location at 300th longitude position, in region *R1* inside the crater and (b) Close up view of 3-D DEM of the region *R1*.

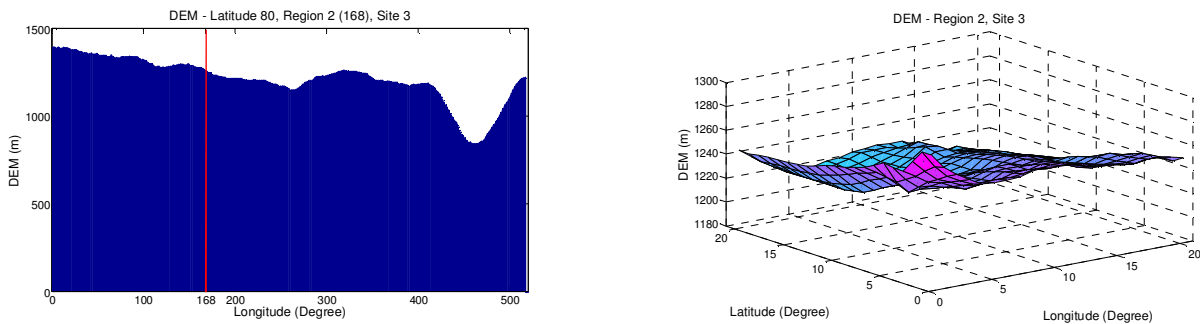


Figure 4.8: (a) DEM of 80th latitude position, showing transmitter location at 168th longitude position, in region *R2* outside the crater and (b) Close up view of 3-D DEM of the region *R2*.

4.5 Lunar Multipath Analysis Technique

The method shown for the analysis of lunar multipath environment and wireless link is summarized below:

- ❖ Suitable signal bandwidth was selected for the transmission over a lunar wireless link under consideration.
- ❖ A ratio (in dB) of LOS to a farthest multipath component was selected, giving a threshold in the PDP, up to which the lunar multipath components were allowed below the LOS signal component.
- ❖ Terrain based reflection coefficient of a given region was found and the maximum delay spread was obtained using Equation (4.8). The selection of unity reflection coefficient provided extreme condition on the number of multipath for a given link.
- ❖ The number of multipath was found using Equation (4.7).
- ❖ The reflectors were placed at random positions around the transmitter and the receiver.
- ❖ The power associated with all the signal components and their delays were calculated using Equation (4.4), based on actual DEM. This provided the PDP of the given link.
- ❖ The lunar wireless channel object was selected as Rician and the Rician k factor and the path gains for the given link were calculated using actual DEM of the lunar site.
- ❖ The error rate analysis was carried out, using the Rician k factor, the path delays and the path gains.
- ❖ The error rate analyses of all the links were carried out by moving the receiver in a given region.

One can also change the parameters, if desired, to carry out multiple iterations. For detailed analysis, one may take the average/rms value of the performance parameters in multiple runs.

4.6 Conclusion

This chapter has suggested a technique for the prediction of lunar PDP and the error rate analysis of the lunar wireless link, based on the proposed LWM. It has been shown, that the analysis of lunar multipath environment can be done using the suggested Lunar Wireless Model. The lunar PDP shows the exponential decay, similar to the outdoor model on the earth. The channel behavior is visualized by the suggested method. The maximum data rate

without the use of an equalizer is predictable from the LWM, for employment of lunar WSN. Exclusion of an equalizer simplifies the receiver design and consequently, reduces the mass and the size. The results are useful to predict the BER and the PER of a given link on the lunar surface. Typically, the BER reaches 10^{-4} and the minimum suggested SNR at the receiver is 15 dB.

Chapter 5

Design, Development and Testing of Wireless Impedance Sensor Node

A few recent lunar missions have found water ice present on the moon [5, 7, 159]. It has now been established that water on the moon is available in the form of ice, mixed with lunar regolith, though it may or may not be available at the surface level. However, all such results are based on remote observations from the orbiter. To detect the potential water bearing sites and to confirm the remote observations, in-situ measurements of water ice of different geographical locations are essential.

The unique detection of water ice requires endeavor to look for a method that can characterize a unique property of water or some process, which results due to the existence of water. There are many methods like infrared, neutron probe, Nuclear Magnetic Resonance (NMR), electrical, microwave and seismic that can detect the presence of water but only a few techniques can unambiguously and uniquely identify it, as being water. An electrical property sensor, to measure the permittivity of lunar regolith, can distinctively infer the presence of water. A Wireless Impedance Sensor Node (WISN) has been proposed and discussed for this purpose, in this chapter.

5.1 Need of Special Water Ice Sensor

Conventional soil moisture sensors may be based on techniques like neutron probe, capacitance probe, Time Domain Reflectometry (TDR) or Frequency Domain Reflectometry (FDR). Seshadri et al. [69] have attempted the impedance spectroscopy for detection of water in planetary regolith and Walker et al. [160] used mostly the reflectometry based sensor for soil moisture measurements. Commercially available soil sensors [9] are based on reflectometry, which generally have a long probe and the probe needs to be inserted inside the soil, to get better results. However, for future lunar or space applications to study the planetary surface science; such sensors are not appropriate due to the requirement of insertion inside the surface, as the rover would need extra energy to push the sensor inside. Also, there should be a mechanism as well for pushing the probe inside, adding further requirement of resources. Moreover, the sensor should be compact enough from size, weight and power point of view, in any space applications. In addition, reflectometry based sensors normally use frequency in MHz range, at which there is an ambiguity in differentiating between the dry regolith and ice, since the permittivity of regolith and ice are almost comparable in this range.

These are the motivating factors to design and develop a special water sensor, which is better suited for future lunar and other planetary applications, to carry out in-situ measurements. The impedance spectroscopy is a well established technique, used in the analysis of an electrochemical cell or electrolyte material. The embedded impedance sensor discussed in this chapter uses the frequency domain technique, giving whole frequency spectrum in the measurement range, by sweeping the frequency and it is a newer application of impedance spectroscopy for detection of water in the soil. The impedance sensor needs only an electrical contact with the surface for detection of water/ice. The developed lab model of impedance sensor is compact in size with Printed Circuit Board (PCB) dimensions of $50\text{ mm} \times 50\text{ mm}$ and has low mass of about 60 grams, which may be suitable for space and planetary applications. The sensor is also useful for similar terrestrial applications. It is beneficial for soil moisture detection in an agriculture application and for other applications based on impedance.

5.2 Algorithms

As shown in Figure 5.1 (a), a function generator produces a sinusoidal signal and feeds to a calibrating resistor and Device Under Test (DUT), which could be a regolith (soil) sample in the lunar application. The signal generator block could be a Direct Digital Synthesizer (DDS) AD9858 [161] and could be programmed to generate the frequency sweep. It is known that soil represents a dielectric material and its electrical equivalent circuit may be represented by a network like the one given by Mantovani and Calle [162]. Such complex soil electrical circuits demand the curve fitting to the impedance data for interpretation. In the present case, the simplest soil equivalent circuit is used as shown in Figure 5.1 (b), in which the capacitance accounts for dielectric nature of bulk soil and the resistance represents the leakage in it. Simplifying the soil equivalent circuit promises simplified algorithms, which are easier to be implemented for future space applications. The simplified algorithms can also avoid human efforts of curve fitting and ease in making the derivation of the final results automatic by software. In the following derivations, the bold phase quantities represent the vector quantities.

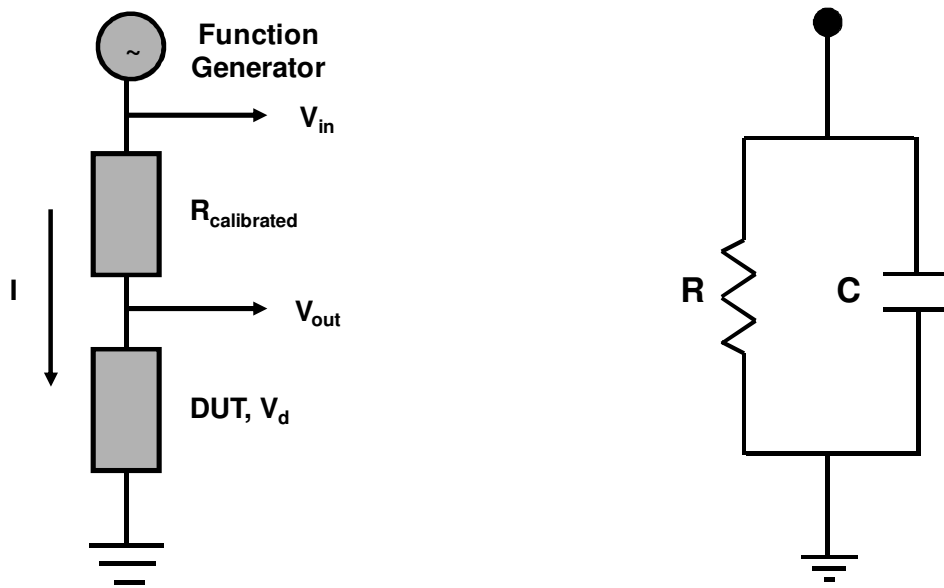


Figure 5.1: (a) Principle of impedance measurement and (b) Soil equivalent circuit.

5.2.1 Impedance Algorithm

Suppose $V_i = |V_i|$ is the input voltage signal from the signal generator and V_o is the output voltage signal, assumed as

$$V_o = |V_o| e^{-j\phi} = |V_o| (\cos\phi - j \sin\phi) \quad (5.1)$$

where ϕ is the phase shift between the input and output. The output voltage is given by

$$V_o = \left(\frac{Z}{Z + R_{cal}} \right) V_i \quad (5.2)$$

Simplifying Equation (5.2), one can obtain the impedance of a DUT as

$$Z = \left(\frac{V_o}{V_i - V_o} \right) R_{cal} = \left(\frac{|V_o| \cos\phi - j |V_o| \sin\phi}{|V_i| - |V_o| \cos\phi + j |V_o| \sin\phi} \right) R_{cal} \quad (5.3)$$

However, the impedance is a complex quantity given by

$$Z = Z_R + j Z_I \quad (5.4)$$

where Z_R and Z_I are the real and imaginary parts of impedance, respectively. Simplifying Equation (5.3), the real and imaginary parts of impedance are given as

$$Z_R = \frac{(|V_i| |V_o| \cos\phi - |V_o|^2) R_{cal}}{(|V_i|^2 - 2 |V_i| |V_o| \cos\phi + |V_o|^2)} \quad (5.5)$$

and

$$Z_I = \frac{|V_i| |V_o| \sin\phi R_{cal}}{(|V_i|^2 - 2 |V_i| |V_o| \cos\phi + |V_o|^2)} \quad (5.6)$$

respectively, in terms of the measurable circuit parameters. Now, considering soil equivalent circuit as a parallel combination of soil capacitance and soil resistance, as shown in Figure 5.1 (b), one can obtain the impedance of soil sample in terms of the capacitance and resistance as

$$\mathbf{Z} = \frac{R \left(\frac{-j}{\omega C} \right)}{R + \left(\frac{-j}{\omega C} \right)} = \frac{R}{1 + j \omega C R} \quad (5.7)$$

Simplifying Equation (5.7), one can deduce

$$\mathbf{Z} = \left(\frac{R}{1 + \omega^2 C^2 R^2} \right) + j \left(\frac{-\omega C R^2}{1 + \omega^2 C^2 R^2} \right) \quad (5.8)$$

Again, considering the complex impedance in the form given in Equation (5.4), the resistance and capacitance of soil sample are obtained as

$$R = Z_R \left[1 + \left(\frac{Z_I}{Z_R} \right)^2 \right] \quad (5.9)$$

and

$$C = \frac{-Z_I}{2 \pi f R Z_R} \quad (5.10)$$

respectively, in terms of the measurable circuit quantities.

Thus, the impedance of a sample is deduced from the input voltage, the output voltage and the calibration resistance in the measurement circuit. The capacitance of the sample is further obtained from the measured parameters. The capacitance of the soil is actually formed between the two measuring wires or probes, due to its dielectric nature. The probe length could be only few millimeters, just sufficient to make an electrical contact with the soil and measure the impedance, as mentioned in Section 5.4. This type of sensor does not necessarily have a long probe, while the commonly available soil sensors [9] generally have a long probe for soil testing.

5.2.2 Parameter Extraction Algorithm

The capacitance obtained from the impedance algorithm may easily be converted into permittivity, by considering a suitable geometry factor, based on the electrode configuration and dimensions.

From Equation (5.4), the admittance (Y) is given by $Y = \frac{1}{Z} = \frac{1}{Z_R + j Z_I}$

$$\therefore Y = \left(\frac{Z_R}{Z_R^2 + Z_I^2} \right) + j \left(\frac{-Z_I}{Z_R^2 + Z_I^2} \right) \quad (5.11)$$

But, the admittance of soil is related to its conductivity and also its permittivity as [69]

$$Y = g (\sigma' + j \sigma'') = j g \omega \varepsilon_0 (\varepsilon' - j \varepsilon'') \quad (5.12-a)$$

$$\therefore Y = g \omega \varepsilon_0 \varepsilon'' + j g \omega \varepsilon_0 \varepsilon' \quad (5.12-b)$$

where σ' and σ'' are the real and imaginary parts of soil conductivity, respectively; ε' and ε'' are the real and imaginary parts of soil permittivity, respectively; while ε_0 is the permittivity of free space. In Equation (5.12), $g = \frac{A}{d}$ is a geometry factor of the electrode configuration, having the electrode area A and the inter-electrode spacing d . Comparing Equation (5.11) and Equation (5.12), one can get

$$\varepsilon' = \frac{-Z_I}{g \omega \varepsilon_0 (Z_R^2 + Z_I^2)} \quad (5.13-a)$$

$$\varepsilon'' = \frac{Z_R}{g \omega \varepsilon_0 (Z_R^2 + Z_I^2)} \quad (5.13-b)$$

$$\sigma' = \frac{Z_R}{g (Z_R^2 + Z_I^2)} \quad (5.13-c)$$

$$\sigma'' = \frac{-Z_I}{g (Z_R^2 + Z_I^2)} \quad (5.13-d)$$

$$\sigma' = \omega \varepsilon_0 \varepsilon'' \quad (5.13-e)$$

$$\sigma'' = \omega \varepsilon_0 \varepsilon' \quad (5.13-f)$$

Therefore, the soil permittivity and conductivity are given in terms of the geometry factor and the measurable quantities of real as well as imaginary parts of impedance. Actually, $g \varepsilon_0$ is the capacitance of an empty cup.

5.3 Principle of Operation

A wireless impedance sensor in its simplest form is shown in Figure 5.2 (a) as a block [163] consisting of an impedance measuring circuit, a signal processing algorithm module, a memory unit and an RF transceiver. The sensor has two electrodes for impedance measurement, which make an electrical contact with the sample under test. The signal processing algorithm actually does the post processing on the recorded data and the results produced would be useful to infer if water is present in the soil. The results are stored in the memory and given to the 2.4 GHz transceiver. The data can be transmitted by wireless signal to the neighboring node or the data aggregator on the rover.

Impedance measurement in frequency domain generally requires changing the frequency of perturbation signal, in order to cover the entire range of interest. This implies slow signal processing and it is also quite tedious. However, if a frequency sweep or a chirp signal is used for measurement, then all the frequencies of interest are covered during one measurement cycle. The chirp is a linear frequency modulated signal in the simplest linear form and it can become complex when frequency time graph is non-linear. The chirp signal processing is extensively used in signal processing and reported in the literature like those given by Purdy et al. [164], Yu et al. [165], Pabari [166] and Pabari et al. [167]. The chirp signal works faster than the single frequency measurement and it is suggestive to sweep the frequency in the embedded impedance sensor. A typical up chirp signal is shown in Figure 5.2 (b). The mathematical details of chirp signal can be found in the literature.

The principle of operation of a compact impedance sensor is shown in Figure 5.3. The idea is to use an embedded system, in which a microcontroller sends a command to a signal generation block. The signal generation block produces a sinusoidal signal of the desired amplitude and frequency. To generate a frequency sweep signal, a Direct Digital Synthesizer (DDS) like AD9858 [161] from Analog Devices can be programmed and used. The sample and associated circuit block is actually a sample under test, along with necessary passive components to derive the current response of the sample. A precision resistance is used, in its

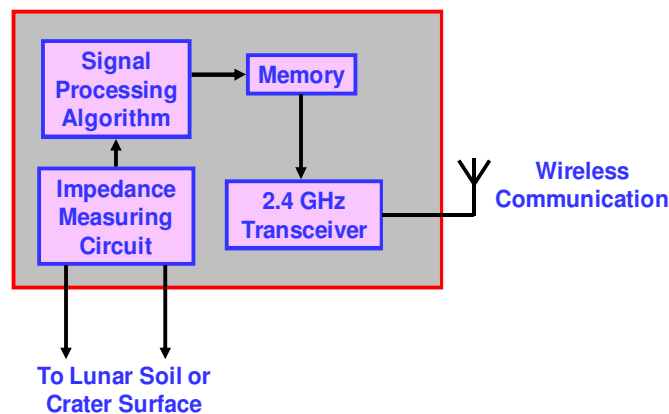


Figure 5.2: (a) Impedance sensor blocks.

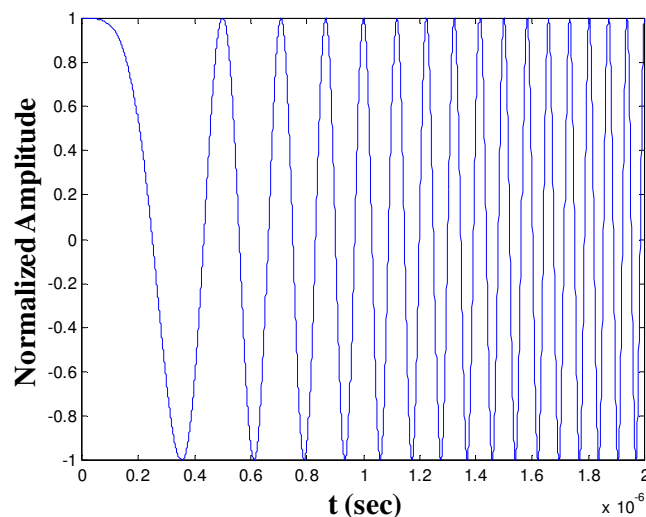


Figure 5.2: (b) A typical up chirp signal.

simplest form, to convert the voltage into current. An Analog-to-Digital Converter (ADC) takes the samples and feeds the data to a microcontroller. The microcontroller in turn

calculates the Discrete Fourier Transform (DFT) of the available data and stores the results thus produced, in the memory. The Fourier transform provides the information about the amplitude and phase of impedance under measurement. To implement this idea, AD5933 [168] impedance converter chip from Analog Devices has been selected, which simplifies the measuring task. Before implementing the sensor chip, it was programmed for soil moisture detection application. This was achieved by programming a USB microcontroller, provided on the evaluation board, with different combinations of parameters used in the impedance measurements. The response is sampled and converted into the digital signal by the ADC. Using available samples, the 1024 point Discrete Fourier Transform (DFT) is obtained and the results are made available in the specified memory locations. The microprocessor has to carry out multiple tasks like initiating impedance measurement, collecting and storing the results, dealing with the communication protocols and the device calibration.

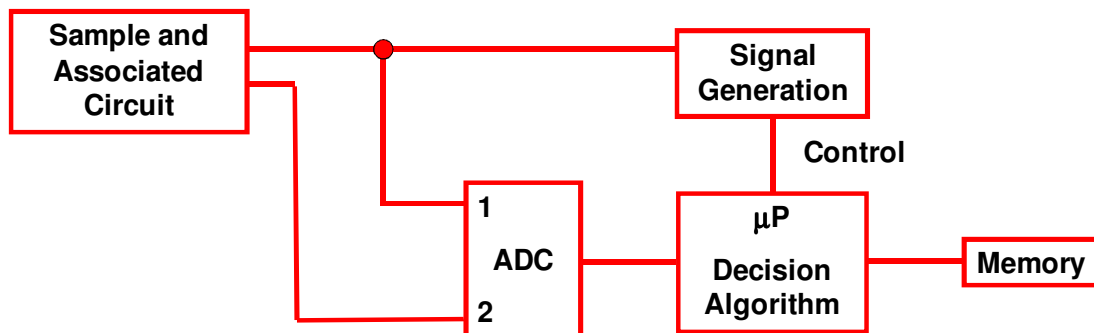


Figure 5.3: Principle of operation of impedance sensor.

5.4 Design, Evaluation and Development of WISN

The impedance measurement includes all effects like connecting cables and parasitic effects. If these effects are not identified and eliminated, they lead to systematic errors during the information extraction, from the impedance data. It is also important to be able to assign parts of the impedance data to their causes, for comprehensible modelling and precise information extraction. The electrode geometry is an important factor in order to avoid the parasitic effects in the stray field. Since impedance sensor needs only an electrical contact

without really needing a specific length of the probe, the probe can be as short in length as desired, in principle; as long as it makes an electrical contact with the soil and measures the impedance correctly. In the present experiment, two bare copper wires with 1 mm diameter have been used with a distance of 15 mm between them and were contacted about 8 mm with the soil, filled in a designed cup. However, the soil permittivity has also been checked using the probe spacing of 15 mm, 25 mm and 35 mm, and the matching results have been found in all cases. One has to model appropriately, to extract the precise information from the impedance data. The measuring probe is connected to the sensor electronics.

The Wireless Impedance Sensor Node (WISN) consists of impedance measuring chip connected to a microcontroller, which is programmed to communicate with the sensor chip. The microcontroller is programmed using a computer through the USB port. The data are stored in the memory for further use. The RF transceiver, capable of communicating in wireless mode at 2.4 GHz frequency in the license free Industry Scientific and Medical (ISM) band, is connected to the microcontroller. The choice of the frequency permits the use of miniaturized antenna for the nodes and it is very advantageous for future space applications. The data stored in the memory are transmitted to a data aggregator in wireless mode by the transceiver, through the antenna. The RF front end is optional to increase the transmitter power. The detailed design is depicted in Figure 5.4 (a). Dimensions of PCB of the sensor promise very compact size of 50 mm \times 50 mm. The final size of the sensor is 60 \times 64 \times 36 mm³. The details of the PCB and the snapshots of the WISN are shown in Figure 5.4 (b) to Figure 5.4 (e). The measurement frequency of the WISN depends on the user supplied master clock frequency and in the developed model, the sensor is fed with a master clock frequency of 16 MHz. The capability of measuring at frequencies below the present value of 10 kHz could be achieved by applying a lower value of the master clock frequency.

There is no salinity on the moon [141], and water, if present, would be in pure form. If water molecules are trapped in the permanently shadowed regions of the moon near its south pole, then water could be found in a pure ice form. Permittivity of water or ice, in general, depends on temperature and frequency of measurement. Experimental evidence indicates that the permittivity of ice may be considered independent of both, the temperature (below 273 K) and the frequency, in the microwave range and may be assigned a constant value of 3.15 [73].

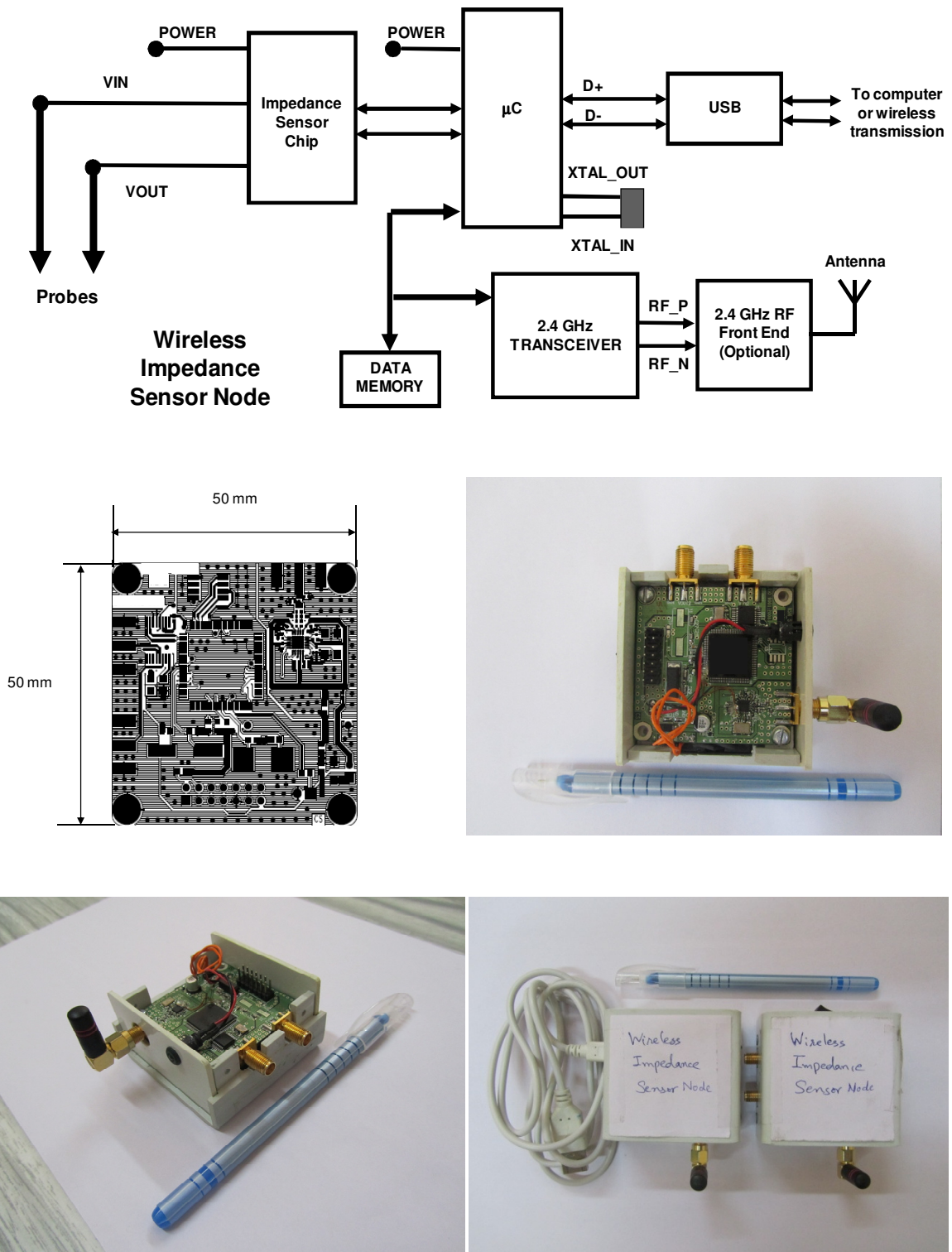


Figure 5.4: (a) Developmental blocks of WISN (top), (b) PCB details (middle left), (c) Top snapshot of WISN (middle right), (d) Side snapshot of WISN (bottom left) and (e) Snapshot of measuring WISN and data aggregator WISN (bottom right).

However, at lower frequency in the kHz range, the permittivity of ice depends considerably on temperature. Also, there is a difference in the upper knee point frequencies in the real permittivity plots of water and ice, as shown by Stacheder [74]. At 273 K temperature, the real part of permittivity of ice is given as 38.11 (at 10 kHz) and as 4 (at 100 kHz), with the upper knee point frequency at 1 kHz [74]. The present WISN model is fed by 16 MHz master clock and has a measurement range from 10 kHz to 100 kHz, which signifies that WISN in the present form can be used to measure permittivity of ice at 273 K.

The upper knee point in the real permittivity plot of ice could vary from less than 1 Hz [75] in colder region of the moon to 1 kHz [74] at 273 K, depending on temperature. To operate the WISN below 273 K for measuring permittivity of ice, it requires the operating frequency to be lower than the presently used value; which can be achieved by a suitable selection of master clock frequency. For instance, to measure the permittivity of ice around 260 K, the upper knee point is at about 100 Hz [75] and the WISN can be fed with a 500 kHz master clock frequency to work in 100 Hz to 1000 Hz range to differentiate between the ice and regolith. The transition region (from upper knee point frequency to lower knee point frequency) of real permittivity of ice is comparatively in lower frequency range from few Hz to few kHz and it shifts right or left depending on increase or decrease in the temperature. The temperature of a given lunar site (or for a given application) could be known from the site survey data (or literature) and hence, estimates of knee point frequencies of ice could be known ahead of time. Accordingly, the WISN is fed with a suitable master clock frequency to differentiate between the ice and regolith.

Moreover, if water in the form of ice is present on the moon, it could be mixed with the regolith and the effective permittivity is contributed by regolith and ice, both. The resultant value would be more than that of the regolith alone and less than that of the ice alone. Typical transition regions of permittivity of the ice are from 90 (at 1 kHz) to 4 (at 100 kHz) at 273 K temperature [74] and from 92 (at 100 Hz) to 4 (at 3000 Hz) at about 260 K temperature [75]. The real permittivity of ice (ϵ_{r_ice}') in the transition region is, therefore, given as $4 \leq \epsilon_{r_ice}' \leq 90$ (or more at lower temperatures) in lower frequency range. The real permittivity of water is about 80 at room temperature in lower frequency range, as

found in the literature [169]. The lunar regolith dielectric constant is about 4 to 6 as given by Buehler et al. [70] depending on the density.

Soil being a porous medium, it has air portion also, along with the soil and therefore, the value of effective permittivity is less than that of the soil alone, depending on porosity. Wet soil has three components present in it, viz., soil, air and water. The effective permittivity of the mixture is dependent on volumetric fractions, as well as permittivity of all the three. The maximum value of effective permittivity of wet soil is bounded by [170]

$$\overline{\varepsilon_{max}} = P_s \varepsilon_s + P_w \varepsilon_w + P_a \varepsilon_a \quad (5.14)$$

where $\overline{\varepsilon_{max}}$ = maximum relative permittivity of mixture

P_s = volume fraction of soil

P_w = volume fraction of water

P_a = volume fraction of air

ε_s = relative permittivity of soil

ε_w = relative permittivity of water

ε_a = real relative permittivity of air

Equation (5.14) is written in terms of volumetric water content (θ) and porosity (η) as

$$\overline{\varepsilon_{max}} = (1 - \eta)\varepsilon_s + \theta \varepsilon_w + (\eta - \theta) \varepsilon_a \quad (5.15)$$

The measured value of permittivity, which is more than that of the dry regolith, indicates that the mixture is not only the soil, but also carries a portion of ice (neglecting the contribution by air, being a small value due to its relative permittivity of unity). Since, the permittivity of ice is higher than that of the dry regolith in the transition region as mentioned before, the WISN can be useful to differentiate between the regolith alone and the ice mixed with the regolith, by judicious selection of user defined master clock frequency. The measured data can be transmitted in wireless mode to a distant rover, navigating the lunar surface.

5.4.1 Merits of WISN over Existing Sensors

- The neutron probe uses permanent metal access tubes into the soil [101], for soil moisture measurement. The capacitance probe also requires installation of permanent access tubes and operator intervention is necessary [101]. It is a new application of the impedance spectroscopy to detect water ice and few experiments were carried out, using either an impedance meter or a signal generator and an oscilloscope, before final design was decided in case of WISN. The selection of sensor chip AD5933 [168] promises a very compact size of the sensor. The overall reduction in mass and volume of the sensor is a basic need for any payload in a space mission. Also, automation is necessary and operator intervention is not feasible in unmanned space applications. The WISN, therefore, encourages its use for detection of water ice in future space missions, due to its compact size. Also, the impedance sensor has been made to operate in wireless mode; which is the only feasible way to communicate in space.
- Second advantage of the impedance based sensor design is the reduction in probe length. The technique shown in [101] uses an oscillator, a resistor, a transmission line and a soil probe for soil moisture measurement; using a simplified impedance technique with the suggested probe length of 60 mm. Such techniques are not feasible to be implemented in space, due to bulky size. Also, the commercially available soil sensors are based on reflectometry with longer probe length, typically about 50 mm [9] and their probe length could be dependent on the wavelength. In case of WISN, the dependence of probe on wavelength is avoided and the probe length could be reduced to a minimum necessary for an electrical contact. The effective contact of about 8 mm with soil has been used, which shows a drastic reduction of about one sixth in probe length, compared to existing sensors.
- Third merit of WISN is the use of simplified algorithms for data interpretation and avoidance of curve fitting, which is typical in some cases.
- Reflectometry sensors and other technique [9, 101] use operating frequency in MHz range, at which there is an ambiguity in differentiating between the dry regolith and ice; since the permittivity of regolith and ice are almost comparable in this range. In

present case, WISN can be made to operate in transition region of permittivity of ice, by feeding an appropriate master clock. This promises applicability of WISN for lunar and planetary surfaces, where water could be in ice form due to very low temperatures.

- Another advantage is that, WISN gives the permittivity as a function of frequency in contrast to existing sensors, which give a single point measurement. Additional information [171], which may be derived by such frequency sweeping capability of the WISN, could be the observation of low frequency relaxation and possible measurement of activation energy. Modeling of soil impedance may also be carried out in the measurement range of interest, using permittivity as a function of frequency.

Thus, there are many advantages of WISN over existing sensors, proving its use for future planetary applications.

5.5 Experimental Set Up

The arrangement of experimental set up used for testing is depicted in Figure 5.5. A cylindrical sample cup of 40 mm diameter and 40 mm clear height was made from Perspex or Poly Methyl Methacrylate (PMMA) material. Perspex is optically transparent and offers very low capacitance. Both properties of the material are essential for the experiment. The sample cup is a top loading cup, with a lid having two holes for placing electrodes. Two metallic electrodes are inserted inside the cup for carrying measurement signals to and fro the sample.

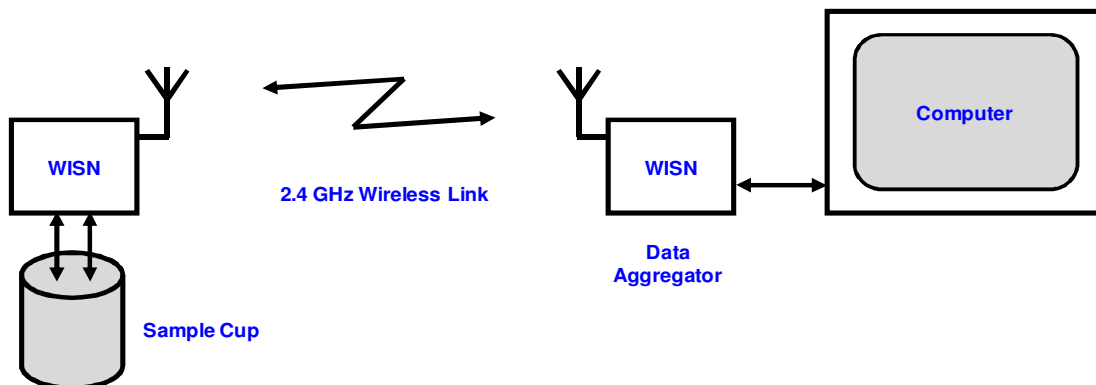


Figure 5.5: Experimental Set Up for Testing.

The distance between the electrodes was kept 15 mm, in the newly designed cup. The sample under test is filled inside the cylindrical cup and the electrodes are connected to the WISN on the other side. The other WISN, called data aggregator is connected to a computer for data collection. The WISN, connected to sample, takes the measurements and transmits the data to the data aggregator in wireless mode, at 2.4 GHz frequency.

5.5.1 WISN Calibration

During evaluation phase of the sensor, soil equivalent circuit was tested for its impedances of theoretical and measured values [163]. In Figure 5.6, the real and the imaginary measured impedances as well as the real and the imaginary theoretical impedances are shown as a function of frequency. The responses indicate one-to-one match between the measured and theoretical impedances in the measurement range of 10 to 100 kHz, as depicted in Figure 5.6 [163]. The sensor is calibrated by a high precision resistor. The responses of few precision resistors are shown in Figure 5.7 (a). The resistors have their associated stray capacitances due to metallic leads and they can cause non-ideal characteristics during calibration of the sensor. It is seen from Figure 5.7 (a) that, as the value of resistor is increased, the stray capacitance is also increased. Total stray capacitance is contributed by leads of the resistor and measuring probes. Its value can be as high as 1 pF, as depicted in Figure 5.7 (b) and can lead to large errors, if not taken care.

5.6 Results and Discussions

Testing was carried out in four different phases using the WISN, viz., for terrestrial sand type soil in phase I, for Milli-Q [157] water in phase II, for ice in phase III and for lunar soil stimulant JSC-1A [77] in phase IV. Different materials had been selected to check capability of the developed sensor to measure the impedances of various materials and to derive the electrical properties of the materials from the impedances.

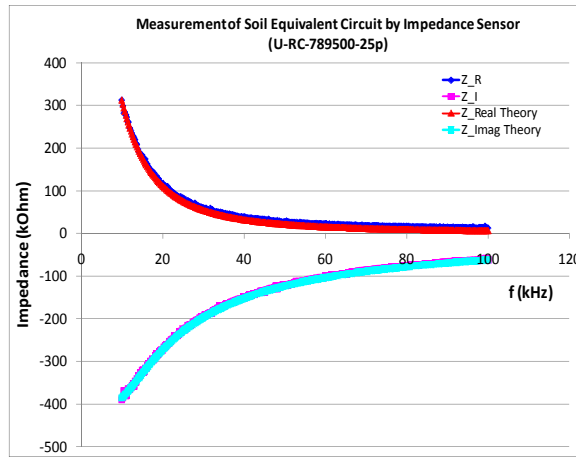


Figure 5.6: Plot of Z_R (measured, blue), Z_I (measured, magenta), Z_{Real} Theory (theoretical, red) and Z_{Imag} Theory (theoretical, cyan) versus frequency.

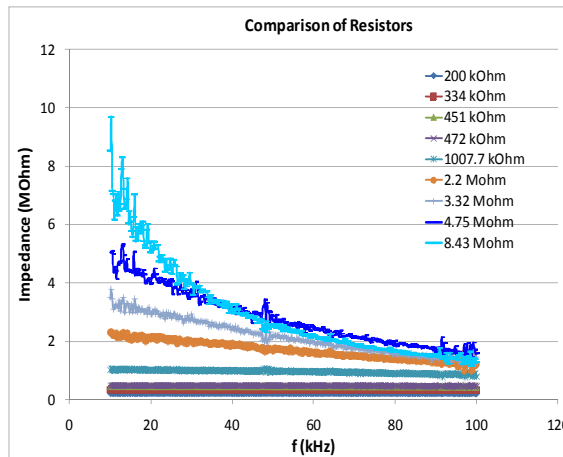


Figure 5.7: (a) Response of resistors.

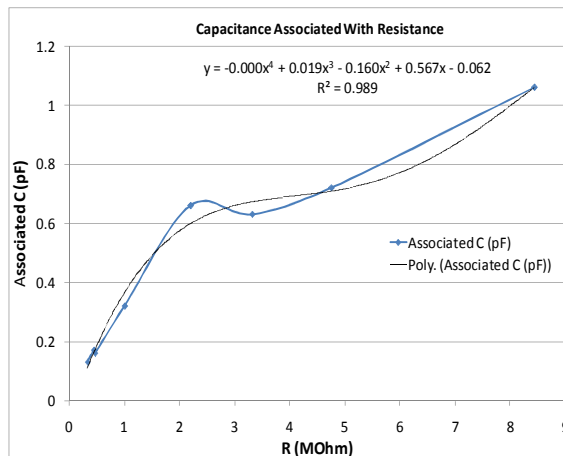


Figure 5.7: (b) Capacitance associated with resistance.

5.6.1 Terrestrial Soil Testing (Phase I)

The purpose of testing the sand type terrestrial soil was only to establish the technique for differentiating soils with various water contents, during early evaluation of the sensor; and not to derive its permittivity. This is because; lunar soil is different than sand and therefore, no further processing was considered for the sand, after deriving capacitances of the samples. This testing phase was useful to check the sensor performance for soil, in general.

A sample cup with two electrodes was made for soil testing and terrestrial samples of sand type soil were taken. The samples were allowed to dry at 100 degree Celsius for one day. Moisture testings were carried out using the WISN for dry soil, soil with 0.5 % water and soil with 1 % water. A photograph of the sand is shown in Figure 5.8 (a). The capacitances of all samples were derived using Equation (5.10) and results are given in Figure 5.8 (b). The results show that the sensor can easily differentiate three types of samples.

Some of the outlier points in the results are due to digital nature of the sensor, having slight oscillations in the calibration. Since, these measurements were taken during early evaluation of the sensor, using slightly different cup and electrode spacing, as compared to those used for the remaining testing phases given in Subsection 5.6.2 to Subsection 5.6.4; the capacitance values are not directly comparable to that in Subsection 5.6.4.

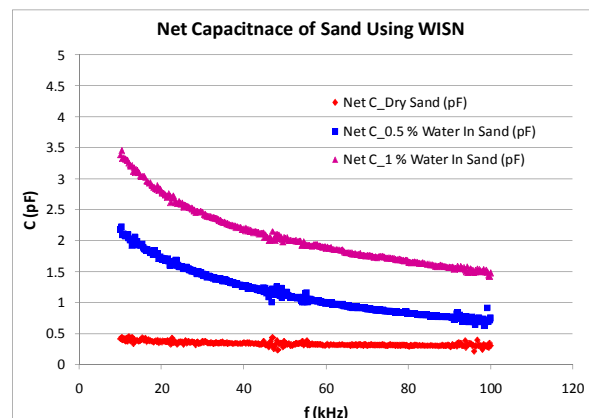


Figure 5.8: (a) Snapshot of sand type soil and (b) Capacitance versus frequency results of sand for various water contents.

5.6.2 Milli-Q Water Testing (Phase II)

In order to verify the WISN capability to measure the permittivity of a known substance, Milli-Q [157] water had been selected. Milli-Q [157] water is ultra pure water. The permittivity of pure water is reported in literature [67, 68]. The results given by Batalioto et al. [67] for relative permittivity of Milli-Q water are shown in Figure 5.9.

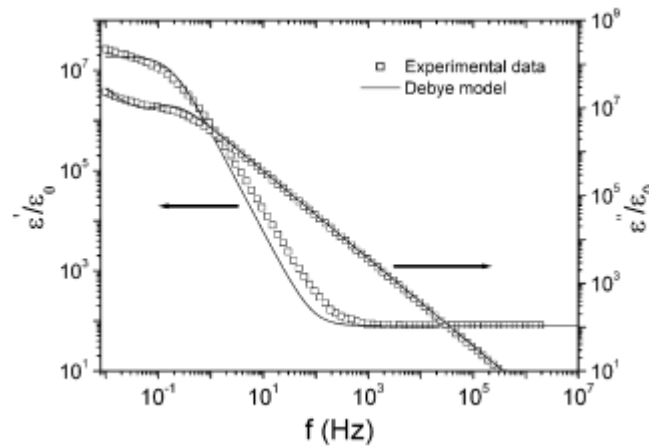


Figure 5.9: Real (ϵ') and imaginary (ϵ'') parts of dielectric constant of Milli-Q water (Courtesy: Batalioto et al. [67]).

In testing phase II, samples of Milli-Q water were collected and tested using the WISN under various conditions. During this phase, a newly designed cup having two electrodes was made for impedance measurement. Two bare copper wires were used as electrodes, with 15 mm spacing between them. During this testing phase, stray capacitance of the order of few hundreds of femto Farad was found due to testing probes. The presence of this stray capacitance was verified by using known capacity of capacitors, whose capacitance values were measured using precision component analyzer from Wayne Kerr Electronics [172]. Moreover, the capacitance between a pair of parallel wires obtained by a standard equation [173] may be useful in calculating the results for offsetting the effects of stray capacitance. The real and imaginary parts of permittivity of Milli-Q water, obtained from measurements by the developed sensor, are shown in Figure 5.10. The results given by Batalioto et al. [67] for relative permittivity of Milli-Q water are 80 for real part throughout the measurement range

and about 120 for imaginary part, at 10 kHz frequency. The results shown in Figure 5.10 agree with those given in Figure 5.9. This verifies the results obtained by the sensor and proves its excellent performance.

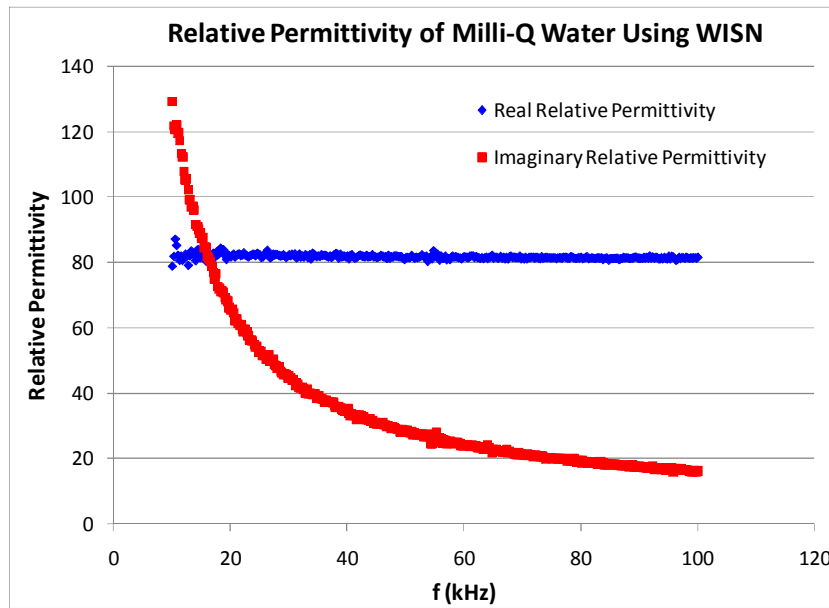


Figure 5.10: Real (blue) and imaginary (red) relative permittivity of Milli-Q water.

5.6.3 Ice Testing (Phase III)

The permittivity of ice in the low frequency range is reported in the literature [74, 75] at different temperatures. To check the performance of the WISN for ice, a few samples of pure ice were prepared in the laboratory and tested using the WISN. Electrode configuration was kept the same, as that used in phase II and the temperature was measured by a thermometer. As mentioned in Section 5.4, when temperature changes to lower values, the permittivity curve shifts to the left. This indicates the measurement frequency to be lower and such measurements are taken by changing the master clock frequency of the WISN to lower value, as given in Section 5.4.

The ice results given by Stacheder [74] are at 273 K. The testing of the ice was carried out by the WISN at a temperature of 273 K and the results obtained are shown in Figure 5.11.

The results measured by the WISN and the results given by Stacheder [74] are presented in Table 5.1 for real permittivity of ice. The imaginary permittivity is also shown in Figure 5.11, which actually represents a loss component. It is seen from Table 5.1 that the measured values agree with the reported values, which conveys that the sensor can also be used for sensing the ice.

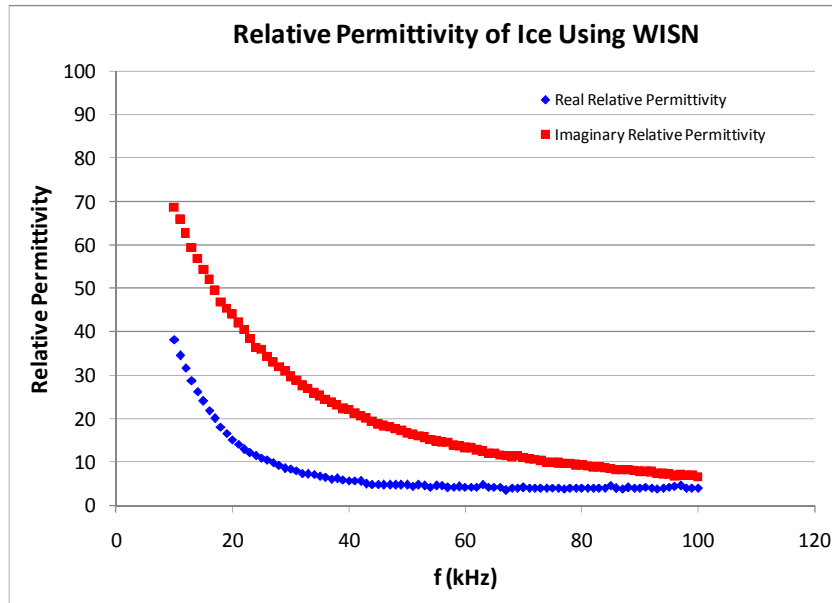


Figure 5.11: Real (blue) and imaginary (red) relative permittivity of ice at 273 K.

Table 5.1: Comparison of permittivity measured by WISN with the reported values

| Frequency (kHz) | Real Permittivity Measured by WISN | Reported Real Permittivity [74] |
|-----------------|------------------------------------|---------------------------------|
| 10 | 38.20 | 38.11 |
| 100 | 4.01 | ~ 4 |

5.6.4 Lunar Soil Simulant Testing (Phase IV)

The sample cup and the electrode configuration used in this phase were the same as those used in phase II and phase III, to keep the same calibration. To check the performance of WISN for soil on the moon; lunar soil simulant JSC-1A [77] was considered for testing,

which is quite similar to JSC-1 [76]. Photograph of JSC-1A is shown in Figure 5.12 (a). The JSC-1A sample was heated at 100 degree Celsius for 24 hours to make it dry. Various soil samples as dry soil, soil with 2 % water content and soil with 5 % water content were prepared, by adding high quality Milli-Q [157] water in appropriate proportions. Such samples of JSC-1A [77] were tested using the WISN and the capacitances of the samples, derived from Equation (5.10), are shown in Figure 5.12 (b). As mentioned earlier, there are some outlier points in the results due to sensor.

From the results in Figure 5.8 (b) and Figure 5.12 (b), one can infer that the sensor should be operated comparatively in lower frequency range as far as possible, to distinguish various moisture contents easily. It is seen that as water content is increased, it actually adds value in dielectric behavior and the curve becomes more and more hyperbolic in nature. This type of variation is expected due to dielectric nature of pure water. Variation of permittivity with respect to frequency has been reported by Dam et al. [72] for wet soil. The results of the ultra pure water have been obtained using the WISN, as given in Subsection 5.6.2.

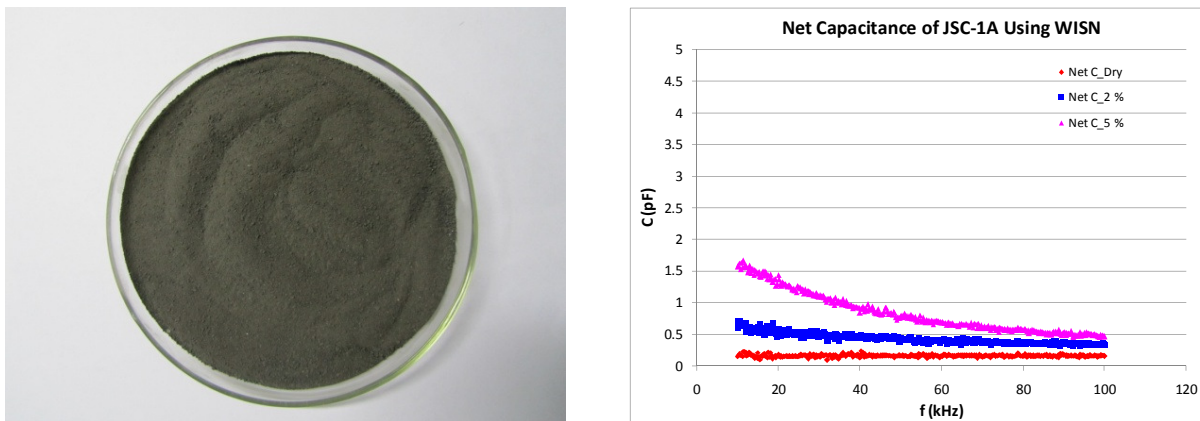


Figure 5.12: (a) Snapshot of JSC-1A and (b) Capacitance versus frequency results of JSC-1A for various water contents.

Atkins et al. [174] have typically measured the minimum soil capacitance of 22.4 pF, using a capacitance probe and considered the air capacitance of 3.5 pF, during their soil testing phase. In present experiments, the WISN has typically measured the minimum soil capacitance of about 0.6 pF, with the air capacitance of about 0.4 pF. The WISN has detected a capacitance change of about 1.5 pF for JSC-1A; when water is varied from 0 % (dry

sample) to 5 %, with the smallest change of as low as 0.2 pF. These results show the excellent potential of WISN and prove for its future possible applicability on the moon, after proper calibration. From Figure 5.8 (b) or Figure 5.12 (b), one can easily derive the calibration plots to detect the percentage of water in given soil.

Moreover, the permittivity and conductivity of JSC-1A were derived from the measurable quantities, based on the parameter extraction algorithm given in Subsection 5.2.2, for measurement frequencies from 10 kHz to 100 kHz. These results are shown in Figure 5.13 and Figure 5.14, respectively.

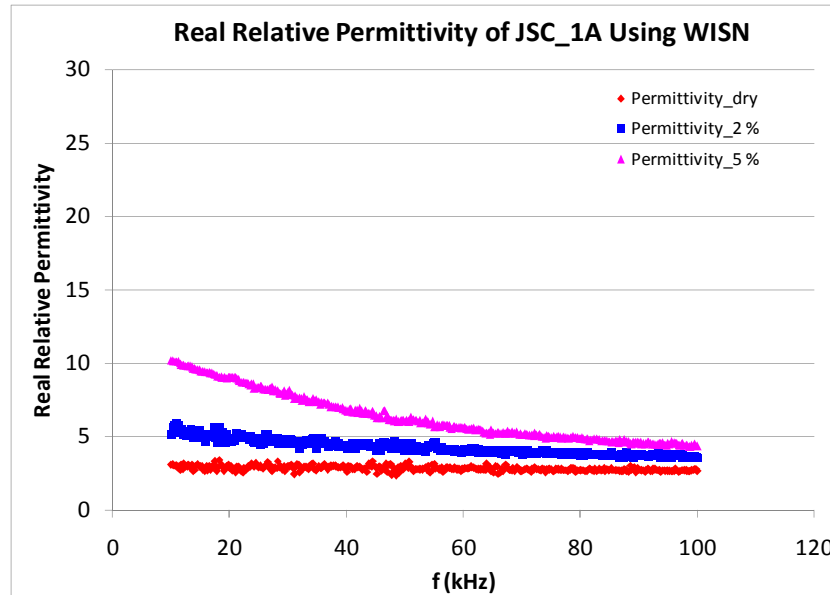


Figure 5.13: Real relative permittivity of JSC-1A, for various water contents.

The porosity of the sample was found by measuring the bulk density of the sample and taking the particle density of JSC-1A as 2.928 gram per cube cm [175]. Krotikov [176] has given an approximate relationship between the dielectric constant of dry soil and its density and his equation gives the value of ϵ_s as 6.1 for JSC-1A. Buehler et al. [70] have given the dependence of dielectric constant (ϵ') of soil on the density (ρ) as

$$\epsilon' = 1.56 \rho^{1.3} \quad (5.16)$$

Lunar samples measured by Buehler et al. [70] also fall on this exponential line and therefore, the relationship given in Equation (5.16) has been used for calculation. The value of ϵ_s for JSC-1A using Equation (5.16) is 6.3, ϵ_a for air is unity, while ϵ_w for water at room temperature is given as 80 [169]. These constants were taken as the inputs and the maximum

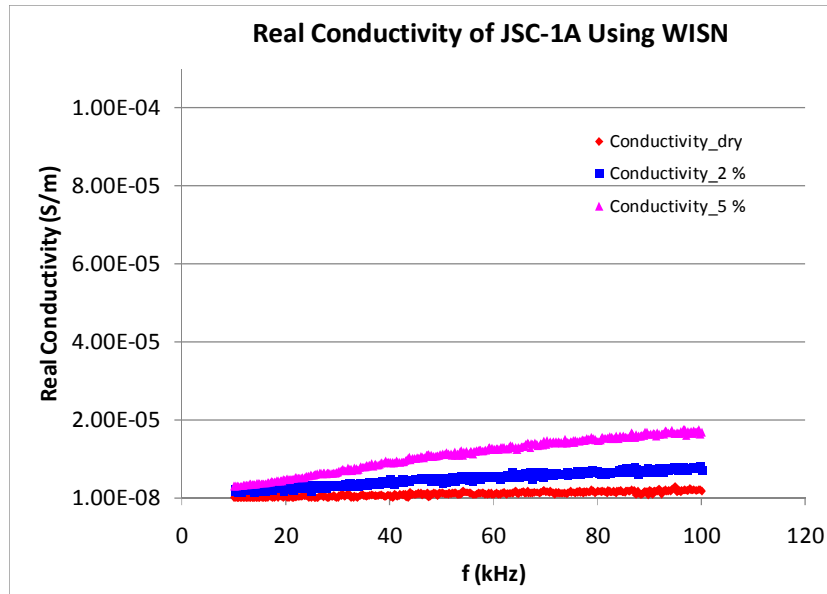


Figure 5.14: Real conductivity of JSC-1A, for various water contents.

values of real relative permittivity of the mixtures were found using Equation (5.15) for various samples of certain porosities, based on the volumetric fractions of soil, water and air. The volumetric water contents, the measured porosities and the estimated upper limits of permittivity of mixtures are shown in Table 5.2.

Table 5.2: Volumetric water contents, measured porosities and estimated upper limits of permittivity of mixtures

| Percentage Water in JSC-1A | Volumetric Water Content (θ) | Measured Porosity of Mixture (η) | Estimated Upper Limit of Permittivity |
|----------------------------|---------------------------------------|---|---------------------------------------|
| 0 | 0 | 0.379036264 | 4.29 |
| 2 | 0.036363636 | 0.50633383 | 6.49 |
| 5 | 0.090909091 | 0.583954297 | 10.39 |

The results shown in Figure 5.13 were carried out in frequency range from 10 to 100 kHz using the WISN at room temperature of 305 K and the measured values of permittivity of samples are found within the expected limit. Since, the permittivity is a function of frequency as well as temperature; its value can differ at other temperatures. Nurge [75] has shown for the lunar soil simulant JSC-1A, that the value of real permittivity is 10 for 12 % water in the sample at 160 K temperature, while it is 10 for 8 % water in the sample at 174 K temperature. These suggest that the slope of characteristic rises as temperature is increased and explains the dependence of permittivity on temperature.

5.7 Thermal and Space Qualification Consideration

The sensor package should be as compact as possible to reduce the volume from space application point of view. This is achievable by using the impedance sensor for water ice detection. Since environment of the moon is hostile as mentioned in Chapter 2, the sensor hardware has to be protected from the extreme temperature changes. The exact environmental specifications can be known only after the landing site is decided, which is most likely to be in the polar regions due to possibility of finding water ice mixed with the regolith. There are many regions near the poles of the moon having permanently shaded region, also called cold traps sometimes, where water may be found in ice form. Also, there are places near such regions where sunlight reaches only for some duration, e.g., near Malapert mountain. The temperatures of such regions normally remain about -50 to -30 degree Celsius.

The operating temperature for space qualified components is generally -55 to +125 degree Celsius. The components and electronics package will have to be separately qualified and tested for lower temperatures. Since the operating temperature of electronics cannot be lower than -55 degree Celsius, the sensor packages may have to be kept warm from inside to make the electronics operating. One way to achieve this is by using battery powered heaters [177] mounted around the sensor. Another solution for keeping the electronics warm is by means of self power dissipation, automatically controlled by some sensing mechanism provided inside the package. Third possible solution to mitigate this problem is to use Multi

Layer Insulation (MLI) [178] or thermal blankets wound around the package, which is a normal practice for space applications.

There is a large amount of cosmic radiation occurring on the moon. This demands the sensor package to be radiation hardened. The space qualifications of on board instruments are usual practices of space agencies like National Aeronautics and Space Administration (NASA), Indian Space Research Organization (ISRO), European Space Agency (ESA) and others. The sensor package has to pass through all space qualification tests, outlined by such space agencies. Vladimirova et al. [85] have attempted to characterize the wireless sensor motes for space applications.

5.8 Conclusion

This chapter has proposed a Wireless Impedance Sensor Node (WISN) for the lunar WSN to detect water ice in the soil. The lab model of the WISN has been developed for future lunar and planetary applications and it is a distinct entry in the domain for soil moisture detection. It is compact enough to be considered for space and planetary surface science applications, with very small probe length, of the order of few mm. The WISN works based on derived impedance algorithm. The permittivity and the conductivity of the samples are obtained by the parameter extraction algorithm, from the measurable quantities. The sand type terrestrial soil and the lunar soil simulant JSC-1A were tested using the WISN. The sensor performance was verified by testing Milli-Q water in the measurement range of interest. The capability of the WISN for detecting the ice was verified. The results of water and ice agree with those given in the literature and promise that the WISN can be used for future planetary applications.

Chapter 6

Investigation of Sensor Deployment Schemes

For any WSN, it is of the utmost important to deploy the sensors with optimum choice. In case of a manual deployment, the sensors are deployed at the site of interest with accurate positioning. In a partly controlled deployment, a moving vehicle drops the sensors from predefined points and the sensors reach the surface. Normally, manual and partly controlled deployments are used for terrestrial sensor networks. However, for space and planetary applications like that on the moon, the manual deployment or partly controlled deployment is not feasible as it is outside the earth and therefore, only a random deployment is the choice left. The random deployment is achieved by means of probably a lander type packet, falling from the orbiter or by a launcher, mounted on the rover. Along with a suitable sensor deployment scheme, it is also very important to minimize the number of sensors for a given probing region of interest with the highest level of wireless connectivity.

In circular and spherical segment schemes [142] suggested in this chapter; it is assumed that the sensor packets, which may have some initial rotation to maintain the direction, are detached from the satellite orbiting around the moon and fall vertically downward, towards the selected crater of the moon due to gravity. It is further assumed that

the packet velocities are damped, when they reach near the lunar surface and the sensors are ejected from the packet at a certain height from the surface. The third deployment scheme, i.e., the parabolic scheme [142] launches the tiny wireless sensors inside a crater using a mini launcher, either on a lander or a rover at the crater edge. For all the three methods, it is also assumed that the necessary tiny wireless sensors are available, which can work in lunar environment. These sensors are put in appropriate scenarios to check practical aspects of such deployment schemes. The Newton's laws of motions remain valid for planetary applications as well and have been used in the work for deriving the equations governing the trajectories of various topologies. It is known that the gravity of the moon is 1.622 metre per square sec [2] and it is taken in all calculations in this chapter.

6.1 Circular Deployment

Considering the target application for future planetary exploration, only limited amount of size and weight are permitted for payloads or sensors due to many limitations like launching facility, energy and cost involved. If one can reduce the number of sensors to be deployed, it can further reduce the weight and size of the sensor payload, but at the cost of reduced topographical coverage. However, the number of sensors is also decided by the line-of-sight communication range between the sensors. An application scenario is considered in which the sensors are ejected from an orbiter towards the circular graphical region (with radius R) on the lunar surface in a two dimensional plane.

As mentioned above, it is assumed that enough number of water ice sensors, capable of working in hostile environment are available; the sensor packet is detached from the orbiter; its initial velocity is reduced and after reaching a particular drop point with height h from the lunar surface, the sensor packet is opened by releasing pressure inside. Small sensors are packed between two circular rings as shown in Figure 6.1, with a facility to release the pressure from centre of an inner ring. After achieving the desired altitude, the sensor packet is opened with horizontal thrust to throw the sensors in radial directions, creating some initial horizontal separation among them. This initial horizontal separation among the sensors is

needed for geographical coverage of the crater or region, as there is no wind on the moon and hence no natural horizontal force exists. Also, from this initial height h , all sensors start their

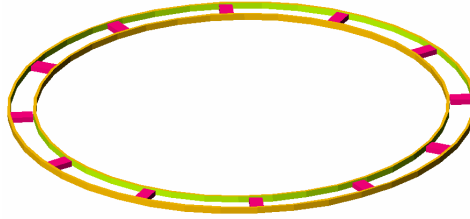


Figure 6.1: Circular ring package for sensor deployment.

downward journey towards the lunar surface due to gravity of the moon. For the geographical region under consideration, the drop point (from where the package is opened) and its corresponding point on lunar surface are assumed to be the origins in respective planes for simplicity. The centre of the ring structure is concentric with these points, i.e., at $(0, 0)$. If the sensors are packed between two circular rings having initial locations as (r, θ_j) , where $j = 1, 2, \dots, n$ and r is the average of two radii of circular rings of sensor packet, then the angular separation between any two consecutive sensors is approximately $(2\pi/n)$ for n sensors. For the vertical velocity components,

$$-h = v_i t + \frac{1}{2} a t^2 = -\frac{1}{2} (1.622) t^2 = -0.811 t^2$$

giving the time of flight,

$$t = 1.11 \sqrt{h} \quad (6.1)$$

Also,

$$-v_{fy} = v_{iy} + a t = -(1.622) t = -1.8 h^{0.5}$$

$$\therefore v_{fy} = 1.8 \sqrt{h}$$

For the horizontal velocity components, the distance travelled by each sensor is,

$$d = v_i t + \frac{1}{2} a t^2 = v_{ix} t = 1.11 v_i \sqrt{h} \quad (6.2)$$

Also, $v_{ix} = v_{fx} = v_i$ and $v_{iy} = 1.8 \sqrt{h}$ giving the final impact velocity of sensor as

$$v_f = \sqrt{v_i^2 + 3.24 h} \quad (6.3)$$

If pressure p is released from the centre of the inner ring and the vertical dimension of the ring structure is y , then the force exerted on the inner ring due to this pressure is $(2 \pi r_i y p)$ and the distance travelled by each sensor will be d from its initial rest position, where r_i is the radius of the inner ring. Under this scenario, the energy used for horizontal thrust is $E = 2 \pi r_i y p d$. Each sensor would have $(E/\kappa n)$ as initial energy, which will be converted into the initial kinetic energy giving the initial horizontal velocity, $v_{ix} = v_i$. Here, κ is the packet filling factor, defined as a ratio of the number of sensors required to fill the packet fully to the number of sensors actually filled in the packet.

$$\frac{E}{\kappa n} = p \cdot (2 \pi r_i y) \cdot d = p \cdot (2 \pi r_i y) \cdot v_i t = \frac{1}{2} m_s v_i^2$$

where m_s is the mass of each sensor.

$$\therefore p = \frac{m_s d}{4.9284 \pi r_i y h} \quad (6.4)$$

Also,

$$v_i = \frac{4 \pi r_i y p t}{m_s} \quad \text{and } v_i \propto p, \text{ as expected.}$$

The positions of all sensors would be on a circular path (initially assuming the crater surface as flat surface for simplification) with radius of $R = r + d (\approx d)$ and the positions on the surface are given by (R, θ_j) , where $j = 1, 2, \dots, n$. The final radius R depends on the travelled distance d , which in turn depends on the initial horizontal velocity v_{ih} . This initial velocity is created due to applied blast energy. Higher the blast energy, more is R and more is n for a

given line-of-sight communication distance between the sensors (d_s). Some minimum energy (E_{min}) is needed to blast the packet for achieving the required coverage of sensing region with radius R ; and for a given probing region of radius R , a minimum number of sensors is required to assure the line-of-sight wireless communication distance. This gives a lower bound on the number of sensors to be deployed. The upper bound on the number of sensors is given by the maximum permissible mass in payload and maximum energy (E_{max}) is needed for creating the blast. In the above calculations, the altitude of deployment or the drop point h is known in advance, hence the time of flight can be found.

In the present application scenario, the probing region of interest is taken about 1 km in diameter near the lunar south pole and it is actually decided after the landing site is finalized. Some of the regions near the lunar south pole do not receive sunlight and are very cold. Such regions are called permanently dark regions and there is a possibility of water ice mixed with lunar regolith in such regions. Deploying the sensors in larger area can provide the information of regolith properties in larger geographical area. The diameter of the probing region depends on such site selection and may be planned to be about 1 km. Larger area coverage is always desirable for finding the potential sites having water, but it requires more number of sensors, which in turn puts the requirements of larger size and weight of a payload, the constraints for a mission. Hence for studying the parameters, a circular region with radius R of 0.5 km is considered here, which may be achieved by few sensors with communication range of 200 m. However, it is easy to obtain the parameters for other values, as well. All remaining parameters related to topology are obtained. Figure 6.2 shows the plot of sensor fall time versus the altitude of deployment point and it is useful in calculating starting time of the network. Figure 6.3 shows initial velocity required by sensors for a given deployment height and radius of the sensing region (or distance travelled). This parameter is useful in estimating the required deployment energy to eject the sensors from a particular altitude. Figure 6.4 shows the impact velocity of sensors at the time of reaching the lunar surface, for a given altitude and initial velocity. It is necessary to know the impact velocity for designing the shielding of sensor node and it should be within the withstanding limit of material used for shielding, so that the sensor node does not break due to the impact on lunar surface. For a typical sensor having estimated weight of 200 grams, the radius of deployment ring as 1 m

with thickness as 3 cm, packet filling factor of 3 and sensors having estimated communication range as 200 m; the deployment pressure is obtained from Figure 6.5 and the deployment energy is obtained from Figure 6.6, respectively. Equation (6.6) for the number of sensors, which is derived in the following part, is used in computing the energy shown in Figure 6.6.

Figure 6.7 (a) depicts the geometry for obtaining the minimum number of sensors, Figure 6.7 (b) shows the practical positions of the sensors and Figure 6.8 shows the minimum number of sensors required for a given sensing region and for a given line-of-sight communication range of the sensors. As shown in Figure 6.7 (a), for n sensors on a circle of

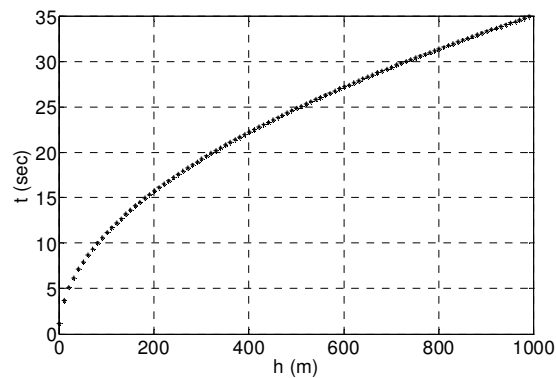


Figure 6.2: Sensor fall time vs. altitude.

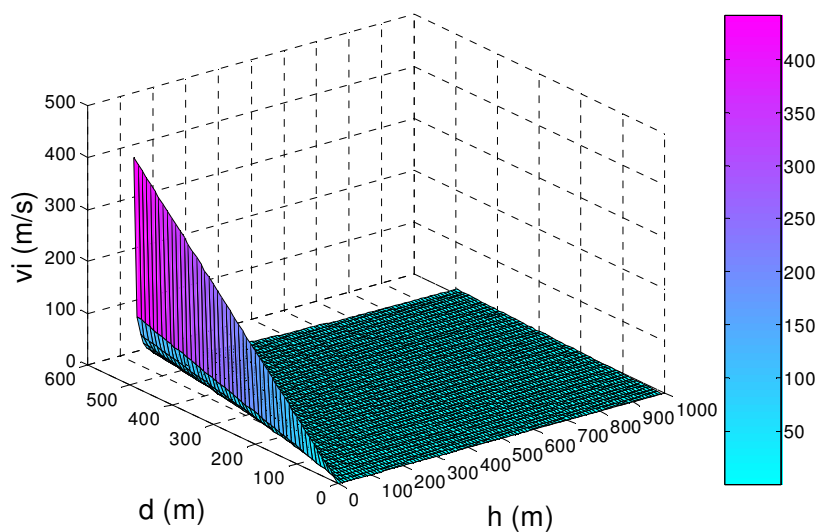


Figure 6.3: Initial velocity vs. altitude & distance to be covered.

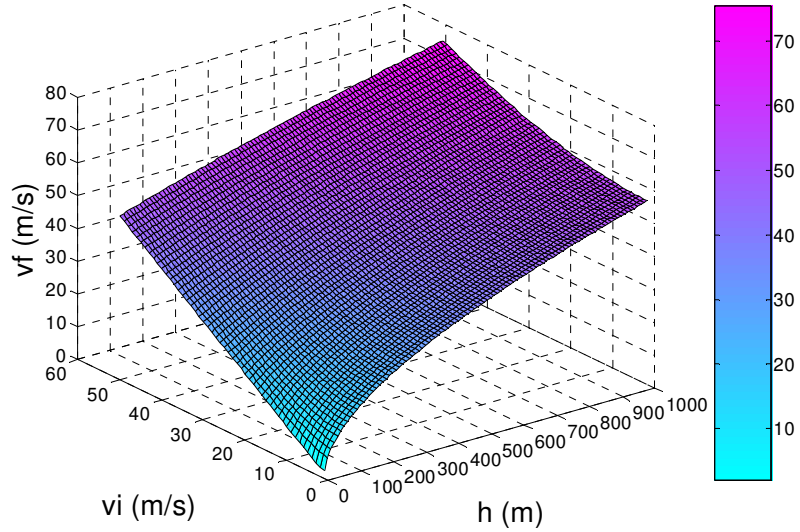


Figure 6.4: Impact velocity vs. altitude & initial thrust velocity.

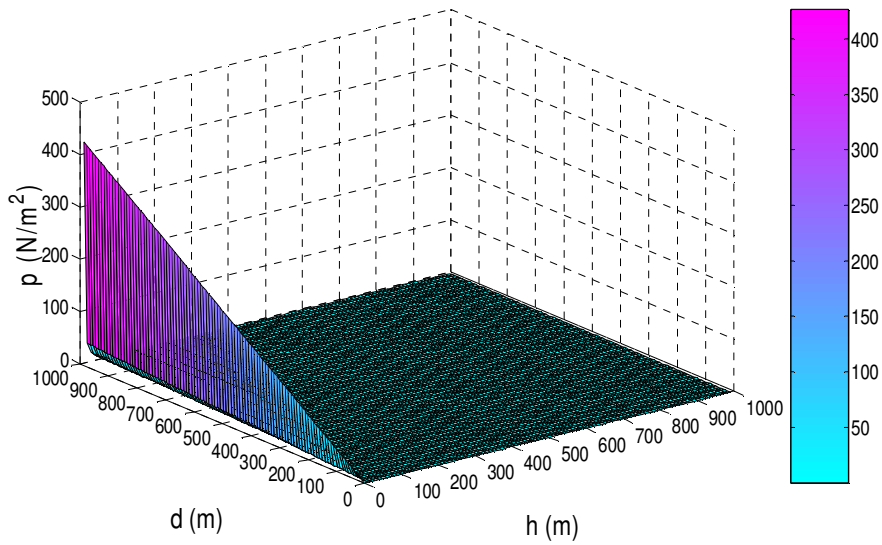


Figure 6.5: Deployment pressure vs. altitude & distance to be covered.

radius R with angle between any two consecutive sensors as θ , the Cosine law is applied in a triangle having two sides as radii of circle (R) and the third side as line-of-site communication distance (d_s) between two sensors under consideration.

$$\cos \theta = \frac{R^2 + R^2 - d_s^2}{2 \cdot R \cdot R} \quad (6.5)$$

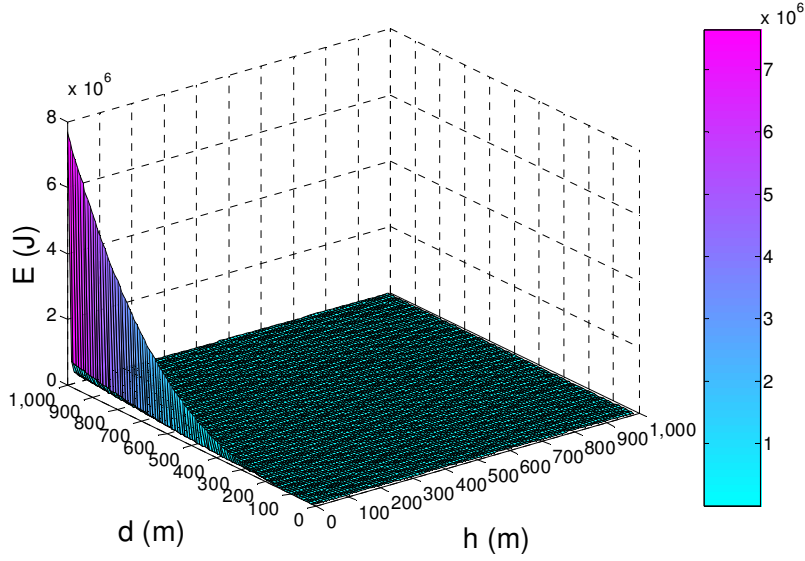


Figure 6.6: Deployment energy vs. altitude & distance to be covered.

Simplifying Equation (6.5) by taking the angular separation between two sensors as $\theta = 2\pi/n$, the following equation is obtained for the number of sensors required to probe a particular region of interest.

$$n = \frac{2\pi}{\cos^{-1}\left(1 - \frac{d_s^2}{2R^2}\right)} \quad (6.6)$$

Positions of the sensors after deployment will be

$$(R, \theta_j) = \left(R, \frac{j2\pi}{n}\right) = \left(R, j \cos^{-1}\left(1 - \frac{d_s^2}{2R^2}\right)\right)$$

where $j = 1, 2, \dots, n$ and the deployment energy required for the initial thrust is

$$E = \kappa \cdot n \cdot \frac{1}{2} \cdot m_s v_{ix}^2 = \kappa \cdot \frac{2\pi}{\cos^{-1}\left(1 - \frac{d_s^2}{2R^2}\right)} \cdot \frac{1}{2} \cdot m_s v_{ix}^2$$

$$\therefore E = \frac{\pi \kappa m_s d^2}{1.2321 h \cos^{-1}\left(1 - \frac{d_s^2}{2R^2}\right)} \quad (6.7)$$

Due to uneven surface topology inside a selected crater or on a selected site, the sensors may slide or roll over the paths and reach the final settled positions (R', θ'_i) . These final positions of sensors, if calculated using the location information, may provide the information on the local curvature of the crater, if not exactly then approximately and may also help in adding further details in terrain mapping of the crater.

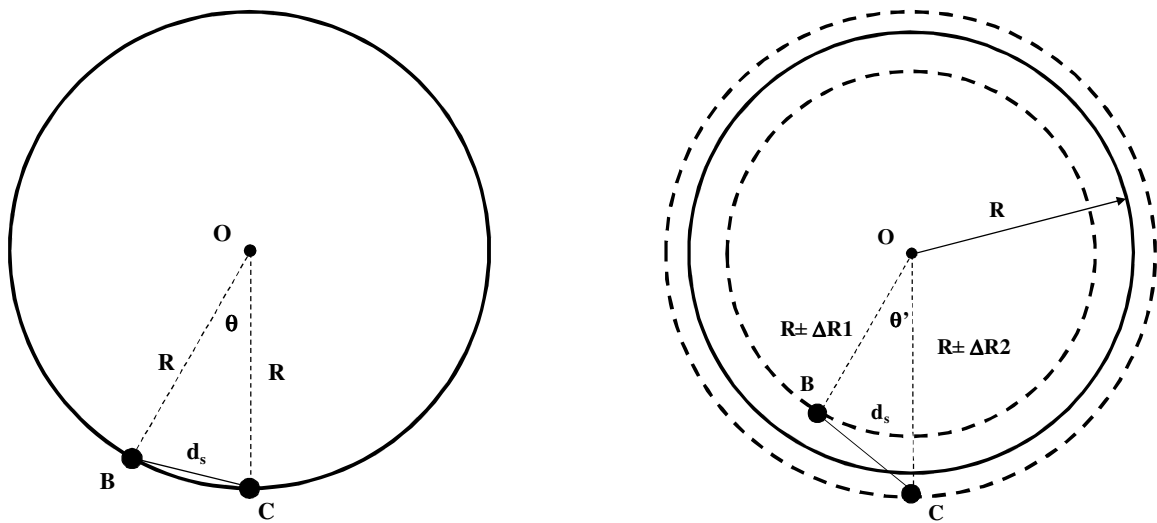


Figure 6.7: (a) Geometry for minimum number of sensors in circular topology and (b) Geometry for practical sensor positions.

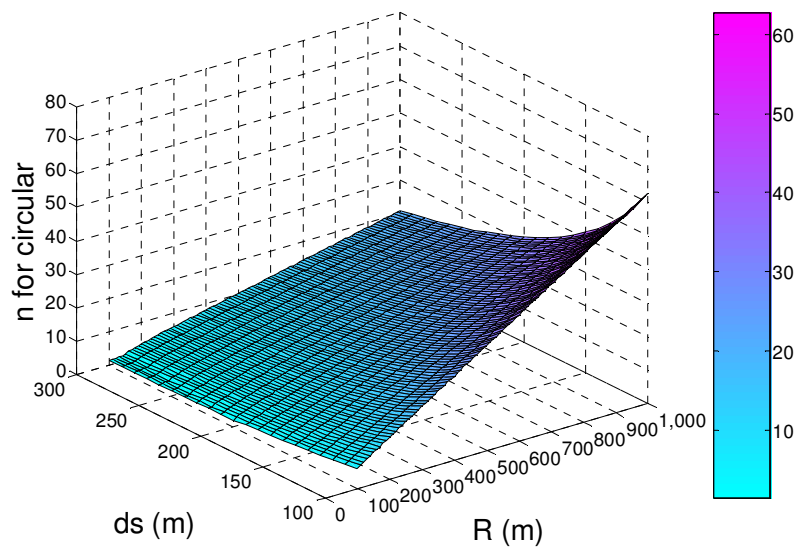


Figure 6.8: Minimum number of sensors in circular topology vs. radius of sensing zone (R) & line-of-sight communication range (d_s).

In case of the circular type deployment, the sensors are supposed to fall on the circular region. However, this may not always be the case due to uneven surface topology on the moon. This causes the sensors to either roll or slip, when they reach the lunar surface and settle at slightly different positions. In effect, they make different topology instead of a perfect circle. However, the wireless connectivity must be achieved under this practical scenario too, in order to complete the network. Suppose two adjacent sensors fall at positions of circles with radii $R \pm \Delta R_1$ and $R \pm \Delta R_2$ respectively, where ΔR_1 and ΔR_2 are changes in radii for actual positions as depicted in Figure 6.7 (b). These adjacent sensors make an angle θ' and they must have distance d_s between them to complete the network. In case, if they fall at larger distance than d_s , they can't establish the communication. If the new angle θ' is less than the old angle θ , it guarantees the wireless connectivity. Under this practical scenario, a condition on the permissible change in radii of two adjacent sensors, ΔR_1 and ΔR_2 is obtained as below.

$$\theta' \leq \theta$$

$$\therefore \text{Cos } \theta' \geq \text{Cos } \theta$$

$$\therefore \frac{(R \pm \Delta R_1)^2 + (R \pm \Delta R_2)^2 - d_s^2}{2 \cdot (R \pm \Delta R_1) \cdot (R \pm \Delta R_2)} \geq \frac{R^2 + R^2 - d_s^2}{2 \cdot R \cdot R}$$

Simplifying the above inequality, one can obtain the following condition for assured wireless connectivity in case of practical positions

$$\frac{-R \cdot \left(\sqrt{\frac{\Delta R_1}{\Delta R_2}} \mp \sqrt{\frac{\Delta R_2}{\Delta R_1}} \right)^2}{\left(\pm \frac{1}{R} \pm \frac{1}{\Delta R_1} \pm \frac{1}{\Delta R_2} \right)} \leq d_s^2 \quad (6.8)$$

The changes in radii ΔR_1 and ΔR_2 for any two neighboring sensors can be either positive or negative and only the magnitude should be taken in Equation (6.8). The rover can move near the deployment area and complete the wireless link to the orbiter or satellite, after the sensors are deployed in a circular zone.

Considering the examples for probing typical circular regions with (arbitrarily chosen) radii of 251 m and 500 m; using a circular sensor packet of vertical dimension 3 cm and inner radius 1 m, filled with sensors of 200 grams each and ejected from an altitude of 500 m for both the regions, various parameters are found and summarized in Table 6.1.

Table 6.1: Deployment parameters of typical circular schemes

| Parameter | Value for R = 251 m | Value for R = 500 m |
|--------------------|-------------------------------|---------------------------------|
| Sensor Fall Time | 24.82 sec | 24.82 sec |
| Initial Velocity | 10.07 m/sec | 20.1 m/sec |
| Impact Velocity | 41.49 m/sec | 44.99 m/sec |
| Number of Sensors | 7.67 (8*) | 15.6 (16*) |
| Total Pressure | 4.95 (5.17*) N/m ² | 20.11 (20.62*) N/m ² |
| Total Blast Energy | 233.23 (243.37*) J | 1890.77 (1939.25*) J |

*For nearest higher integer no. of sensors

6.2 Spherical Segment Deployment

The target sensing region is taken here again as a circular region (typically 1 km in diameter) and the sensors are dropped on two circular paths having radii of R_1 and R_2 with $R_1 > R_2$. To achieve the wireless connectivity and the degree of coverage under this scenario, the sensors are packed in circular ring structure as in the case of circular strategy. But now, there are two similar ring structures stacked in vertical direction so as to make an overall spherical segment structure, as shown in Figure 6.9 (a). For obtaining the mounting angle of the upper (second) ring structure from that of the first in a vertical stack inside a spherical packet, the geometry shown in Figure 6.9 (b) is used. Suppose, three sensors are to be deployed at positions B , C and D on the outer circular path having $BC = CD = d_s$, as line-of-sight wireless communication range. The fourth sensor position A is to be on the inner path such that the rectangle $ABCD$ is a rhombus. This is because, the sensor at A should also be

able to communicate to the sensors at B or D , after the network is established. Using this topology, the ratio of two radii, i.e., R_2/R_1 is found from the geometry and given as

$$\frac{R_2}{R_1} = 1 - \frac{d_s^2}{R_1^2} \quad (6.9)$$

Typically, for outer circle with 500 m radius in the considered example, the inner circle would have a radius of 420 m and the ratio of two radii would be 0.84. If the first ring structure for the outer circle is kept at 0 degree in the hemisphere, then the other ring structure is to be kept at 32.86 degree from the first on the hemispherical segment. In practice, hemispherical structure can be designed based on a real application, using the derived equation.

Now, consider that this hemispherical packet, having radius r and vertical dimension of each ring y (as it was taken for circular), is to be released from the satellite similar to the circular case. All sensors are assumed to be placed in radial directions inside the individual ring structure of hemispherical packet. The sensor packet is detached from the orbiter and its initial velocity is damped, when it attains a desired altitude from the lunar surface. The radial lines drawn from the centre of the sphere to the mid points of the vertical dimension of the ring structure are indicative of the directions of force exerted due to the pressure (p), which is released from the centre after achieving the desired altitude.

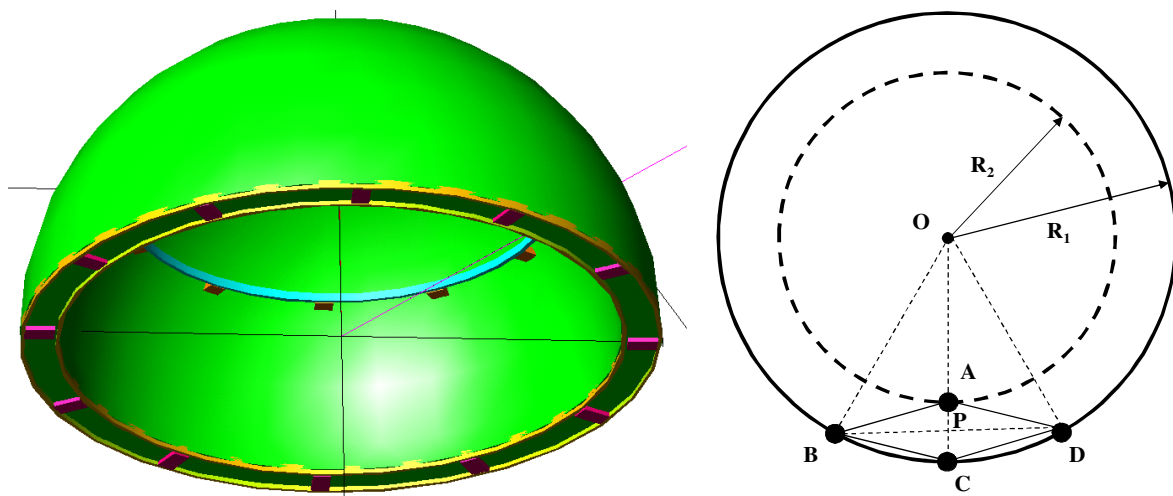


Figure 6.9: Position of sensors in (a) Spherical deployment package and (b) Sensing region.

The force on the first ring is $(2 \pi r y p)$ Newton and the sensors in this ring would travel a total horizontal distance d , due to this exerted force. However, the force on the second ring would now be $(2 \pi r y p \cos \theta)$ Newton in horizontal direction and $(2 \pi r y p \sin \theta)$ Newton in vertical direction, due to splitting of the velocity vector in two dimensions. This would cause the sensors in the second ring to travel a distance 0.84 times less than those of the first ring, in the present case. This becomes a special case of a parabolic strategy (described in the next section), in which the initial velocity is taken equal for all sensors and the launching angles can vary during the deployment; except the condition that, here, a group of sensors stacked in vertical direction are deployed together at a particular angle; while in case of parabolic strategy, only single sensor is deployed at a particular angle. The equations governing this deployment scheme are given below and merge with the circular scheme for the first ring structure; having 0 degree as position angle of ring in the hemisphere, as expected. The plots are similar to those given in the next section for the case, when launching angles are varied and therefore plots are not given here.

Time of flight of the sensor, $t_j = 0.617 (v_i \sin \theta_j - v_f \sin \phi_j)$

Distance travelled by the sensor, $d_j = 0.617 v_i \cos \theta_j \cdot (v_i \sin \theta_j - v_f \sin \phi_j)$

Depth of final sensor position from the drop point,

$$h = 0.308 \left\{ (v_i \sin \theta_j)^2 - (v_f \sin \phi_j)^2 \right\}$$

Impact angle of the sensor with horizontal, $\phi = -\tan^{-1} \left\{ \sqrt{\tan^2 \theta_j - \alpha \sec^2 \theta_j} \right\}$

Factor governing the impact angle,

$$\alpha = \frac{3.244 h}{v_i^2} \tag{6.10}$$

where $j = 1$ and 2

The trajectory parameters and the deployment energy for individual rings can be obtained using the method given for the circular, by splitting the vector in two directions. Also, the stacking of deployment rings in spherical segment can be done in reverse way, i.e., smaller ring can be mounted in the lower hemispherical part of the packet instead of mounting on the upper part, modifying the parameters slightly.

The number of sensors in such type of deployment system is given by Equation (6.6) but now for individual rings. The minimum number of sensors in this scheme is given by the addition of number of sensors in the first ring and that in the second ring as

$$n = \frac{2\pi}{\cos^{-1}\left(1 - \frac{d_s^2}{2R_1^2}\right)} + \frac{2\pi}{\cos^{-1}\left(1 - \frac{d_s^2}{2R_2^2}\right)} \quad (6.11)$$

However, $\frac{R_2}{R_1} = 1 - \frac{d_s^2}{R_1^2}$ and therefore, $R_2 = R_1 - \frac{d_s^2}{R_1}$. Substituting this value of R_2 in Equation (6.11), one can obtain the following equation for the minimum number of sensors required in this scheme.

$$n = \frac{2\pi}{\cos^{-1}\left(1 - \frac{d_s^2}{2R_1^2}\right)} + \frac{2\pi}{\cos^{-1}\left(1 - \frac{d_s^2 R_1^2}{2(R_1^2 - d_s^2)^2}\right)} \quad (6.12)$$

The number of sensors in the first and the second rings are given by the first and the second terms of Equation (6.12) or by Equation (6.6) as 16 and 14, respectively; with $R = R_1 = 500$ m and $R = R_2 = 420$ m for probing two circular zones, with assured wireless connectivity. Figure 6.10 shows the plot of minimum number of sensors in the spherical segment type strategy versus sensing zone radius and line-of-sight communication range. Once the sensors are deployed on the lunar surface, the rover can move near the deployed sensors and complete the network.

The analysis of radius sensitivity for this type is achieved on similar ground as that of the circular topology. If radius of the outer circle is taken as R_1 , the actual position of the first sensor is $R_1 + \Delta R_1$ and the actual position of the second sensor is $R_1 + \Delta R_2$; then Equation

(6.8) is a valid condition for establishing the communication between any two adjacent sensors on the outer ring with R replaced by R_1 , where ΔR_1 and ΔR_2 represent changes in radii with respect to R_1 , due to actually occupied positions by the first and the second sensor, respectively.

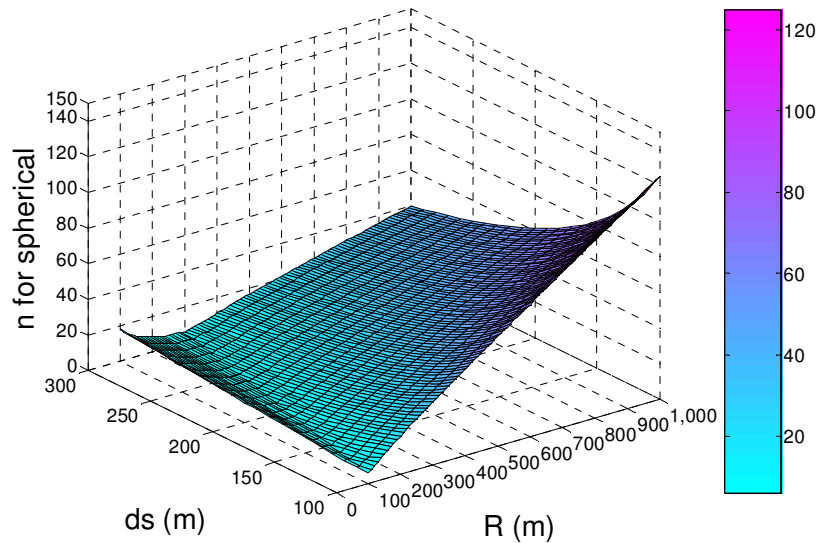


Figure 6.10: Minimum number of sensors in spherical scheme vs. radius of sensing zone (R) & line-of-sight communication range (d_s).

If the third sensor, which is supposed to be on the inner circle with radius R_2 , has actual position as $R_2 + \Delta R_3$; where ΔR_3 is the change in original radius R_2 , then it can always be referenced with respect to the radius of outer circle R_1 . Thus, $R_2 + \Delta R_3$ position may be considered as $R_1 + \Delta R_3'$; where $\Delta R_3'$ is the change in radius with respect to R_1 and now again Equation (6.8) can be applied to obtain a condition for wireless connectivity. Therefore, the derivation of sensitivity analysis is not repeated here.

6.3 Parabolic Launching

Under this deployment scheme, the lander needs to carry a mini launcher or shooter, which is either mounted on a rover or on the lander. After landing on lunar surface, the rover

should reach near the edge of a selected crater. Being at the edge of a crater, it launches sensors at different positions inside the crater by selecting various vertical launching angles with respect to horizontal axis and also by varying initial velocities of the sensors. The shooter also has the capability to vary angles in horizontal plane as well, to cover the required probing region of interest in lateral direction. However, the angle in horizontal plane does not affect the trajectory path, since the crater diameter is very large as compared to the sensing region and may be avoided in calculations. Under this scenario, the choice remains as (1) when each sensor is deployed with the same initial velocity but with varying vertical launching angles and (2) when each sensor is launched with the same vertical launching angle but with varying launching velocities. The geometry of the scheme is shown in Figure 6.11, the topology for number and positions of sensors is depicted in Figure 6.12 and the pictorial view at the crater site is shown in Figure 6.13.

Assuming the mass of each sensor as m_s and the initial launching velocity as v_s , the momentum imparted by the launcher is $m_s v_s$ and the energy needed is $\frac{1}{2} m_s v_s^2$. If there are n sensors, total initial kinetic energies for two cases respectively are

$$E_1 = \sum_{i=1}^n \frac{1}{2} m_{si} v_{si}^2 = \frac{1}{2} n m_s v_s^2 \quad (6.13-a)$$

$$E_2 = \sum_{i=1}^n \frac{1}{2} m_{si} v_{si}^2 = \frac{1}{2} m_s \sum_{i=1}^n v_{si}^2 \quad (6.13-b)$$

Since, the sensors are to be deployed at different locations; for instance, in a straight line for a particular setting of angle in horizontal plane, the launcher being at the edge of a crater would shoot each sensor with either different velocities or with different angles; effectively making the horizontal components of velocities different. In case of equal velocity launching scheme, the total energy is n times the energy required for a single sensor and some energy is also consumed in changing the launch angle. However, in case of varying velocities with the same angle, the total energy required is less than that in the first case; considering the highest starting velocity for the second case equal to the velocity of the first case. However, an exact comparison is dependent on the choice of parameters for a particular type of scheme.

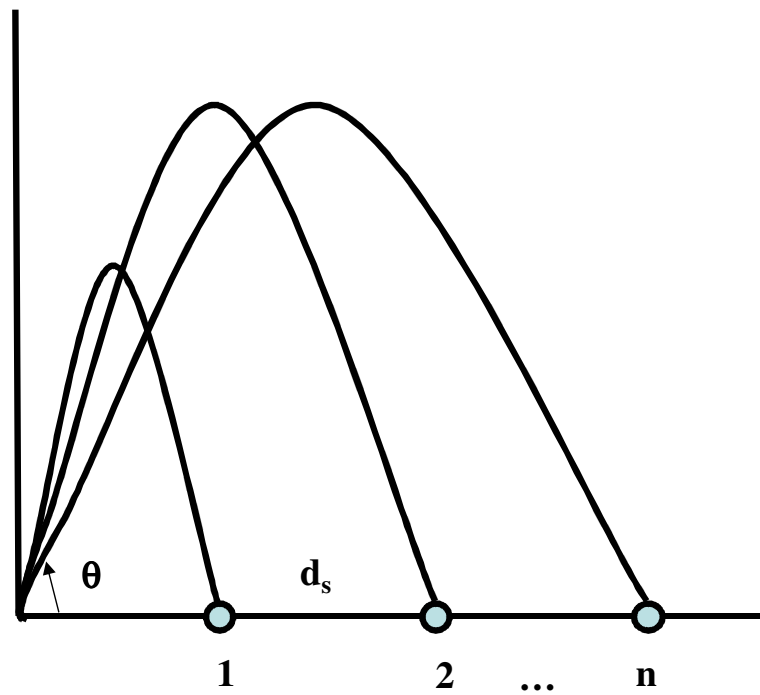


Figure 6.11: Geometry of sensor launching scheme.

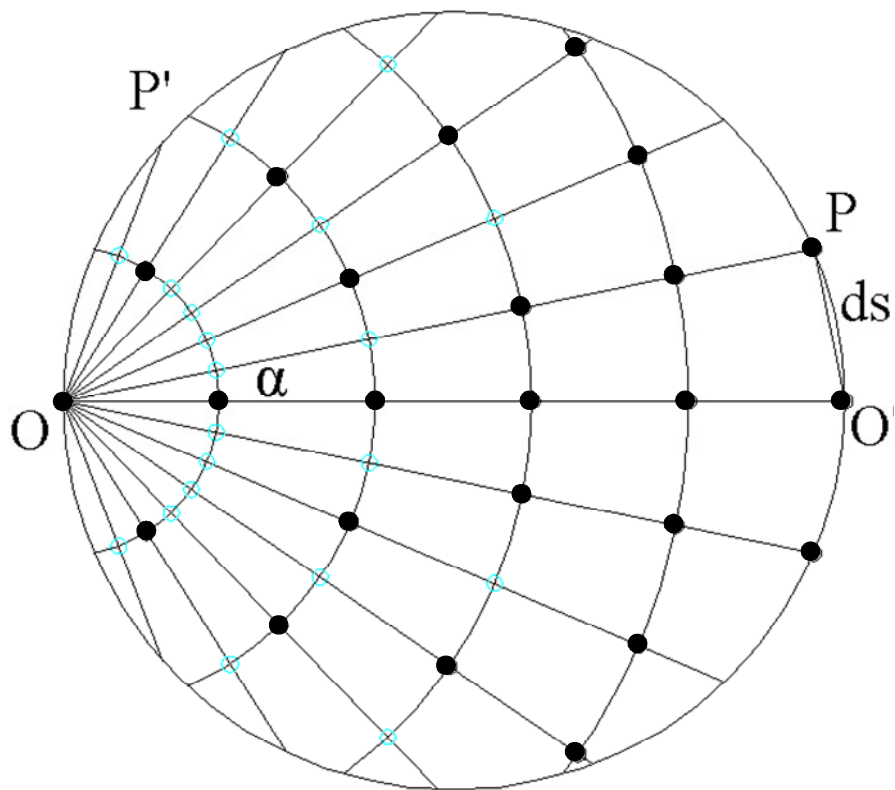


Figure 6.12: Topology showing number and positions of sensors in a typical circular sensing zone of 1 km diameter.

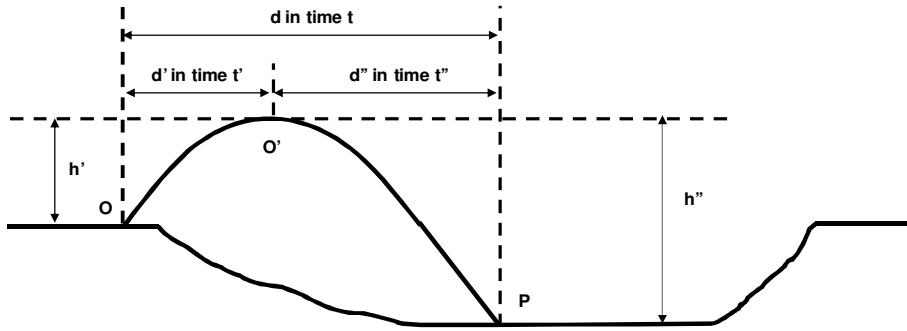


Figure 6.13: Pictorial view of scheme at crater.

For deploying n sensors, each having transmission range of d_s metre (typically 200 m) and assuming one sensor or relay is present at the edge of crater with the same transmission range d_s ; the positions of the sensors and the launching angles are found. The initial velocities are v_1, v_2, \dots, v_n and the launching angles are $\theta_1, \theta_2, \dots, \theta_n$. By using equations of motion and the concept of parabolic trajectory, following equations are obtained; where $j = 1, 2, \dots, n$. Distances of individual sensors from origin (launching place) are d_1, d_2, \dots, d_n .

Time of flight of the sensor, $t_j = 0.617 (v_i \sin \theta_j - v_f \sin \phi_j)$

Distance travelled by the sensor, $d_j = 0.617 v_i \cos \theta_j \cdot (v_i \sin \theta_j - v_f \sin \phi_j)$

Depth of crater where a sensor is deployed from the shooter,

$$h = 0.308 \left\{ (v_i \sin \theta_j)^2 - (v_f \sin \phi_j)^2 \right\}$$

Impact angle of the sensor with horizontal,

$$\phi = -\tan^{-1} \left\{ \sqrt{\tan^2 \theta_j - \alpha \sec^2 \theta_j} \right\}$$

Factor governing the impact angle,

$$\alpha = \frac{3.244 h}{v_i^2} \quad (6.14)$$

for a case when velocities are same and

Time of flight of the sensor, $t_j = 0.617 (v_{ij} \sin \theta - v_{fj} \sin \phi)$

Distance travelled by the sensor, $d_j = 0.617 v_{ij} \cos \theta \cdot (v_{ij} \sin \theta - v_{fj} \sin \phi)$

Depth of crater where a sensor is deployed from the shooter,

$$h = 0.308 \left\{ (v_{ij} \sin \theta)^2 - (v_{fj} \sin \phi)^2 \right\}$$

Impact angle of the sensor with horizontal,

$$\phi = -\tan^{-1} \left\{ \sqrt{\tan^2 \theta - \alpha \sec^2 \theta} \right\}$$

Factor governing the impact angle,

$$\alpha = \frac{3.244 h}{v_{ij}^2} \tag{6.15}$$

for a case when angles are same.

In Equation (6.14) and Equation (6.15) v_i is the launching velocity of the sensor, θ is the launching angle with horizontal, $j = 1, 2, \dots, n$ and n is the total number of sensors to be deployed. The depth of crater, the impact angle, the time of flight and the distance travelled by the sensors are shown in Figure 6.14 to Figure 6.17 for a typical parabolic launching strategy with varying launching angles and in Figure 6.18 to Figure 6.21 for a typical parabolic strategy with varying initial velocities.

For obtaining a minimum number of sensors in case of both types of parabolic strategies; it is assumed that the shooter is located at the left end of a diameter of a probing region or crater and the sensors are deployed at an equal distance of d_s in a straight line having different angles α in horizontal plane, as shown in Figure 6.12.

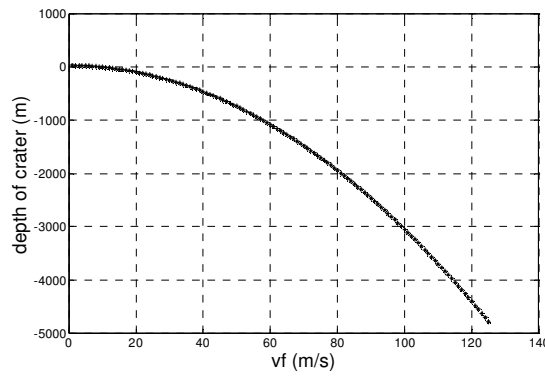


Figure 6.14: Depth of crater from the edge vs. impact velocity of sensor ($v_i = 10 \text{ m/s}$).

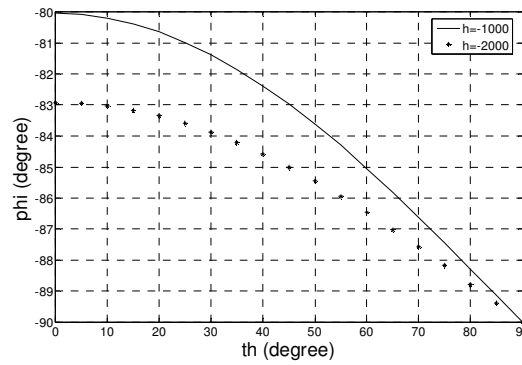


Figure 6.15: Impact angle of sensor vs. launching angle ($v_i = 10 \text{ m/s}$).

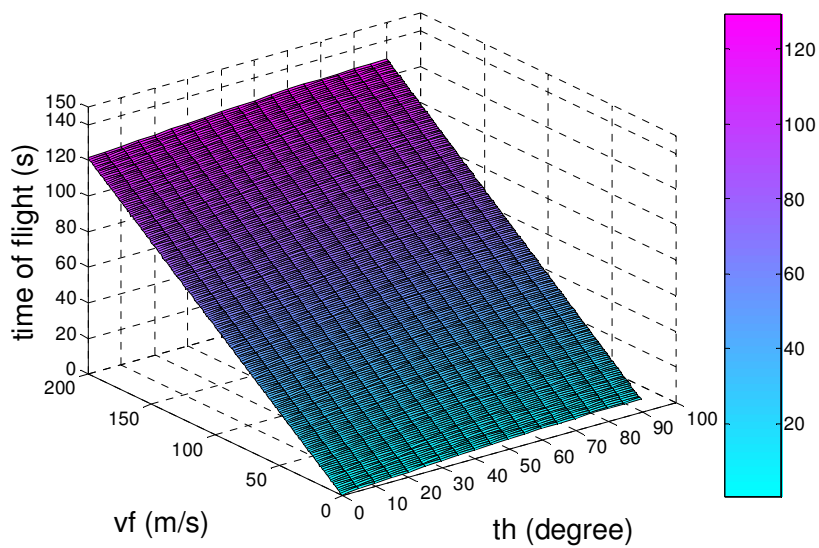


Figure 6.16: Time of flight of sensor vs. launching angle & impact velocity ($h = -1 \text{ km}, v_i = 10 \text{ m/s}$).

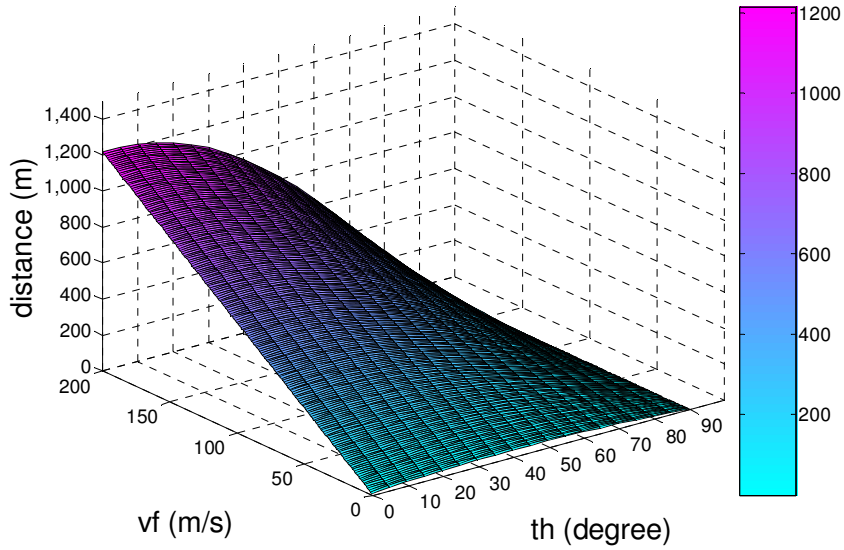


Figure 6.17: Distance of sensor vs. launching angle & impact velocity ($h = -1 \text{ km}, v_i = 10 \text{ m/s}$).

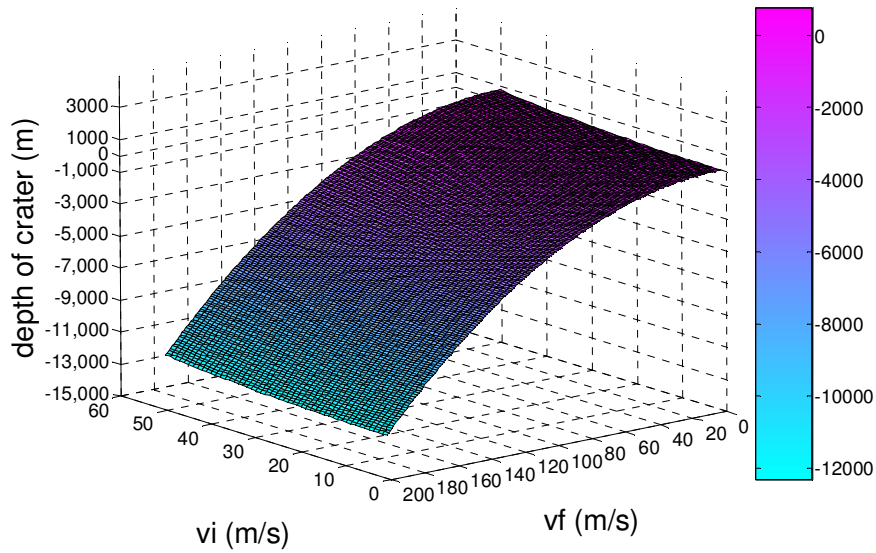


Figure 6.18: Depth of crater achieved by a sensor vs. launching & impact velocities.

Here OO' is a diameter and P is a point on semicircle. Therefore, $\angle OPO'$ is right angle and $\sin \alpha = \frac{d_s}{2R}$, where R is a radius of the sensing zone.

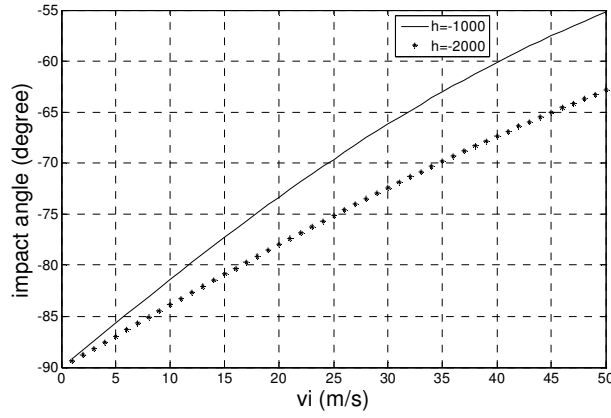


Figure 6.19: Impact angle of sensor vs. launching velocity.

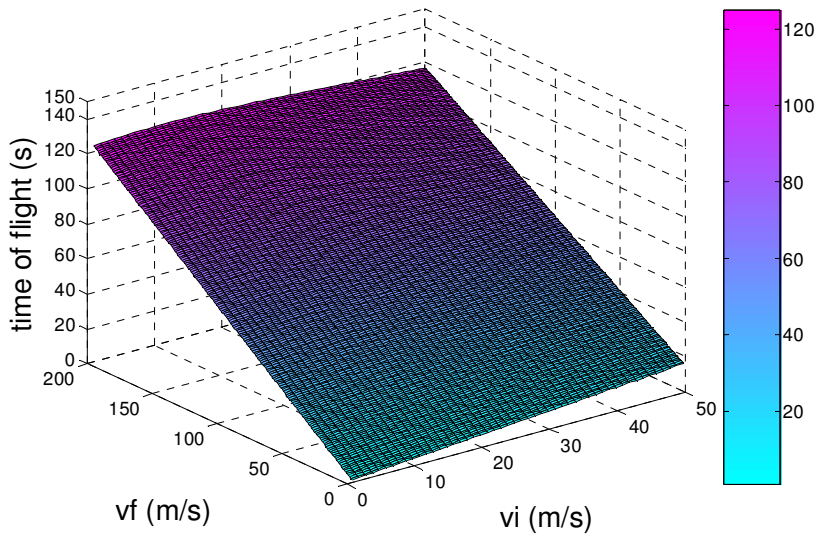


Figure 6.20: Time of flight of sensor vs. launching & impact velocities ($h = -1 \text{ km}, \theta = 30^\circ$).

Therefore, $\alpha = \text{Sin}^{-1} \left(\frac{d_s}{2R} \right)$ is the first horizontal angle for launching, from the diameter, on which the shooter is located. The remaining angles are taken as multiples of α on both sides of the diameter under consideration.

The length of the chord is, $OP = 2R \text{Cos } \alpha$. On this chord, the sensors are to be deployed at an equal distance of d_s and the number of sensors in this chord is given by the length of the chord divided by d_s . The longest chord is the diameter under consideration and

if the shortest chord is considered with minimum length d_s , then the horizontal angle of this shortest chord is found as follows.

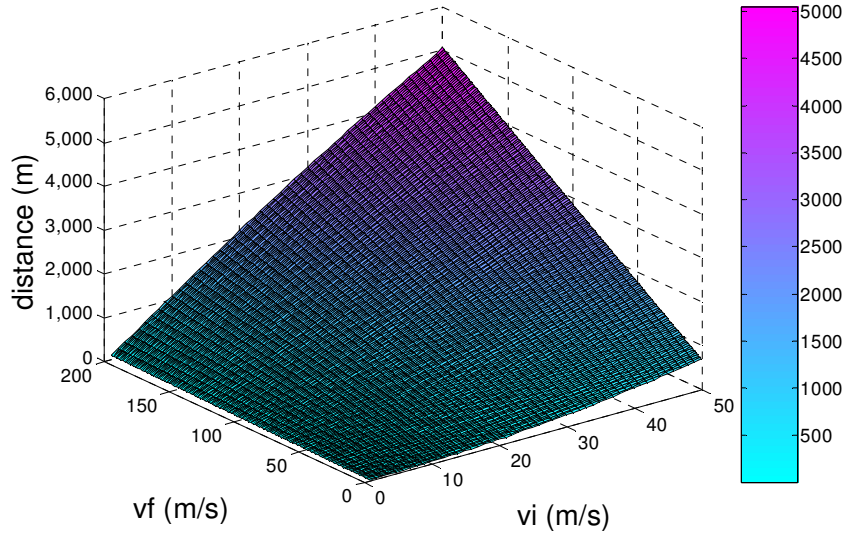


Figure 6.21: Distance covered by a sensor vs. launching & impact velocities ($h = -1 \text{ km}, \theta = 30^\circ$).

As the length of the shortest chord is d_s like OP' in Figure 6.12, the horizontal angle made by this shortest chord with the diameter is given by $\alpha' = \text{Cos}^{-1} \left(\frac{d_s}{2R} \right)$ and considering the setting of the shooter for the horizontal angles as multiples of α , i.e. $\alpha' = l \alpha$, where l is an integer, the maximum value of the integer l is given by

$$l_{max} = \text{floor} \left[\frac{\text{Cos}^{-1} \left(\frac{d_s}{2R} \right)}{\text{Sin}^{-1} \left(\frac{d_s}{2R} \right)} \right] \quad (6.16)$$

where $\text{floor}[]$ is a MATLAB [139] function which rounds the quantity in bracket towards the minus infinity and it provides an integer value of l_{max} or the quotient of ratio in equation.

The total number of sensors in parabolic scheme is given by addition of sensors in each chord in either side of the diameter.

$$\begin{aligned} \therefore n_p &= \frac{1}{d_s} \cdot \left[\sum_{l=-l_{max}}^{l_{max}} 2 R \cos (l \alpha) \right] \\ \therefore n_p &= \frac{2 R}{d_s} \cdot \sum_{l=-l_{max}}^{l_{max}} \cos \left[l \sin^{-1} \left(\frac{d_s}{2 R} \right) \right] = \text{ceil} \left[\frac{2 R}{d_s} \cdot \sum_{l=-l_{max}}^{l_{max}} \cos \left\{ l \sin^{-1} \left(\frac{d_s}{2 R} \right) \right\} \right] \end{aligned} \quad (6.17-a)$$

where $\text{ceil}[]$ is a MATLAB [139] function which rounds the quantity in bracket towards the infinity and it provides an integer number of sensors for a given probing region and wireless connectivity.

By observing the deployment topology in Figure 6.12 critically, one can find that, many sensors are redundant and the redundancy is more near the shooter. Various combinations of sensing zone and wireless connectivity have been checked and it has been found that the number of sensors, after removing the redundancy, becomes slightly more than half the number obtained from Equation (6.17-a). Therefore, in practice, following equation obtained after removing redundancy may be used for finding the minimum number of sensors.

$$\therefore n_{p_practical} \approx \text{ceil} \left[\left\{ \frac{R}{d_s} \cdot \sum_{l=-l_{max}}^{l_{max}} \cos \left(l \sin^{-1} \left(\frac{d_s}{2 R} \right) \right) \right\} + 1 \right] \quad (6.17-b)$$

The minimum number of sensors given by Equation (6.17-b) is 25 for a zone with radius of 500 m. The maximum number of sensors is decided by the weight permitted for a payload. Figure 6.22 shows the practical minimum number of sensors from Equation (6.17-b) for a given zone of radius R and sensors having communication range d_s .

In case of parabolic strategy also, there is an uncertainty in final positions of the sensors and the sensors may settle at some practical positions instead of targeted positions due to irregular surface terrain. Suppose the location of the mini launcher is selected as origin and the targeted locations of deployed sensors are given by vectors $R_{11}, R_{12}, \dots, R_{1s1}$ for the first setting of horizontal angle,

$R_{21}, R_{22}, \dots, R_{2s_2}$ for the second setting of horizontal angle, ...,

$R_{m1}, R_{m2}, \dots, R_{msm}$ for the m^{th} setting of horizontal angle;

where s_1, s_2, \dots, s_m in subscripts are the number of sensors in the 1st, 2nd, ..., m^{th} horizontal lines respectively and

$s_1 + s_2 + \dots + s_m = n_{p_practical}$ as given by Equation (6.17-b).

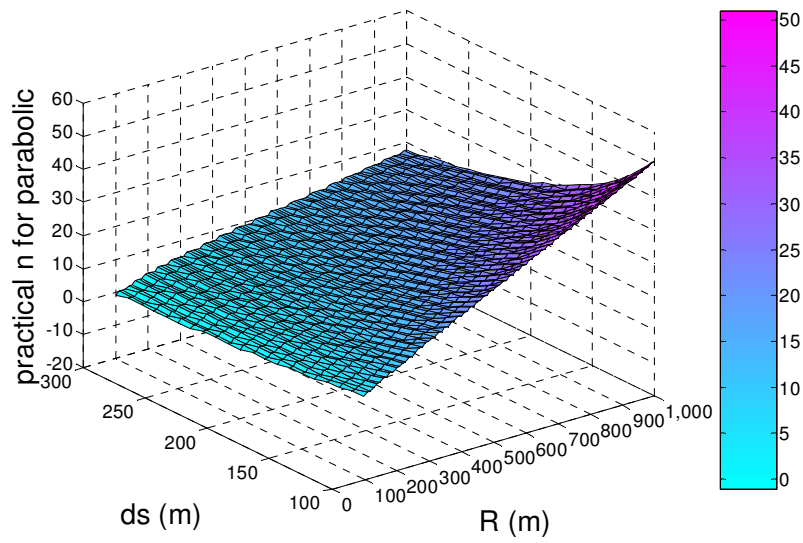


Figure 6.22: Minimum number of sensors in parabolic type scheme vs. radius of sensing zone (R) & wireless connectivity range (d_s).

Suppose, the sensors attain actual positions as

$R_{11} \pm \Delta_{11}, R_{12} \pm \Delta_{12}, \dots, R_{1s_1} \pm \Delta_{1s_1}$ for the first setting of horizontal angle,

$R_{21} \pm \Delta_{21}, R_{22} \pm \Delta_{22}, \dots, R_{2s_2} \pm \Delta_{2s_2}$ for the second setting of horizontal angle, ...,

$R_{m1} \pm \Delta_{m1}, R_{m2} \pm \Delta_{m2}, \dots, R_{msm} \pm \Delta_{msm}$ for the m^{th} setting of horizontal angle;

where Δ in subscripts indicate differences between the targeted and the actual positions of respective sensors.

For any horizontal deployment line, the maximum permissible difference between practical and ideal positions for any two adjacent sensors must be less than or equal to the communication range d_s and for any two nearby sensors on two adjacent lines, the permissible change is given by Equation (6.8) after using respective parameters.

6.4 Deployment Simulation Consideration

The simulation related to the sensor deployment in a given terrain may be carried out to know the effects of terrain on various factors like the number of sensors, coverage, routing, positions of sensors after deployment etc. For lunar application, the selection of landing site for sensor deployment needs careful considerations on many aspects like the possibility of water bearing region, availability of sunlight to charge the rover battery, visibility of the site from the earth for communication and comparatively smooth terrain for easy rover movement. It is known that for given latitude and longitude, the DEM of the site provides the information about the height. One may carry out the terrain based simulation for sensor deployment to know where the sensors would settle on the lunar surface after they are dropped. The sensors may either roll or slide after they encounter the surface first time and settle at the final positions. Such deployment simulation involves very complex computations and stringent requirements. The sensor dimensions, the mass, the friction coefficient between the sensor node and the lunar surface, the DEM data etc. are needed as inputs in the simulation. The sensor dimensions are of the order of few cubic centimeters. The deployment simulation requires very fine resolution of the DEM data of the order of the dimensions of the sensor to consider the effects of local undulations in the terrain. The simulation may be carried out for any of the three suggested deployment schemes. The results of such simulations provide insight into the finally settled positions of the sensors. Using the final positions of the sensors, one can obtain the idea of the network topology and check if the wireless connectivity would be established using Equation (6.8). Thus, such simulation can be useful for finding the location information of the sensors and predicting the network topology.

6.5 Discussions

It is always desirable to reduce the number of sensors and increase the geographical coverage in any wireless sensor network, either on the earth or on any other planet. This

necessitates minimization of the number of sensors for deployment plan under consideration, with maximum connectivity between the sensors. The minimum number of sensors offers minimum weight and size for a given sensing region and also reduced energy for carrying the sensor packet. Any increase in geographical coverage demands more number of sensors, which in turn consumes more mass, size and power. For any WSN, there always remains a tradeoff between the coverage and the number of sensors to be deployed. Thus, the number of sensors should be judiciously selected in the design of WSN. These goals have been achieved for all the three types of deployment schemes suggested for WSN on lunar surface.

In case of circular strategy, when sensors reach crater surface, they can form a circular topology. However, if any of the sensor node fails on impact, then the connectivity of network would be lost in that particular part of the network. Possible solution to this problem is to double the number of sensors in a ring, so that even if a few sensors fail, the remaining may be able to form the network by a networking protocol. This option increases the redundancy by 100 %.

In case of spherical segment deployment, the loss of connectivity problem on impact is solved to a certain extent, as the sensors are deployed in a grid fashion due to double ring structure and there are alternative routes for them to complete the communication network. To add further possibility of establishing a network, the number of sensors can be doubled in each ring, which increases the redundancy by 100 %.

In parabolic deployment scheme, one can achieve enough radio coverage as there is a liberty to deploy a sensor in desired direction by moving the mini launcher in that particular direction. Moreover, a separate release of sensor packet from the orbiter is not required, since the rover must have settled and become ready for wireless operation before deploying the sensor nodes. Increase in redundancy is suggested here too, to increase the probability of network establishment. In such a scheme, if the lander (which actually carries the rover with sensors and launcher) is landed at a place near one of the interested lunar craters, then the shooter can be mounted on the lander itself; instead of putting on the rover. This reduces burden on the rover to carry the sensors and the launcher to the edge of a selected crater.

Simplification regarding comparison of all deployment systems is achieved by comparing the deployment cost. The deployment costs of all topologies depend on the cost of sensor, the number of sensors for a common sensing region and the cost of deployment packet (for circular and spherical segment) or mini launcher (for parabolic). The deployment costs of all the three schemes are given by following equations.

$$C_c = n_c \cdot C_s + C_{c_packet} \quad (6.18)$$

$$C_{sp} = n_s \cdot C_s + C_{sp_packet} \quad (6.19)$$

$$C_p = n_{p_practical} \cdot C_s + C_{p_launcher} \quad (6.20)$$

where C_s is the cost of the sensor;

C_c , C_{sp} and C_p are the deployment costs of circular, spherical and parabolic schemes, respectively;

n_c , n_s and $n_{p_practical}$ are the number of sensors in circular, spherical and parabolic schemes, respectively;

C_{c_packet} , C_{sp_packet} and $C_{p_launcher}$ are the packet cost of circular scheme, the packet cost of spherical scheme and the cost of mini launcher in parabolic scheme, respectively.

Typically, the packet cost of circular, the packet cost of spherical and the cost of mini launcher in Equation (6.18) to Equation (6.20) are constant and almost equivalent except for some marginal differences, which indicate that the deployment cost is directly proportional to the number of sensors in each case. Considering a common circular sensing zone of 1 km in diameter and neglecting the constant components in Equation (6.18) to Equation (6.20), the deployment costs in all the three cases are compared in Table 6.2. Both, circular and spherical type deployments can only be adopted if the rover has reached the lunar surface, has already settled and has become ready for its wireless operation (needed to complete the communication link to the orbiter). Otherwise, the sensors deployed by any of these two methods can become ineffective due to short battery life time, before the rover has established

and therefore become of no use. This necessitates the release of sensor packet from the orbiter at a time or after the time, when rover is ready for its wireless operation.

The parabolic deployment scheme suffers from the disadvantage that either the lander or the rover needs more energy to carry the deployment mechanism and the sensors. Also, it is seen that the deployment cost in case of circular scheme is the lowest and that in case of spherical scheme is the highest, while that for the parabolic scheme is moderate. In planetary applications, where weight and power are not serious issues, the parabolic scheme seems a better choice as compared to circular or spherical segment schemes.

Table 6.2: Comparison of deployment costs of three schemes

| Scheme | No. of Sensors (for R = 500 m) | Deployment Cost |
|---------------|---|----------------------------|
| Circular | 16 | $16 C_s$ |
| Spherical | 30 | $30 C_s$ |
| Parabolic | 25 | $25 C_s$ |

6.6 Summary and Conclusion

The sensor deployment scheme on the moon is quite different than that used for terrestrial sensor networks on the earth. Three deployment schemes have been suggested for lunar application and results provide good understanding and more insight into conditions of various trajectory parameters related to different proposals. The minimum numbers of sensors are derived based on optimization between the maximum area coverage and the wireless connectivity, while the deployment costs of all systems provide quick information about the selection of the scheme for a particular application. The condition on permissible tolerances in desired dropping positions of the sensors has been derived. The condition addresses the practical difficulty in achieving the exact locations of the sensors and provides information about the limits of tolerances with assured wireless connectivity.

Chapter 7

Conclusion and Future Work

The Wireless Sensor Network (WSN) has been in research phase for about two decades and its applications are increasingly becoming popular in diversified fields including commercial, military, health, environment, agriculture, space and planetary science. Different applications need to address research issues associated with them in different ways, depending on considerations like hardware design, communication channel modeling, low power protocols, media sharing issues, adaptive networking and the shortest path routing. One of the applications of WSN is in the study of planetary surface science. Since, space missions involve huge cost; it is evocative to predict performance of the system ahead of time. Challenges involved in WSN for in-situ exploration of water ice on the moon have been addressed in this thesis. The research issues are summarized as follows.

Research Issues

- Communication scenario on the moon is different than that on the earth and existing wireless propagation models for the earth based systems cannot directly be applied to the moon.

- Multipath signals can be present at the receiver due to irregular terrain on the moon. These multipath signals pose limitation on the transmission bit rate for a given hardware.
- Existing water ice sensors based on reflectometry are not appropriate for lunar and other planetary applications due to more space requirement, need of extra energy for probe insertion and other constraints.
- Suitable sensor deployment scheme is to be envisaged for sensor positioning on the lunar surface.

All these research issues have been addressed in this thesis with all necessary aspects and conclusion derived from the results are encapsulated as follows.

Conclusion

- ❖ Existing RF models for the earth cannot directly be applied to lunar WSN. Free space loss is a basic loss on the moon. Reflections can occur from terrain irregularities causing multipath at the receiver.
- ❖ RF modeling results show percentage coverage patterns for a given bit rate of the link on lunar surface, based on actual Digital Elevation Model data of the lunar sites.
- ❖ RF modeling results suggest: (a) use of available transceivers as far as receiver sensitivity is concerned, (b) better sensor deployment sites on the moon, based on terrain or; area coverage pattern for a given landing site on the moon and (c) rover paths to assure wireless connectivity between the node and the cluster head on the rover.
- ❖ Analysis of lunar multipath environment can be done and channel behavior can be visualized by the suggested method for prediction of multipath parameters, using the proposed LWM. Lunar PDP shows exponential decay, similar to the outdoor model on the earth.
- ❖ Lunar multipath analysis results are useful to predict BER and PER of a given wireless link on lunar surface. Typically, the BER reaches 10^{-4} and the minimum suggested SNR at the receiver is 15 dB.

- ❖ The developed Wireless Impedance Sensor Node (WISN) is compact enough to be considered for space and planetary surface science applications, with very small electrode length, of the order of few mm.
- ❖ Real part of relative permittivity of dry JSC-1A is found around 3 and real part of conductivity of dry JSC-1A is found of the order of 10^{-8} S/m using the WISN.
- ❖ The real part of permittivity of Milli-Q water reaches 80 and crossover point between real and imaginary parts of permittivity is reproducible by the WISN.
- ❖ Results of water and ice, obtained by the WISN, agree with those given in the literature and promise that the WISN can be used for future planetary applications.
- ❖ Sensor deployment scheme on the moon is quite different than that used for terrestrial sensor networks. Deployment results provide good understanding and more insight into conditions of various parameters related to different proposals.
- ❖ The condition on permissible tolerances in the desired dropping positions of the sensors addresses the practical difficulty in achieving the exact locations of the sensors with assured wireless connectivity.

Future Work

Since, lunar WSN is a big project in itself; it involves many other challenges like localization, power aware protocols and long battery life. The multipath problem on the moon may be overcome by designing space-time coding system, with additional resources included in the node. Another solution to the multipath problem on lunar surface is to carry out time-reversed signal processing for a given positioning of the sensors. The impedance sensor may be used for other application on planetary surface like characterization of planetary dust using a dust collection surface. The impedance sensor may also be used for detection of seismic activity by converting seismic signal into impedance. The impedance sensor may be useful in characterizing various types of soils, sedimentary rocks and similar minerals. The impedance sensor may also be useful for detection of life in astrobiology. Accordingly, there is a vast scope of future work and many research opportunities are open in this domain.

References

- [1] Paul D. Spudis, "Introduction to the Moon", *Moon 101-A Course in Lunar Science for non-specialists*, NASA Johnson Space Centre, Online, 20th September, 2010. Available: <http://www.spudislunarresources.com/moon101.htm>.
- [2] Online, 20th September, 2010. Available: <http://en.wikipedia.org/wiki/Moon>.
- [3] Online, 12th April 2011. Available: http://www.lunarpedia.org/index.php?title=Lunar_Temperature.
- [4] P. Spudis, "Ice on the Moon", *The Space Review*, November 6, 2006.
- [5] C. M. Pieters, J. N. Goswami, R. N. Clark, M. Annadurai, J. Boardman, B. Buratti, J. P. Combe, M. D. Dyar, R. Green, J. W. Head, C. Hibbitts, M. Hicks, P. Isaacson, R. Klima, G. Kramer, S. Kumar, E. Livo, S. Lundeen, E. Malaret, T. McCord, J. Mustard, J. Nettles, N. Petro, C. Runyon, M. Staid, J. Sunshine, L. A. Taylor, S. Tompkins and P. Varanasi, "Character and Spatial Distribution of OH/H₂O on the Surface of the Moon Seen by M³ on Chandrayaan-1", *Science*, 326, 2009, p. 568.
- [6] Christopher R. Webster, Gregory J. Flesch, Kamjou Mansour, Robert Haberle and Jill Bauman, "Mars laser hygrometer", *Applied Optics*, Vol. 43, No. 22, 2004, pp. 4436-4445.
- [7] Paul Spudis, Stewart Nozette, Ben Bussey, Keith Raney, Helene Winters, Christopher L. Lichtenberg, William Marinelli, Jason C. Crusan and Michele M. Gates, "Mini-SAR: an imaging radar experiment for the Chandrayaan-1 mission to the Moon", *Current Science*, Vol. 96, No. 4, 2009, pp. 533-539.

- [8] Online, 11th April 2011. Available: http://en.wikipedia.org/wiki/OSI_model.
- [9] Online, 20th September 2010. Available: <http://www.decagon.com/products/sensors/soil-moisture-sensors/5te-soil-moisture-temperature-and-ec/>.
- [10] Bhavneet Sidhu, Hardeep Singh and Amit Chhabra, "Emerging Wireless Standards - WiFi, ZigBee and WiMAX", *World Academy of Science, Engineering and Technology*, Issue 25, January 2007, pp. 308-313. Online, 25th September 2010. Available: <http://www.waset.org/journals/waset/v25/v25-58.pdf>
- [11] Online, 25th September 2010. Available: http://en.wikipedia.org/wiki/IEEE_802.11
- [12] Simon Liam Willis, "Investigation into long range wireless sensor networks", Ph. D. Thesis, James Cook University, Townsville, Australia, December 2007.
- [13] S. Xu and T. Saadawi, "Does the IEEE 802.11 MAC protocol work well in multihop wireless ad hoc networks?", *IEEE Communications Magazine*, Vol. 39, Issue 6, 2001, pp. 130-137.
- [14] Hung-Yun Hsieh and R. Sivakumar, "IEEE 802.11 over multi-hop wireless networks: problems and new perspectives", *Proceedings of IEEE 56th Vehicular Technology Conference*, Vol. 2, 2002, pp. 748-752.
- [15] Online, 25th September 2010. Available: <http://en.wikipedia.org/wiki/Bluetooth>.
- [16] Y. Liu, M. J. Lee and T. N. Saadawi, "On-demand formation of Bluetooth scatternet", *Proceedings of Military Communications Conference*, Vol. 2, 2002, pp. 1069-1074.
- [17] Y. Liu, M. J. Lee and T. N. Saadawi, "A Bluetooth scatternet route structure for multihop ad-hoc networks", *IEEE Journal on Selected Areas in Communications*, Vol. 21, Issue 2, 2003, pp. 229-239.
- [18] Online, 11th April 2011. Available: http://en.wikipedia.org/wiki/IEEE_802.15.4-2006.
- [19] Online, 1st October 2010. Available: <http://focus.ti.com/lit/ds/symlink/cc2420.pdf>.
- [20] Online, 1st October 2010. Available: <http://www.zigbee.org/>.
- [21] Online, 1st October 2010. Available: www.media.mit.edu/resenv/classes/MAS961/readings/802-15-4_Tutorial.ppt.
- [22] Online, 6th October 2010. Available: <http://www.wimaxforum.org/>.
- [23] Online, 6th October 2010. Available: <http://en.wikipedia.org/wiki/WiMAX>.
- [24] Online, 6th October 2010. Available:

- <http://www.breezecom.com/index.php/en/technology/standards/wimax>.
- [25] Caroline Gabriel, “WiMAX: The Critical Wireless Standard”. Online, 6th October 2010. Available: http://www.eyeforwireless.com/wimax_report.pdf.
- [26] Wonil Roh and Vladimir Yanover, “Introduction to WiMAX Technology”, in *WiMAX Evolution: Emerging Technologies and Applications*, John Wiley & Sons, Ltd, 2009.
- [27] Online, 6th October 2010. Available: <http://www.alvarion.com/index.php/en/technology/standards/lte>.
- [28] Online, 6th October 2010. Available: http://en.wikipedia.org/wiki/3GPP_Long_Term_Evolution.
- [29] Bruno Clerckx, Angel Lozano, Stefania Sesia, Cornelius van Rensburg and Constantinos B. Papadias, “3PPG LTE and LTE Advanced”, Special Issue of *EURASIP Journal on Wireless Communications and Networking*, Hindawi Publishing Corporation, 2009.
- [30] Allen H. Kupetz and K. Terrell Brown, “4G - A Look into the Future of Wireless Communications”, *Rollins Business Journal*, Jan-Mar 2004, pp. 1-5.
- [31] Jean-Paul Rissen and Robert Soni, “The evolution to 4G systems”, 4G Wireless Technologies-Special Issue of *Bell Labs Technical Journal*, Vol. 13, Issue 4, Winter 2009, pp. 1-5.
- [32] Online, 6th October 2010. Available: <http://en.wikipedia.org/wiki/4G>.
- [33] Online, 6th October 2010. Available: <http://www.alvarion.com/index.php/en/technology/standards/4g>.
- [34] Ian F. Akyildiz, Weilian Su, Yogesh Sankarasubramaniam and Erdal Cayirci, “A Survey on Sensor Networks”, *IEEE Communications Magazine*, Vol. 40, No. 8, 2002, pp. 102-114.
- [35] Online, 16th November 2010. Available: <http://www.princeton.edu/~mrm/zebranet.html>.
- [36] J. L. Hill, “System Architecture for Wireless Sensor Networks”, Ph. D. Thesis, University of California, Berkeley, 2003.
- [37] Y. Xu, J. Heidemann and D. Estrin, “Geography-informed energy conservation for ad hoc routing”, *Proceedings of 7th Annual International Conference on Mobile Computing and Networking*, New York, 2001, pp. 70-84.

- [38] M. D. Yarvis, W. S. Conner, L. Krishnamurthy, J. Chhabra, B. Elliott and A. Mainwaring, "Real-world experiences with an interactive ad hoc sensor network", *Proceedings of the 2002 International Conference on Parallel Processing Workshops*, Washington, 2002, pp. 143-151.
- [39] Chris Townsend and Steven Arms, "Wireless Sensor Networks: Principles and Applications", MicroStrain, Incorporation. Online, 4th February 2011. Available: <http://microstrain.com/white/Wilson-chapter-22.pdf>.
- [40] Jorge Tavares, Fernando J. Velez and Joao M. Ferro, "Application of Wireless Sensor Networks to Automobiles", *Measurement Science Review*, Vol. 8, Sec. 3, No. 3, 2008, pp. 65-70.
- [41] P. L. Rice, A. G. Longley, K. A. Norton and A. P. Barsis, "Transmission loss predictions for tropospheric communication circuits", Technical Note 101, National Bureau of Standards, 1967.
- [42] G. Hufford, "The ITS irregular terrain model version 1.2.2-The algorithm". Online, 5th February 2011. Available: http://flattop.its.blrdoc.gov/itm/itm_alg.pdf.
- [43] H. Wong, "Field strength prediction in irregular terrain-the PTP model", 2002. Online, 5th February 2011. Available: <http://www.fcc.gov/oet/fm/ptp/report.pdf>.
- [44] A. Neskovic, N. Neskovic and G. Paunovic, "Modern approaches in modeling of mobile radio systems propagation environment", *IEEE Communications Surveys*, Vol. 3, No. 3, 2000, pp. 1-12.
- [45] S. L. Willis and C. J. Kikkert, "Radio propagation model for long-range ad hoc wireless sensor network", *International Conference on Wireless Networks, Communications and Mobile Computing*, Vol. 1, Issue 13-16, 2005, pp. 826-832.
- [46] Microwave Office, Online, 5th February 2011. Available: <http://web.awrcorp.com/products/mwoffice/>.
- [47] Vishwanath Chukkala and Phillip De Leon, "Simulation and analysis of the multipath environment of Mars", *Proceedings of IEEE Aerospace Conference*, Big Sky, Montana, 2005, pp. 1678-1683.
- [48] Theodore S. Rappaport, *Wireless Communications, principles and practice*, 2nd Edition, Pearson, 2009.

- [49] Justin C. I. Chuang, “The effects of time delay spread on portable radio communications channels with digital modulation”, *IEEE Journal on Selected Areas in Communications*, Vol. SAC-5, No. 5, June 1987, pp. 879-889.
- [50] Jeff Plescia, “The Lunar Surface”, *Moon 101-A Course in Lunar Science for non-specialists*, NASA Johnson Space Center, 2008. Online, 1st February 2011. Available: http://www.spudislunarresources.com/moon101/moon_101_surface.pdf.
- [51] Ruth Globus, “Impact upon lunar atmosphere”, Chapter 5, Appendix J in *Space Settlements: A Design Study*, Richard D. Johnson and Charles Holbrow, Ed., NASA, 1977. Online, 6th January 2011. Available: <http://settlement.arc.nasa.gov/75SummerStudy/5appendJ.html>.
- [52] Paul Lucey, Randy L. Korotev, Jeffrey J. Gillis, Larry A. Taylor, David Lawrence, Bruce A. Campbell, Rick Elphic, Bill Feldman, Lon L. Hood, Donald Hunten, Michael Mendillo, Sarah Noble, James J. Papike, Robert C. Reedy, Stefanie Lawson, Tom Prettyman, Olivier Gasnault and Sylvestre Maurice, “Understanding the lunar surface and space-moon interactions”, *Reviews in Mineralogy and Geochemistry*, Vol. 60, No. 1, 2006, pp. 83-219.
- [53] Arlin P. S. Crotts, “Lunar outgassing, transient phenomena and the return to the moon. I. EXISTING DATA”, *The Astrophysical Journal*, Vol. 687, No. 1, 2008, pp. 692-705.
- [54] R. Sridharan, S.M. Ahmed, Tirtha Pratim Das, P. Sreelatha, P. Pradeepkumar, Neha Naik and Gogulapati Supriya, “‘Direct’ evidence for water (H₂O) in the sunlit lunar ambience from CHACE on MIP of Chandrayaan I”, *Planetary and Space Science*, Vol. 58, 2010, pp. 947-950.
- [55] S. Alan Stern, “The lunar atmosphere: History, status, current problems, and context”, *Reviews of Geophysics*, Vol. 37, No. 4, 1999, pp. 453-491.
- [56] Wendell Mendell, “The lunar environment”, *Moon 101-A Course in Lunar Science for non-specialists*, NASA Johnson Space Center, 2008. Online, 1st February 2011. Available: http://www.spudislunarresources.com/moon101/moon_101_enviro.pdf.
- [57] Online, 2nd February 2011. Available: <http://maia.usno.navy.mil/NSFA/CBE.html>.
- [58] Online, 2nd February 2011. Available: <http://en.wikipedia.org/wiki/Sunlight>.
- [59] Online, 2nd February 2011. Available: [http://en.wikipedia.org/wiki/Lunar_distance_\(astronomy\)](http://en.wikipedia.org/wiki/Lunar_distance_(astronomy)).

- [60] T. J. Stubbs, R. R. Vondrak and W. M. Farrell, "A dynamic fountain model for lunar dust", *Advances in Space Research*, Vol. 37, Issue 1, 2006, pp. 59-66.
- [61] Online, 7th February 2011. Available: <http://en.wikipedia.org/wiki/Sun>.
- [62] Eltek Limited, Online, 7th February 2011. Available: http://www.eltekdataloggers.co.uk/sensors_light.shtml.
- [63] Pico Technology, Online, 7th February 2011. Available: <http://www.picotech.com/applications/pt100.html>.
- [64] Online, 7th February 2011. Available: <http://www.megatron.co.il/Thermocouple.html>.
- [65] Online, 7th February 2011. Available: <http://en.wikipedia.org/wiki/Thermocouple>.
- [66] Online, 7th February 2011. Available: <http://en.wikipedia.org/wiki/Permittivity>.
- [67] F. Batalioto, A. R. Duarte, G. Barbero and A. M. F. Neto, "Dielectric dispersion of water in the frequency range from 10 mHz to 30 MHz", *Journal of Physical Chemistry B*, Vol. 114, Issue 10, 2010, pp. 3467-3471.
- [68] F. Grasso, F. Musumeci and A. Triglia, "Impedance Spectroscopy of Pure Water in the 0.01 Hz to 100 kHz Range", *IL Nuovo Cimento D*, Vol.12, No. 8, 1990, pp. 1117-1130.
- [69] Suresh Seshadri, Keith B. Chin, Martin G. Buehler and Robert C. Anderson, "Using electrical impedance spectroscopy to detect water in planetary regoliths", *Astrobiology*, Vol. 8, No. 4, 2008, pp. 781-792.
- [70] M. G. Buehler, H. Bostic, K. B. Chin, T. McCann, D. Keymeulen, R. C. Anderson, S. Seshadri and M. G. Schaap, "Electrical Properties Cup (EPC) for characterizing water content of martian and lunar soils", *IEEE Aerospace Conference*, Big Sky, Montana, 2006, paper no. 1400, pp. 18.
- [71] D. H. Chung, W. B. Westphal and G. R. Olhofet, "Dielectric properties of Apollo 14 lunar samples", *Proceedings of the 3rd Lunar Science Conference*, The MIT Press, Cambridge, Vol. 3, 1972, pp. 3161-3172.
- [72] Remke L. van Dam, Brian Borchers and Jan M. H. Hendrickx, "Methods for prediction of soil dielectric properties: a review", *Proceedings of the SPIE*, Vol. 5794, 2005, pp. 188-197.
- [73] F. T. Ulaby, R. K. Moore and A. K. Fung, "Microwave dielectric properties of natural earth materials" in *Microwave Remote Sensing, III: From theory to applications*, Ed. F.

- T. Ulaby, R. K. Moore and A. K. Fung, Artech House, Norwood, USA, 1986, pp. 2017-2027.
- [74] M. Stacheder, "TDR and low-frequency measurements for continuous monitoring of moisture and density in a snow pack", *International Agrophysics*, Vol. 19, 2005, pp. 75-78.
- [75] Mark Nurge, "In-situ dielectric spectroscopy (ISDS) for water detection on the lunar surface". Online, 12th April 2011. Available: http://www.nasa.gov/pdf/499471main_ksc_nurge_insitu_dielectric_spectroscopy.pdf.
- [76] David S. McKay, James L. Carter, Walter W. Boles, Carlton C. Allen and Judith H. Allton, "JSC-1: A new lunar soil simulant", *Engineering, Construction and Operations in Space IV*, American Society of Civil Engineers, 1994, pp. 857-866. Online, 7th February 2011. Available: <http://ares.jsc.nasa.gov/HumanExplore/Exploration/EXlibrary/DOCS/EIC050.HTML>.
- [77] Online, 28th March 2011. Available: <http://www.orbitec.com/store/simulant.html>.
- [78] Rodger Magness and Patrick Plancke, "ESA TEC-E wireless technology dossier, Annex A, An Assessment of Wireless Proximity Networks for Space Applications", *Proceedings of 9th ESA Workshop on Advanced Space Technologies for Robotics and Automation*, ASTRA 2006, ESTEC, Noordwijk, The Netherlands, November 28-30, 2006. Online, 7th February 2011. Available: <http://robotics.estec.esa.int/ASTRA/Astra2006/Papers/ASTRA2006-1.3.2.01.pdf>.
- [79] Anirudh Daga, Gaylon R. Lovelace, Deva K. Borah and Phillip L. De Leon, "Terrain-Based Simulation of IEEE 802.11a and b Physical Layers on the Martian Surface", *IEEE Transactions on Aerospace and Electronic Systems*, Vol. 43, No. 4, 2007, pp. 1617-1624.
- [80] Vishwanath Chukkala, Phillip De Leon, Stephen Horan and Vijayakumar Velusamy, "Radio frequency channel modeling for proximity networks on the Martian surface", *Computer Networks*, Vol. 47, 2005, pp. 751-763.
- [81] D. K. Borah, Anirudh Daga, Gaylon R. Lovelace and Phillip De Leon, "Performance evaluation of the IEEE 802.11a and b WLAN physical layer on the Martian surface", *Proceedings of IEEE Aerospace Conference*, Big Sky, Montana, 2005, pp. 1429-1437.

- [82] Anirudh Daga, Deva K. Borah, Gaylon R. Lovelace and Phillip De Leon, "Physical layer effects on MAC layer performance of IEEE 802.11a and b WLAN on the Martian surface", *Proceedings of IEEE Aerospace Conference*, Big Sky, Montana, 2006, pp. 8.
- [83] Phillip De Leon, Stephen Horan, Deva Borah and Ray Lyman, "Effective utilization of commercial wireless networking technology in planetary environments: year 2 annual report", Annual Report NASA, Glenn Research Center, March 2005. Online, 7th February 2011. Available: http://ntrs.nasa.gov/archive/nasa/casi.ntrs.nasa.gov/20050092405_2005093383.pdf.
- [84] Driss Benhaddou, Manikanden Balakrishnan, Xiaojing Yuan, Ji Chen, Mukesh Rungta, Rick Barton and Heng Yang, "Wireless Sensor Networks for Space Applications: Network Architecture and Protocol Enhancements", *Sensors & Transducers Journal*, Vol. 7, Special Issue, October 2009, pp. 203-212.
- [85] T. Vladimirova, C. P. Bridges, G. Prassinou, Xiaofeng Wu, K. Sidibeh, D. J. Barnhart, A. H. Jallad, J. R. Paul, V. Lappas, A. Baker, K. Maynard and R. Magness, "Characterising wireless sensor motes for space applications", 2nd NASA/ESA Conference on Adaptive Hardware and Systems (AHS), Edinburgh, 2007, pp. 43-50. Online, 7th February 2011. Available: <http://epubs.surrey.ac.uk/2002/1/fulltext.pdf>.
- [86] Philippe Dubois, Cyril Botteron, Valentin Mitev, Carlo Menon, Pierre-Andre Farine, Paolo Dainesi, Adrian Ionescu and Herbert Shea, "Ad hoc wireless sensor networks for exploration of Solar-system bodies", *Acta Astronautica*, Vol. 64, Issue 5-6, 2009, pp. 626-643.
- [87] W. Ye, J. Heidemann and D. Estrin, "An energy-efficient MAC protocol for wireless sensor networks", *Proceedings of IEEE INFOCOM*, New York, Vol.3, 2002, pp. 1567-1576.
- [88] A. Sinha and A. Chandrakasan, "Dynamic power management in wireless sensor networks", *IEEE Design and Test of Computers*, Vol. 18, No. 2, 2001, pp. 62-74.
- [89] B. H. Calhoun, D. C. Daly, N. Verma, D. F. Finchelstein, D. D. Wentzloff, A. Wang, S. H. Cho and A. P. Chandrakasan, "Design considerations for ultra-low energy wireless microsensor nodes", *IEEE Transactions on Computers*, Vol. 54, Issue 6, 2005, pp. 727-740.

- [90] A. Rogoyski, B. Skidmore, V. Maheswaran, I. Wright, J. Zarnecki and C. Pillinger, "Wide area microprobe analyser (WAMPA)", *Acta Astronautica*, Vol. 59, Issue 8-11, 2006, pp. 1029-1038.
- [91] A. Schiele, J. Laycock, A. W. Ballard, M. Cosby and E. Picardi, "DALOMIS: a data transmission and localisation system for microprobes swarms", *Proceedings of The 8th International Symposium on Artificial Intelligence, Robotics and Automation in Space-ISAIRAS*, Munich, Germany, European Space Agency Special Publication 603, 2005, pp. 693-703.
- [92] N. Patwari, J. N. Ash, S. Kyperountas, A. O. Hero, R. L. Moses and N. S. Correal, "Locating the nodes: cooperative localization in wireless sensor networks", *IEEE Signal Processing Magazine*, Vol. 22, Issue 4, 2005, pp. 54-69.
- [93] D. Niculescu, "Positioning in ad hoc sensor networks", *IEEE Network*, Vol. 18, Issue 4, 2004, pp. 24-29.
- [94] G. Sun, J. Chen, W. Guo and K. J. R. Liu, "Signal processing techniques in network-aided positioning: a survey of state-of-the-art positioning designs", *IEEE Signal Processing Magazine*, Vol. 22, Issue 4, 2005, pp. 12-23.
- [95] R. J. Fontana, "Recent system applications of short-pulse ultra-wideband (UWB) technology", *IEEE Transactions on Microwave Theory and Techniques*, Vol. 52, Issue 9, 2004, pp. 2087-2104.
- [96] Online, 22nd February 2011. Available: <http://lcross.arc.nasa.gov/water.htm>.
- [97] Eduardo Landulfo, Eliane Goncalves Larroza, Ani S. Torres, Fabio J. da Silva Lopes, Renata da Costa and Wellington C. de Jesus, "Atmospheric water-vapor detection using laser remote sensing", Online, 22nd February 2011. Available: <http://spie.org/x31449.xml?ArticleID=x31449>.
- [98] Michael S. Brown, Gregory J. Fiechtner, J. V. Rudd, David A. Zimdars, Matthew Warmuth and James R. Gord, "Water-vapor detection using asynchronous THz sampling", *Applied Spectroscopy*, Vol. 60, Issue 3, 2006, pp. 261-265.
- [99] Joel A. Silver and D. Christian Hovde, "Near-infrared diode laser airborne hygrometer", *Review of Scientific Instruments*, Vol. 65, 1994, pp. 1691-1694.

- [100] Georges Durry and Gerard Megie, "In situ measurements of H₂O from a stratospheric balloon by diode laser direct-differential absorption spectroscopy at 1.39 μm", *Applied Optics*, Vol. 39, Issue 30, 2000, pp. 5601-5608.
- [101] G . J . Gaskin and J . D . Miller, "Measurement of soil water content using a simplified impedance measuring technique", *Journal of Agricultural Engineering Research*, Vol. 63, Issue 2, February 1996, pp. 153-159.
- [102] Online, 8th February 2011. Available:
http://en.wikipedia.org/wiki/Infrared_spectroscopy.
- [103] Online, 8th February 2011. Available:
http://www.ibsg-st-petersburg.com/About_Us/h20.htm.
- [104] Yankee Environmental Systems Inc., Online, 19th February 2011. Available:
<http://www.yesinc.com/products/data/cmh/index.html>.
- [105] H. C. Chaudhari and V. J. Shinde, "Dielectric study of moisture laden soils at X-band microwave frequency", *International Journal of Physical Sciences*, Vol. 3, No. 3, 2008, pp. 75-78.
- [106] J. Baker-Javis, E. J. Vanzura and W. A. Kissick, "Improved technique for determining complex permittivity with the transmission/reflection method", *IEEE Transactions on Microwave Theory and Techniques*, Vol. 38, Issue 8, 1990, pp. 1096-1103.
- [107] Michael D. Janezic and Jeffrey A. Jargon, "Complex permittivity determination from propagation constant measurement", *IEEE Microwave and Guided Wave Letters*, Vol. 9, No. 2, 1999, pp 76-78.
- [108] S. D. Logsdon, "Soil dielectric spectra from vector network analyzer data", *Soil Science Society of America Journal*, Vol. 69, No. 4, 2005, pp. 983-989.
- [109] S. K. Srivastava and G. P. Mishra, "Study of the characteristics of the soil of Chhattisgarh at X-band frequency", *Sadhana*, Vol. 29, Part 4, 2004, pp. 343-347.
- [110] Jayesh Pabari, Shrutisingh Yadav and Rajani Singh, "Microwave Detection of Soil Moisture using C-band Rectangular Waveguide", *Sensors & Transducers Journal*, International Frequency Sensor Association, Vol. 120, Issue 9, September 2010, pp. 134-141.

- [111] M. Leoncini, G. Resta and P. Santi, "Analysis of a wireless sensors dropping problem in environmental monitoring", *IEEE Proceedings of 4th International Symposium on Information Processing in Sensor Networks (IPSN)*, 2005, pp. 239-245.
- [112] M. Leoncini, G. Resta and P. Santi, "Partially controlled deployment strategies for wireless sensors", *Ad Hoc Networks*, Vol. 7, Issue 1, January 2009, pp. 1-23.
- [113] K. Chakrabarty, S. S. Iyengar, Qi Hairong and Cho Eungchun, "Grid coverage for surveillance and target location in distributed sensor networks", *IEEE Transactions on Computers*, Vol. 51, Issue 12, Dec 2002, pp. 1448-1453.
- [114] Y. Zou and K. Chakrabarty, "Uncertainty-aware and coverage-oriented deployment for sensor networks", *Journal of Parallel and Distributed Computing*, Vol. 64, Issue 7, July 2004, pp. 788-798.
- [115] A. Howard, M. J. Mataric and G. S. Sukhatme, "An incremental self-deployment algorithm for mobile sensor networks", *Autonomous Robots*, Vol. 13, Issue 2, 2002, pp. 113-126.
- [116] A. Howard, M. J. Mataric and G. S. Sukhatme, "Mobile sensor network deployment using potential fields: a distributed, scalable solution to the area coverage problem", *Proceedings of the 6th International Symposium on Distributed Autonomous Robotics Systems (DARS)*, Fukuoka, Japan, 2002, pp. 299-308.
- [117] S. Kumar, T. Lai and A. Arora, "Barrier coverage with wireless sensors", *Proceedings of the 11th Annual International Conference on Mobile Computing and Networking (Mobicom)*, 2005, pp. 284-298.
- [118] Y. Zou and K. Chakrabarty, "Sensor deployment and target localization based on virtual forces", *22nd Annual Joint Conference of the IEEE Computer and Communications (Infocom)*, 2003, Vol. 2, pp. 1293-1303.
- [119] J. Chen, E. Shen and Y. Sun, "The deployment algorithms in wireless sensor networks: a survey", *Information Technology Journal*, Vol. 8, Issue 3, 2009, pp. 293-301.
- [120] G. L. Wang, G. H. Cao and T. F. L. Porta, "Movement assisted sensor deployment", *IEEE Transactions on Mobile Computing*, Vol. 5, No. 6, 2006, pp. 640-652.
- [121] X. Q. Wang, Y. T. Yang and Z. L. Zhang, "A virtual rhomb grid-based movement-assisted sensor deployment algorithm in wireless sensor networks", *Proceedings of the*

1st International Multi-Symposiums on Computer and Computational Sciences, Hanzhou, Zhejiang, 2006, pp. 491-495.

- [122] P. Wan and C. Yi, "Coverage by Randomly Deployed Wireless Sensor Networks", *IEEE Transactions on Information Theory*, Vol. 52, Issue 6, 2006, pp. 2658-2669.
- [123] X. Bai, S. Kumar, D. Xuan, Z. Yun and T. H. Lai, "Deploying wireless sensors to achieve both coverage and connectivity", *Proceedings of the 7th ACM International Symposium on Mobile Ad Hoc Networking and Computing*, Florence, Italy, 2006, pp. 131-142.
- [124] P. N. Balister and S. Kumar, "Random vs. deterministic deployment of sensors in the presence of failures and placement errors", *IEEE INFOCOM*, Rio de Janeiro, Brazil, 2009, pp. 2896-2900.
- [125] M. Maleki, "QoM and lifetime-constrained random deployment of sensor networks for minimum energy consumption", *Proceedings of the 4th IEEE International Symposium on Information Processing in Sensor Networks (IPSN)*, 2005, pp. 293-300.
- [126] T. Clouqueur, V. Phipatanasuphorn, P. Ramanathan and K. K. Saluja, "Sensor deployment strategy for target detection", *Proceedings of the 1st ACM International Workshop on Wireless Sensor Networks and Applications (WSNA)*, 2002, pp. 42-48.
- [127] R. Edwards and J. Durkin, "Computer prediction of service areas for VHF mobile radio networks", *Proceedings of the IEE*, Vol. 116, Issue 9, September 1969, pp. 1493-1500.
- [128] J. Durkin, "Computer prediction of service areas for VHF and UHF land mobile radio services", *IEEE Transactions on Vehicular Technology*, Vol. 26, Issue 4, November 1977, pp. 323-327.
- [129] J. Walfisch and H. L. Bertoni, "A theoretical model of UHF propagation in urban environments", *IEEE Transactions on Antennas and Propagation*, Vol. 36, 1988, pp. 1788-1796.
- [130] J. M. Hernando and F. Perez-Fontan, *Introduction to Mobile Communications Engineering*, Boston, USA, Artech House, 1999.
- [131] J. D. Parsons, *The Mobile Radio Propagation Channel*, 2nd Edition, New York, Wiley, 2000.

- [132] George Kennedy, *Electronic Communication Systems*, 3rd Edition, McGraw-Hill Book Company, 1985.
- [133] J. D. Gibson, *The Mobile Communications Handbook*, Florida, USA, CRC Press Inc., 1996.
- [134] W. C. Y. Lee, *Mobile Communications Engineering*, McGraw Hill Publications, New York, 1985.
- [135] K. Bullington, "Radio Propagations at Frequencies above 30 Megacycles", *Proceedings of the IEEE*, Vol. 35, 1947, pp. 1122-1136.
- [136] J. Epstein and D. W. Peterson, "An Experimental Study of Wave Propagation at 840 M/C", *Proceedings of the IRE*, Vol. 41, No. 5, 1953, pp. 595-611.
- [137] J. Deygout, "Multiple Knife-edge Diffraction of Microwaves", *IEEE Transactions on Antennas and Propagation*, Vol. 14, No. 4, 1966, pp. 480-489.
- [138] J. P. Pabari, Y. B. Acharya, U. B. Desai, S. N. Merchant and B. Gopalkrishnan, "Radio Frequency Modelling for Future Wireless Sensor Network on Surface of the moon", *International Journal of Communications, Network and System Sciences*, Scientific Research Publication, Vol. 3, No. 4, April 2010, pp. 395-401.
- [139] Online, 3rd May 2011. Available: <http://www.mathworks.com/products/matlab/>.
- [140] Austriamicrosystems, Online, 15th February 2011. Available: <http://www.austriamicrosystems.com/eng/Press/Release-Archive-2010/2.4-GHz-multi-channel-FSK-transceiver>.
- [141] Grant H. Heiken, David T. Vaniman and Bevan M. French, *Lunar source book a user's guide to the moon*, Cambridge University Press, 1991.
- [142] Jayesh P. Pabari, Y. B. Acharya and U. B. Desai, "Investigation of Wireless Sensor Deployment Schemes for In-Situ Measurement of Water Ice near Lunar South Pole", *Sensors & Transducers Journal*, International Frequency Sensor Association, Vol. 111, Issue 12, December 2009, pp. 86-105.
- [143] T. S. Rappaport, S. Y. Seidal and R. Singh, "900 MHz multipath propagation measurements for US digital cellular radiotelephone", *IEEE Transactions on Vehicular Technology*, Vol. 39, No. 2, May 1990, pp. 132-139.
- [144] Online, 11th January 2011. Available: <http://www.wirelesscommunication.nl/reference/chaptr03/ricepdf/ricepdf.htm>.

- [145] Online, 11th January 2011. Available:
<http://www.wirelesscommunication.nl/reference/chaptr03/rayleigh.htm>.
- [146] Gregory D. Durgin, *Space-Time Wireless Channels*, Prentice Hall PTR, NJ, 2003.
- [147] Online, 11th January 2011. Available:
<http://mathworld.wolfram.com/ModifiedBesselFunctionoftheFirstKind.html>.
- [148] Hulya Gokalp and Sana Salous, "Multipath Statistics for 3G W-CDMA Systems", Online, 11th January 2011. Available:
<http://www.dur.ac.uk/comms.systems/pdfs/multipath%20statistics%20for%203G.PDF>
.
- [149] Matthias Patzold, Arkadiusz Szczepanski and Neji Youssef, "Methods for modeling of specified and measured multipath power delay profiles", *IEEE Transactions on Vehicular Technology*, Vol. 51, No. 5, September 2002, pp. 978-988.
- [150] Vinko Erceg, David G. Michelson, Saeed S. Ghassemzadeh, Larry J. Greenstein, A. J. Rustako, Peter B. Guerlain, Marc K. Dennison, R. S. Roman, Donald J. Barnickel, Spencer C. Wang and Robert R. Miller, "A model for the multipath delay profile of fixed wireless channels", *IEEE Journal on Selected Areas in Communications*, Vol. 17, No. 3, March 1999, pp. 399-410.
- [151] Online, 11th January 2011. Available:
http://en.wikipedia.org/wiki/Nyquist%E2%80%93Shannon_sampling_theorem.
- [152] Online, 11th January 2011. Available:
http://en.wikipedia.org/wiki/Coherence_bandwidth.
- [153] Rodger Magness, "TEC-E technology dossier: wireless onboard spacecraft and in space exploration, annex A, short-range RF wireless (proximity) networks technology assessment for space applications", Technical Note Draft 0.10, ESA, 3rd April 2006, Online, 12th January 2011. Available: <http://emits.esa.int/emits-doc/1-5200-RD1-ESA-Wireless-Dossier-AnnexA-Draft-R0.pdf>.
- [154] Tushar Tank and Jean-Paul M. G. Linnartz, "Statistical characterization of Rician multipath effects in a mobile-to-mobile communication channel", *International Journal of Wireless Information Networks*, Vol. 2, No. 1, January 1995, pp. 17-26.

- [155] William C. Lindsey, "Error probabilities for Rician fading multichannel reception of binary and N-nary signals", Technical Report No. 32-450, Jet Propulsion Laboratory, California Institute of Technology, California, 3rd June 1963.
- [156] Online, 9th May 2011. Available: http://en.wikipedia.org/wiki/Skin_depth.
- [157] Online, 5th October 2010. Available: <http://www.millipore.com/>.
- [158] Victor F. Petrenko, "Electrical properties of ice", Special Report 93-20, CRREL, 1993. Online, 25th April 2011. Available: <http://www.dtic.mil/cgi-bin/GetTRDoc?AD=ADA270432&Location=U2&doc=GetTRDoc.pdf>.
- [159] Online, 16th February 2011. Available: http://science.nasa.gov/science-news/science-at-nasa/2009/13nov_1crossresults/.
- [160] Jeffrey P. Walker, Garry R. Willgoose and Jetse D. Kalma, "In situ measurement of soil moisture: a comparison of techniques", *Journal of Hydrology*, Vol. 293, Issues 1-4, June 2004, pp. 85-99.
- [161] Analog Devices, "1 GSPS Direct Digital Synthesizer", 2009. Online, 24th January 2011. Available: www.analog.com/static/imported-files/Data_Sheets/AD9858.pdf.
- [162] J. G. Mantovani and C. I. Calle, "Dielectric Properties of the Martian Soil Simulant", *Proceedings of the 40th Space Congress*, 2003.
- [163] J. P. Pabari, Y. B. Acharya, U. B. Desai and S. N. Merchant, "Embedded Impedance Sensor Design for Future Lunar Wireless Sensor Network with 'Chirp' Type Perturbation Signal", *Proceedings of the 2009 International Conference on Signals Systems and Automation*, Vallabhvidyanagar, 28th-29th December 2009, pp. 144-147.
- [164] Robert J. Purdy, Peter E. Blankenship, Charles Edward Muehe, Charles M. Rader, Ernest Stern and Richard C. Williamson, "Radar signal processing", *Lincoln Laboratory Journal*, Vol. 12, No. 2, 2000, pp. 297-320.
- [165] Dan Yu, Farook Sattar and Braham Barkat, "Multiresolution fragile watermarking using complex chirp signals for content authentication", *Pattern Recognition*, Vol. 39, Issue 5, 2006, pp. 935-952.
- [166] Jayesh P. Pabari, "Efficient extension of conventional low frequency filter bank spectrometer by implementation of high resolution Chirp Z signal processing", *International Journal of Electronics*, Vol. 95, Issue 10, 2008, pp. 1073-1081.

- [167] Jayesh P. Pabari, A. B. Shah, N. M. Vadher, Vishal M. Shah, and Ashish Dubey, "Investigations on groove design for modulating frequency response of SAW RAC chirp filter", *International Journal of Electronics*, Vol. 95, Issue 11, 2008, pp. 1201-1208.
- [168] Analog Devices, "1 MSPS, 12-Bit Impedance Converter, Network Analyzer", 2009. Online, 24th January 2011. Available: http://www.analog.com/static/imported-files/data_sheets/AD5933.pdf.
- [169] Marcus E. Hobbs, Mu Shik Jhon and Henry Eyring, "The dielectric constant of liquid water and various forms of ice according to significant structure theory", *Proceedings of the National Academy of Sciences of the USA*, Vol. 56, No. 1, 1966, pp. 31-38.
- [170] N. Suresh, J.C. Callagan and A.E. Creelman, "Microwave measurement of the degree of binding of water absorbed in soils", *Journal of Microwave Power and Electromagnetic Energy*, Vol. 2, Issue 4, 1967, pp. 129-137.
- [171] J. C. Moore and N. Maeno, "Dielectric properties of frozen clay and silt soils", *Cold Regions Science and Technology*, Vol. 21, Issue 3, 1993, pp. 265-273.
- [172] Online, 12th November 2010. Available: <http://www.waynekerrtest.com/>.
- [173] Online, 12th November 2010. Available : <http://en.wikipedia.org/wiki/Capacitance>.
- [174] Ronald T. Atkins, Timothy Pangburn, Roy E. Bates and Bruce E. Brockett, "Soil moisture determinations using capacitance probe methodology", Special Report 98-2, Cold Regions Research and Engineering Laboratory, US Army Corps of Engineers, 1998.
- [175] Casey Q. LaMarche, Jennifer Sinclair Curtis and Philip T. Metzger, "Permeability of JSC-1A: A lunar soil simulant", *Icarus*, Vol. 212, Issue 1, 2011, pp. 383-389.
- [176] V. D. Krotikov, "Dielectric properties of dry soils", *IzvestijaVUZ'ov. Radiophysica*, Vol. 5, No. 6, 1962, p. 1057.
- [177] Online, 26th January 2011. Available: <http://www.thermonde.com/battery.htm>.
- [178] Online, 26th January 2011. Available: http://en.wikipedia.org/wiki/Multi-layer_insulation.

Publications

The publications based on the work presented in this thesis as well as the publications related to the central theme of the thesis are listed here.

Journal:

- J. P. Pabari, Y. B. Acharya and U. B. Desai, “Investigation of Wireless Sensor Deployment Schemes for In-Situ Measurement of Water Ice near Lunar South Pole”, *Sensors & Transducers Journal*, International Frequency Sensor Association, Vol. 111, Issue 12, December 2009, pp. 86-105.
- J. P. Pabari, Y. B. Acharya, U. B. Desai, S. N. Merchant and B. G. Krishna, “Radio Frequency Modelling for Future Wireless Sensor Network on Surface of the Moon”, *International Journal of Communications, Network and System Sciences*, Scientific Research Publication, Vol. 3, No. 4, April 2010, pp. 395-401.
- J. P. Pabari, Y. B. Acharya, U. B. Desai and S. N. Merchant, “Development of Impedance Based, Miniaturized Wireless Water Ice Sensor for Future Planetary Applications”, *IEEE Transactions on Instrumentation and Measurement*, Accepted.

Journal (Under Review):

- J. P. Pabari, Y. B. Acharya, U. B. Desai, S. N. Merchant and B. G. Krishna, “Lunar Multipath Environment and Analysis of Point-to-Point Wireless Link on Surface of the Moon”, *IEEE Transactions on Aerospace and Electronic Systems*.

Conference Proceedings:

- J. P. Pabari, Y. B. Acharya, U. B. Desai and S. N. Merchant, “Embedded Impedance Sensor Design for Future Lunar Wireless Sensor Network with ‘Chirp’ Type Perturbation Signal”, *Proceedings of the 2009 International Conference on Signals Systems and Automation*, Vallabhvidyanagar, 28th-29th December 2009, pp. 144-147.

Presented:

- Jayesh Pabari and Y. B. Acharya, “Evaluation of Contact Type Impedance Sensor for Future Lunar Wireless Sensor Network”, Poster Paper, *16th National Space Science Symposium 2010*, ISRO, 24th-27th February 2010, Dept. of Physics, Saurashtra University, Rajkot.

Acknowledgements

This thesis would have been difficult without the help of several individuals who, in one way or another, devoted their precious time for the completion.

I would like to express my sincere gratitude to my guide Prof. U. B. Desai for his continuous support and invaluable guidance in my research, motivation, positive outlook, patience, intelligence, enthusiasm, immense knowledge and pleasing personality. I could not have imagined having a better guide and 'guru' for my research.

I would also like to express my sincere gratitude to my co-guide Dr. Y. B. Acharya for his invaluable guidance, thought provoking arguments, advice, constant encouragement, untiring queries regarding the progress of the work, patience and positive outlook.

I am grateful to Prof. J. N. Goswami for his encouragement and advice during the meetings with him. I am indebted to Prof. S. V. S. Murty for his concern, advice, stimulating and encouraging discussions I had with him, positive approach, loving identity and the facility provided for research work.

I am thankful to Prof. S. N. Merchant for his invaluable guidance, encouragement, concern and advice during the discussions I had with him. I am also thankful to Mr. Kiran Kumar and Mr. B. Gopala Krishna for providing the digital elevation data of the lunar sites.

I would like to thank Mr. G. G. Dholakia for providing computing support and Mrs. Nishtha A. for providing library support. I am thankful to Mr. Hitesh Vaghela and Mr. H. N. Chandel for the assistance provided in workshop related work. I would like to thank Mr. S. B. Attara, Dr. Bhavik Kodrani, Mr. D. B. Pancholi, Mr. S. K. Goyal, Mrs. Deepthi Jagyasi, Mr. V. Ranganathan and Mrs. Parul Shah for the help provided at a short message. I am grateful to Mrs. S. Nair for her invariable help in SPANN lab at IITB.

I would like to express my sincere gratitude to my wife Krishna for her concern, constant motivation, invaluable suggestions during the discussions I had with her regarding the research and positive outlook.

Finally, I am grateful to my parents for their constant support, inspiration, advice and patience.

